

ARTICLES

**Gravitational waves from merging compact binaries:
How accurately can one extract the binary's parameters
from the inspiral waveform?**

Curt Cutler and Éanna E. Flanagan

Theoretical Astrophysics, California Institute of Technology, Pasadena, California 91125

(Received 7 September 1993)

The most promising source of gravitational waves for the planned kilometer-size laser-interferometer detectors LIGO and VIRGO are merging compact binaries, i.e., neutron-star-neutron-star (NS-NS), neutron-star-black-hole (NS-BH), and black-hole-black-hole (BH-BH) binaries. We investigate how accurately the distance to the source and the masses and spins of the two bodies will be measured from the inspiral gravitational wave signals by the three-detector LIGO-VIRGO network using “advanced detectors” (those present a few years after initial operation). The large number of cycles in the observable waveform increases our sensitivity to those parameters that affect the inspiral rate, and thereby the evolution of the waveform’s phase. These parameters are thus measured much more accurately than parameters which affect the waveform’s polarization or amplitude. To lowest order in a post-Newtonian expansion, the evolution of the waveform’s phase depends only on the combination $\mathcal{M} \equiv (M_1 M_2)^{3/5} (M_1 + M_2)^{-1/5}$ of the masses M_1 and M_2 of the two bodies, which is known as the “chirp mass.” To post-1-Newtonian order, the waveform’s phase also depends sensitively on the binary’s reduced mass $\mu \equiv M_1 M_2 / (M_1 + M_2)$, allowing, in principle, a measurement of both M_1 and M_2 with high accuracy. We show that the principal obstruction to measuring M_1 and M_2 is the post-1.5-Newtonian effect of the bodies’ spins on the waveform’s phase, which can mimic the effects that allow μ to be determined. The chirp mass is measurable with an accuracy $\Delta\mathcal{M}/\mathcal{M} \approx 0.1\%-1\%$. Although this is a remarkably small error bar, it is ~ 10 times larger than previous estimates of $\Delta\mathcal{M}/\mathcal{M}$ which neglected post-Newtonian effects. The reduced mass is measurable to $\sim 10\%-15\%$ for NS-NS and NS-BH binaries, and $\sim 50\%$ for BH-BH binaries (assuming $10M_\odot$ BH’s). Measurements of the masses and spins are strongly correlated; there is a combination of μ and the spin angular momenta that is measured to within $\sim 1\%$. Moreover, if both spins were somehow known to be small ($\lesssim 0.01M_1^2$ and $\lesssim 0.01M_2^2$, respectively), then μ could be determined to within $\sim 1\%$. Finally, building on earlier work of Marković, we derive an approximate, analytic expression for the accuracy ΔD of measurements of the distance D to the binary, for an arbitrary network of detectors. This expression is accurate to linear order in $1/\rho$, where ρ is the signal-to-noise ratio. We also show that, contrary to previous expectations, contributions to $\Delta D/D$ that are nonlinear in $1/\rho$ are significant, and we develop an approximation scheme for including the dominant of these nonlinear effects. Using a Monte Carlo simulation we estimate that distance measurement accuracies will be $\leq 15\%$ for $\sim 8\%$ of the detected signals, and $\leq 30\%$ for $\sim 60\%$ of the signals, for the LIGO-VIRGO three-detector network.

PACS number(s): 04.80.Nn, 04.30.Db, 97.60.Jd, 97.80.Af

I. INTRODUCTION

Neutron-star–neutron-star (NS-NS) binaries with orbital periods of less than half a day will spiral together and merge in less than a Hubble time, due to gravitational radiation reaction. Three such short-period NS-NS binaries have been observed in our Galaxy; when extrapolated to the rest of the Universe these observations result in an estimated NS-NS merger rate in the Universe of $\sim 10^2 \text{ yr}^{-1} \text{Gpc}^{-3}$ [1, 2]. A strong gravitational wave signal is emitted during the last few minutes of inspiral, before the tidal-disruption and/or coalescence stage begins. If the Laser Interferometer Gravitational Wave Observatory (LIGO) [3], and its French-Italian counterpart VIRGO [4], achieve the so-called “ad-

vanced detector” sensitivity level of Ref. [3], then they will be able to detect gravitational waves from the last few minutes of NS-NS inspirals out to distances of order $\sim 1 \text{ Gpc}$ [3]. Hence, event rates of order 10^2 yr^{-1} may be achieved. While there is no direct observational evidence relevant to the merger rates for neutron-star–black-hole (NS-BH) and black-hole–black-hole (BH-BH) binaries, arguments based on progenitor evolution scenarios suggest that these merger rates may also be on the order of $10^2 \text{ yr}^{-1} \text{Gpc}^{-3}$ [2, 5]. The merger of two $10M_\odot$ black holes would be detectable by the LIGO-VIRGO network out to cosmological distances at redshifts of $\sim 2 - 3$.

The gravitational waveforms arriving at the detectors depend on the inspiraling bodies’ masses and spins, the distance to the binary, its angular position on the sky,

and the orientation of the binary's orbital plane with respect to the line of sight. By comparing the observed waveforms with theoretically derived templates, the observers will extract these parameters to a level of accuracy that is determined by the noise in the detectors, and by the detectors' relative positions and orientations. From the output of a single detector, there will be sufficient information to determine the masses of the two bodies, but not their distance or their location on the sky. By combining the outputs of the three LIGO-VIRGO detectors, it should be possible to determine the location of the binary on the sky to within \sim one degree [6, 7], and the distance to the binary to within $\sim 30\%$.

There are many potential applications of such measurements, as has been emphasized by Schutz [6]. For example, coalescing binaries are potentially very useful standard candles for astronomical distance measurements — it has been estimated that from $\sim 10^2$ detected NS-NS events it will be possible to determine the Hubble constant H_0 to within $\sim 10\%$ [8–11]. It may also be possible to measure NS radii, and thus constrain the NS equation of state, by measuring the frequency at which the tidal disruption of the neutron star causes the waves to shut off [8]. And from gravitational wave observations of the final coalescence of two black holes, there may follow new insights into gravitational dynamics in the highly nonlinear regime. The effectiveness of these and other applications depends on the accuracy with which one can read off, from the measured waveform, parameters such as the distance to the binary and the masses of its two components.

The purpose of this paper is to estimate the limits on measurement accuracies that arise from sources of noise that are intrinsic to the detectors. These sources of noise include, for example, thermal vibrations in the interferometers' suspended test masses, and randomness in the arrival times of individual photons at the interferometers' mirrors (photon shot noise), which simulate in the interferometers' output the effects of gravitational waves [3]. Intrinsic detector noise is expected to be the dominant source of error in the determination of coalescing binary parameters, in part because gravitational waves interact very weakly with matter through which they pass [12]. Other possible sources of error which we do not consider here include (i) systematic errors due to insufficiently accurate theoretical modeling of the gravitational waveforms, which will be important primarily for mass and spin measurements [8, 13] and (ii) amplification or deamplification of the wave amplitudes by gravitational lensing effects, which will be important primarily for distance measurements. See Marković [9] for a detailed discussion of this issue.

Many of our conclusions have already been summarized in Cutler *et al.* [8]. Initial measurement accuracy analyses have been carried out by Finn and Chernoff [14], and by Jaranowski and Krolak [15], using a simplified, "Newtonian" model of the waveform. While Newtonian waveforms are adequate for predicting how accurately one can measure the distance to the source, they do not allow one to calculate how accurately the individual masses can be measured, as we shall explain below.

For this purpose, one must include post-Newtonian corrections to the waveform.

Much of our work was guided by the following sequence of considerations. These considerations introduce some of the issues addressed in this paper, motivate a number of approximations that we make in our analysis, and give a preview of some of our main conclusions.

First, coalescing binaries are very "clean" sources of gravitational waves: the waveform is determined to high accuracy by a relatively small number of parameters [6]. These parameters are the source's location, orientation, time of coalescence, and orbital phase at coalescence, as well as the bodies' masses and spin angular momenta. Various other complicating physical effects, not described by these parameters, can be shown to be unimportant. We can generally assume, for instance, that the orbits are circular. This is because radiation reaction causes the orbit's eccentricity ε to decrease during the inspiral, according to $\varepsilon^2 \propto P^{19/9}$, where P is the orbital period [16]. (The effect of a small eccentricity on the phase of the waveform scales like ε^2 .) The emitted gravitational waves are in the frequency band accessible to LIGO only for the last few minutes of inspiral, when $P < 0.2$ sec. Thus a binary born with ε of order unity and $P > 1$ h will have $\varepsilon^2 < 10^{-9}$ by the time it becomes "visible" to LIGO [17]. Also, tidal interactions between the bodies have been shown to be negligible [18, 19] (except for the last few orbits), so for our purposes the bodies can be treated as structureless, spinning point masses [20].

Second, this high predictability of the gravitational waveforms means that the technique of matched filtering can be used to detect the waves [12]. For the most distant (most frequently observed) sources, this will involve extracting the waveforms from the considerably larger instrumental noise in which they will be embedded. The matched filter technique works as follows. The measured strain amplitude in each detector

$$s(t) = h(t) + n(t) \quad (1.1)$$

consists of a (possibly present) signal $h(t)$, and the detector noise $n(t)$, which we assume is Gaussian. To detect any embedded signal, one first suppresses those frequency components of the signal at which the detector noise is largest by convolving with Wiener's optimal filter $w(t)$: thus, $s(t) \rightarrow \int w(t - \tau) s(\tau) d\tau$ [21]. Then, for each inspiral waveform $\hat{h}(t)$ in a large set of theoretical template waveforms, one computes the signal-to-noise ratio S/N , defined by

$$\frac{S}{N}[\hat{h}] = \frac{\int \hat{h}(t) w(t - \tau) s(\tau) d\tau dt}{\text{rms} \int \hat{h}(t) w(t - \tau) n(\tau) d\tau dt}. \quad (1.2)$$

In Eq. (1.2), the denominator is what *would* be the root-mean-square value of the numerator, if the detector output (1.1) consisted of noise alone. Thus, when no gravitational wave is present, each $S/N[\hat{h}]$ is a random variable with Gaussian distribution and root-mean-square equal to 1. Conversely, if $S/N[\hat{h}]$ is sufficiently large as to basically preclude the possibility of its arising from noise alone, for *any* of the $\sim 10^{15}$ template waveforms that

will be applied to the data each year, then one can assert with high confidence that a gravitational wave h has been detected, and that h is close to \hat{h} . It is easy to show that if some template waveform \hat{h} yields a signal-to-noise ratio of $S/N[\hat{h}] \geq 6.0$ in each of two detectors, then one can assert with $> 99\%$ confidence that a gravitational wave has been detected [8]. Defining the combined signal-to-noise ratio ρ of a network of detectors by

$$\rho \equiv \sqrt{\sum_a \rho_a^2}, \quad (1.3)$$

where ρ_a is the S/N in the a th detector, we see that $\rho \approx 8.5$ represents the “detection threshold” for two detectors. For a three-detector network, the detection threshold is still $\rho \approx 8.5$, corresponding to $S/N \gtrsim 4.9$ in each detector. Since detections at threshold represent the most distant coalescences that one can observe (given the binary’s masses, its orientation, and its angular position on the sky), and since coalescing binaries are presumably distributed roughly uniformly on large scales ($\gtrsim 100$ Mpc), the mean value of ρ for detected events will be roughly 1.5 times the threshold value [22]. Thus “typical” detections will have $\rho \approx 12.7$. Similarly, the strongest 1% of signals should have $\rho \gtrsim 40$; i.e., $(100)^{1/3}$ times the threshold value.

Third, much more information is obtainable from the waveform than one might naively expect, for the following reason. The LIGO and VIRGO detectors will be broad-band detectors, with good sensitivity in the frequency range 10 – 500 Hz. The gravitational wave trains from inspiraling stellar-mass binaries typically contain $\sim 10^3$ cycles in this range. Now, if the signal $h(t)$ and template $\hat{h}(t)$ lose phase with each other by just one cycle out of thousands, as they sweep upward in frequency from ~ 10 Hz to ~ 500 Hz, then the integral $\int \hat{h}(\tau)h(t)w(t-\tau)d\tau dt$ will be significantly diminished. Consequently the value of $S/N[\hat{h}]$ will be small unless the phase of the template waveform \hat{h} is “just right” throughout the inspiral. Since the evolution of the waveform’s phase is largely determined by the masses of the two bodies (through their influence on the inspiral rate), one might expect to measure the masses of the bodies with fractional error $\sim 1/\mathcal{N}_{\text{cyc}}$, where \mathcal{N}_{cyc} is the total number of cycles in the observed waveform. This fractional error of $\sim 10^{-3}$ contrasts with the $\sim 20\%$ accuracy with which one can determine parameters, such as the distance to the source, that do not affect the phase evolution (as was first pointed out by Cutler *et al.* [8] and by Chernoff and Finn [14]).

Fourth, our extension of the measurement-error analysis to include post-Newtonian effects introduces the following new features. To Newtonian order, the gravitational wave signal depends on the two masses *only* through the particular combination $\mathcal{M} \equiv \mu^{3/5}M^{2/5}$, where μ is the reduced mass and M is the total mass of the system. This combination is referred to as the “chirp mass.” The degeneracy in the dependence on the masses is broken, however, by post-Newtonian effects that in principle allow one to determine the individual

masses M_1 and M_2 . In the equation governing the evolution of the waveform’s phase [Eq. (3.9) below], the post-Newtonian terms are $\sim M/r$ times smaller than the Newtonian terms, where r is the orbital separation. Since $M/r \approx 1/20$ when the signal is strongest, one might expect to determine each of the two masses ~ 20 times less accurately than \mathcal{M} . We show in Sec. III that this expectation is correct, *provided* the spins of the bodies are known to be small.

Now, black holes and neutron stars in merging binaries may or may not be rapidly spinning. However if we cannot assume *a priori* that their spin angular momenta are very small, then in attempting to find the best fit to the data, we must allow for the possibility that the spin angular momenta are of order their maximum possible values. We show in Sec. III B that the extra “confusion” introduced by the spin dependence of the waveform worsens the accuracy of individual mass measurements by more than an order of magnitude. This is easy to understand: the leading order spin terms in the orbital evolution equation [Eq. (3.20) below] are only one-half post-Newtonian order higher than the leading terms responsible for splitting the mass degeneracy. Therefore the effect on the gravitational waveform of errors in M_1 and M_2 that keep \mathcal{M} fixed can be approximately masked by somewhat larger, compensating errors in its spins. Hence the measured values of masses and spins will have strongly correlated errors [cf. Fig. 3 below], thereby increasing mass-measurement errors [40]. Our results for measurement accuracies are summarized in Tables I and II and Fig. 4 below.

The rest of the paper is organized as follows. In Sec. II we review the anticipated detector noise levels, the basic elements of signal processing, and the lowest-order, “Newtonian” waveforms. In Sec. III we calculate expected mass-measurement accuracies, taking post-Newtonian effects into account. We do this in two stages: first neglecting spin effects in Sec. III A, then including them in Sec. III B. Our emphasis is on learning *roughly* what accuracies can be expected — in part because to treat the parameter-estimation problem in full generality would be extremely complicated. Therefore, we focus on a somewhat simplified “model” of the gravitational waveform, which nevertheless incorporates the effects that are most important for determining the mass-extraction accuracy. A further approximation which we make is to use a linear error-estimation formalism, which is valid when the errors are small (or equivalently, when the signal-to-noise ratio is large).

Most of the information that allows one to measure the binary masses is contained in the phase evolution of the waveform (rather than in its amplitude or polarization). Since all detectors in a detector network measure very nearly the same phase evolution, for the purpose of estimating mass measurement accuracies, to a good approximation it should be adequate to model measurements made by single detector. The mass measurement errors for N detectors are roughly those for a single detector, divided by \sqrt{N} .

When measuring the distance D to the binary, on the other hand, one must also determine the position of the

TABLE I. The rms errors for signal parameters and the correlation coefficient $c_{\mathcal{M}\mu}$, calculated assuming spins are negligible. The results are for a single “advanced” detector, the shape of whose noise curve is given by Eq. (2.1). M_1 and M_2 are in units of solar masses, while Δt_c is in units of msec. The rms errors are normalized to a signal-to-noise ratio of $S/N = 10$; the errors scale as $(S/N)^{-1}$, while $c_{\mathcal{M}\mu}$ is independent of S/N .

M_1	M_2	$\Delta\phi_c$	Δt_c	$\Delta\mathcal{M}/\mathcal{M}$	$\Delta\mu/\mu$	$c_{\mathcal{M}\mu}$
2.0	1.0	1.31	0.721	0.0038%	0.39%	0.899
1.4	1.4	1.28	0.713	0.0040%	0.41%	0.906
10	1.4	1.63	1.01	0.020%	0.54%	0.927
15	5.0	2.02	1.44	0.113%	1.5%	0.954
10	10	1.98	1.43	0.16%	1.9%	0.958

source on the sky and the amplitude and polarization of the waveform. Hence, to estimate distance measurement accuracies, we must model measurements by an entire detector network. However in this case it is a needless complication to use post-Newtonian waveforms; as we show in Sec. IV and Appendix C below, to a good approximation it is adequate to use Newtonian waveforms in the analysis. This is our approach in Sec. IV, where we estimate the distance measurement accuracy ΔD attainable by an arbitrary network of detectors. Jaranowski and Krolak have numerically calculated in several specific cases the distance measurement accuracy one can achieve with the LIGO-VIRGO network [15]. We provide a greatly simplified, analytic solution to the distance-accuracy estimation problem, using an approximation due to Marković [9]. The approximation consists in neglecting the effect on distance measurement errors of the relatively small uncertainty in the angular position of the source on the sky. Making this approximation, we derive a relatively simple formula for the rms distance error ΔD , which applies to any number of detectors with arbitrary orientations.

This formula is derived using the linear error-estimation formalism mentioned above, and consequently is accurate only to linear order in $1/D$. We show that, contrary to previous expectations, effects which are nonlinear in $1/D$ have a significant effect (i.e., factors $\gtrsim 2$) on the predicted distance-measurement accuracies, and develop an approximate method of calculation which gives rough estimates of these nonlinear effects. This method is based on a Bayesian derivation of the (non-Gaussian) probability distribution for the distance D , which incorporates our *a priori* knowledge as well as the information obtained from a gravitational wave measurement. The method also allows us to estimate values of ΔD for binaries that are seen nearly face-on, for which, as pointed out by Marković [9], the linear error-estimation method breaks down. Our results for nearly face-on binaries are typically factors of order 2 to 3 smaller than the upper-limit estimates given by Marković [9].

In Appendix A we extend the treatment of signal processing given in Sec. II to incorporate (i) an arbitrary number of detectors, (ii) the effects of *a priori* knowl-

edge, and (iii) estimation of measurement errors beyond the linear, Gaussian approximation. These extensions are required in Secs. III B and IV. We also develop other tools which should be useful in future analyses of LIGO-VIRGO measurement accuracies: we derive an expression for the minimum signal-to-noise ratio $(S/N)_{\min}$ necessary in order that the Gaussian approximation for estimation of measurement accuracy be valid, and explain how to treat degenerate points in parameter space at which the Gaussian approximation breaks down.

In this paper we will focus on three fiducial types of binary — NS-NS, BH-NS, and BH-BH — with fiducial masses $M_{\text{BH}} = 10M_\odot$ and $M_{\text{NS}} = 1.4M_\odot$ (unless otherwise specified). Throughout we use units where $G = c = 1$. Thus all quantities are measured in units of seconds, except where, for convenience, we use units of solar masses. The conversion factor is $1M_\odot = 4.926 \times 10^{-6} \text{ sec}$.

II. DETECTION AND MEASUREMENT OF GRAVITATIONAL WAVEFORMS

A. Detector characteristics

In order to decide what information can be extracted from gravitational waveforms, one must have a realistic model of the detector noise $n(t)$. This noise will have both Gaussian and non-Gaussian components. We will restrict our analysis to statistical errors due to Gaussian noise. It is likely that the effects of the non-Gaussian components will be unimportant due to (i) the rejection of events that are not simultaneously detected in two or more detectors and (ii) the filtering of the detector outputs with theoretical waveform templates; however this issue needs further study.

The remaining Gaussian noise can be described by its spectral density $S_n(f)$, where f is frequency. The LIGO team has published an estimate of the noise spectrum that might be attained a few years after LIGO comes on line — the so-called “advanced detector” noise spectral density [3]. We use the following rough analytic fit to their noise curve:

$$S_n(f) = \begin{cases} \infty, & f < 10 \text{ Hz}, \\ S_0 \{(f_0/f)^4 + 2[1 + (f^2/f_0^2)]\}, & f > 10 \text{ Hz}, \end{cases} \quad (2.1)$$

where $S_0 = 3 \times 10^{-48} \text{ Hz}^{-1}$ and $f_0 = 70 \text{ Hz}$. For frequencies $f < 10 \text{ Hz}$, the noise due to seismic vibrations is so large that we take it to be effectively infinite. Thermal noise dominates in the frequency band $10 \text{ Hz} \lesssim f \lesssim 50 \text{ Hz}$, and photon shot noise dominates for $f \gtrsim 50 \text{ Hz}$. We refer the reader to Refs. [3, 12] for more details on the sources of noise.

The amount of detector noise determines the strength of the weakest signals that can be detected, and thus the distance to which a given type of source can be seen. The noise level (2.1) will permit the detection of NS-NS mergers out to $\sim 1 \text{ Gpc}$ [3, 14, 22], giving an estimated detection rate of $\sim 10^2 \text{ yr}^{-1}$ [2]. In this paper we are principally concerned *not* with detection issues, but rather

with the accuracy of parameter estimation. This accuracy of parameter estimation depends only on the shape of the noise spectrum, and on the signal-to-noise (S/N) of the detection; e.g., simultaneously doubling both the noise levels and the signal strength leaves measurement accuracy unchanged. We normalize our results to a fixed S/N , and hence our results are independent of the parameter S_0 appearing in the noise spectrum (2.1).

Since the LIGO team's publication [3] of their estimate of the advanced detector's noise curve, there have been new developments in the understanding of the detector's thermal noise which indicate that the advanced thermal noise spectrum may be flatter than previously thought [23]. A modified noise-curve estimate, reflecting this new understanding, has not yet been published. Like the noise spectrum in Ref. [3] on which our simplified model (2.1) is based, the modified noise curve will depend on the values of advanced detector parameters (such as the quality factors of modes of vibration of the suspension wires and suspended masses) for which only rough estimates are available. Our approximate analytic formula describing the modified advanced detector noise curve, for one choice of detector parameters,

$$S_n(f) = \begin{cases} \infty, & f < 10 \text{ Hz}, \\ S_m \alpha^{-4} (f/f_m)^{-5}, & 10 \text{ Hz} \leq f \leq f_m/\alpha, \\ S_m (f/f_m)^{-1}, & f_m/\alpha \leq f \leq \alpha f_m, \\ S_m \alpha^{-3} (f/f_m)^2, & f \geq \alpha f_m, \end{cases} \quad (2.2)$$

where $S_m = 2.7 \times 10^{-47} \text{ Hz}^{-1}$, $f_m = 74 \text{ Hz}$, and $\alpha = 3.8$ [24], assumes particular detector parameters that accentuate the difference between Eqs. (2.2) and (2.1). Since the ultimate shape of the noise curve is not yet well known, we feel that it is useful to calculate the attainable measurement accuracies for both of these shapes of the noise spectrum. We shall see below (cf. Tables II and III) that the flatter spectrum of the modified noise curve (2.2) leads to a modest improvement in how accurately the binary's masses can be measured (for fixed signal-to-noise).

B. Review of parameter estimation

In this section we give a concise summary of those elements of signal processing that are necessary for parameter estimation. The basic concepts of detection and measurement have also been reviewed recently by Finn [26] and by Krolak *et al.* [27], in the specific context of laser interferometer gravitational wave measurements. In Appendix A we give a more detailed treatment of parameter estimation, together with an extensive discussion of the ways in which the simplified linear formalism described in this section can break down: (i) when the signal-to-noise of the detection is low and (ii) when our *a priori* knowledge of some of the binary parameters is not negligible compared to the information obtained from the measurement.

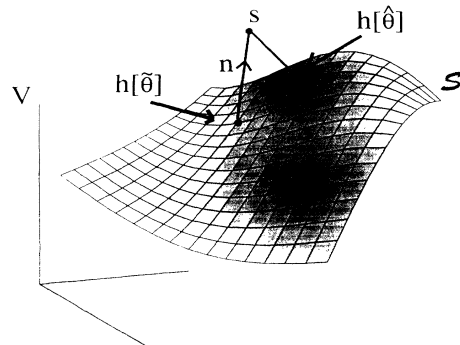


FIG. 1. Gravitational waveforms from coalescing compact binaries are completely specified by a finite number of parameters $\theta = (\theta^1, \dots, \theta^k)$, and so form a surface S in the vector space V of all possible measured detector outputs $s = s(t)$. The statistical properties of the detector noise endow V with the structure of an infinite-dimensional Euclidean space. This figure illustrates the relationships between the true gravitational wave signal $h(\tilde{\theta})$, the measured signal s , and the “best-fit” signal $h(\hat{\theta})$. Given a measured detector output $s = h(\tilde{\theta}) + n$, where $n = n(t)$ is the detector noise, the most likely values $\hat{\theta}$ of the binaries parameters are just those that correspond to the point $h(\hat{\theta})$ on the surface S which is closest [in the Euclidean distance $(s - h | s - h)$] to y .

We assume that an inspiraling binary gravitational wave *has* been observed, i.e., that the appropriate detection criterion has been met by the detector outputs. We now discuss how one determines what parameters for the inspiraling binary provide the best fit to the measured signal. The basic framework is illustrated in Fig. 1. The set of all gravitational waveforms from two inspiraling bodies can be characterized by a relatively small number of parameters (the distance to the source; the time of merger; five angles specifying the position of the source on the sky, the plane of the orbit, and the orbital phase at some given time; and the masses and spin angular momenta of the two bodies—15 parameters in all, assuming that the eccentricity of the orbit is negligible). We regard this set of waveforms as a 15-dimensional surface embedded in the vector space of all possible measured signals. In the absence of any noise, all measured signals from inspiraling binaries would lie on this submanifold; in practice, of course, the measured signal consisting of waveform plus noise is displaced off the submanifold.

The statistical properties of the noise determine a natural inner product on the vector space of signals. Given two signals $h_1(t)$ and $h_2(t)$, we define $(h_1 | h_2)$ by [28]

$$(h_1 | h_2) = 2 \int_0^\infty \frac{\tilde{h}_1^*(f) \tilde{h}_2(f) + \tilde{h}_1(f) \tilde{h}_2^*(f)}{S_n(f)} df, \quad (2.3)$$

where \tilde{h}_1 and \tilde{h}_2 are the Fourier transforms of h_1 and h_2 . This definition is chosen so that the probability for the noise to have some realization $n_0(t)$ is

$$p(n = n_0) \propto e^{-(n_0 | n_0)/2}. \quad (2.4)$$

Hence if the actual incident waveform is $h(t)$, then from Eq. (1.1) the probability of measuring a signal s in the

detector output is proportional to $e^{-(s-h|s-h)/2}$. Correspondingly, given a measured signal s , the gravitational waveform h that “best fits” the data is the one that minimizes the quantity $(s - h|s - h)$; see Fig. 1.

It also follows from Eq. (2.3) that for any functions $g(t)$ and $k(t)$, the expectation value of $(g|n)(k|n)$, for an ensemble of realizations of the detector noise $n(t)$, is just $(g|k)$. Hence the signal-to-noise (1.2) of the detection will be approximately given by

$$\frac{S}{N}[h] = \frac{(h|h)}{\text{rms } (h|n)} = (h|h)^{1/2}. \quad (2.5)$$

The kernel $w(t)$ of Wiener’s optimal filter appearing in Eq. (1.2) is just the Fourier transform of $1/S_n(f)$.

For a given incident gravitational wave, different realizations of the noise will give rise to somewhat different best-fit parameters. However, for large S/N , the best-fit parameters will have a Gaussian distribution centered on the correct values. Specifically, let $\tilde{\theta}^i$ be the “correct” values of the parameters on which the waveforms depend, and let $\tilde{\theta}^i + \Delta\theta^i$ be the best-fit parameters in the presence of some realization of the noise. Then for large S/N , the parameter-estimation errors $\Delta\theta^i$ have the Gaussian probability distribution [26]

$$p(\Delta\theta^i) = \mathcal{N} e^{-\frac{1}{2}\Gamma_{ij}\Delta\theta^i\Delta\theta^j}. \quad (2.6)$$

Here Γ_{ij} is the so-called Fisher information matrix defined by

$$\Gamma_{ij} \equiv \left(\frac{\partial h}{\partial \theta^i} \middle| \frac{\partial h}{\partial \theta^j} \right), \quad (2.7)$$

and $\mathcal{N} = \sqrt{\det(\Gamma/2\pi)}$ is the appropriate normalization factor. It follows that the root-mean-square error in θ^i is

$$\sqrt{\langle (\Delta\theta^i)^2 \rangle} = \sqrt{\Sigma^{ii}}, \quad (2.8)$$

where $\Sigma \equiv \Gamma^{-1}$.

The above discussion applies to measurements made by a single detector. The (straightforward) generalization to a network of detectors, which will be required in Sec. IV, is given in Appendix A.

The above discussion also neglects the effects of any *a priori* constraints on the parameters that may be available. The incorporation of such *a priori* information can have a significant effect on the predicted parameter-extraction accuracies (and also on the best-fit parameter values themselves). This is true not only for those parameters to which the constraints apply, but also for the remaining parameters because of correlations. The effect is significant whenever, for some parameter, the *a priori* information is comparable with the information derived from the measured signal. Hence, *a priori* constraints are usually important whenever we include in an error-estimation analysis parameters which are *weakly determined* by the data. In Appendix A we derive a generalization of Eq. (2.7) [cf. Eq. (A43) below] which roughly incorporates the effect of *a priori* information. This generalization will be used in Sec. III B, where we consider the dependence of the inspiral waveform h on the spins of the two bodies.

C. The gravitational wave signal in the Newtonian approximation

Inspiraling compact binaries can be described, to lowest order, as two Newtonian point particles whose orbital parameters evolve secularly due to gravitational radiation, where the gravitational waves and corresponding energy loss rate are given by the Newtonian quadrupole formula. That is, the orbital frequency Ω at any instant is given by

$$\Omega = \frac{M^{1/2}}{r^{3/2}}, \quad (2.9)$$

where $M \equiv M_1 + M_2$ is the total mass of the system and r is the orbital separation. The inspiral rate, for circular orbits, is given by

$$\frac{dr}{dt} = -\frac{r}{E} \frac{dE}{dt} = -\frac{64}{5} \frac{\mu M^2}{r^3}, \quad (2.10)$$

where $\mu \equiv M_1 M_2 / M$ is the reduced mass. Integrating Eq. (2.10) we obtain

$$r = \left(\frac{256}{5} \mu M^2 \right)^{1/4} (t_c - t)^{1/4}, \quad (2.11)$$

where t_c is the “collision time” at which (formally) $r \rightarrow 0$. Since the emitted gravitational waves are quadrupolar, their frequency f (cycles/sec) is equal to Ω/π . The gravitational waves induce a measured strain $h(t)$ at the detector which is given by (see, e.g., Ref. [12])

$$h(t) = \frac{(384/5)^{1/2} \pi^{2/3} Q(\theta, \varphi, \psi, \iota) \mu M}{D r(t)} \cos \left(\int 2\pi f dt \right), \quad (2.12)$$

where D is the distance to the source. The function Q and the angles $\theta, \varphi, \psi, \iota$ (which describe the position and orientation of the binary) are defined in Sec. IV below; they will not be needed in this section. In Eq. (2.12) we could have included the factor $(384/5)^{1/2} \pi^{2/3}$ in the definition of Q , but choose not to for later convenience.

Because both the amplitude and frequency of the signal increase as $t \rightarrow t_c$, the signal is referred to as a “chirp.” From Eqs. (2.9) and (2.10), the frequency evolves according to

$$\frac{df}{dt} = \frac{96}{5} \pi^{8/3} \mathcal{M}^{5/3} f^{11/3}, \quad (2.13)$$

where $\mathcal{M} \equiv \mu^{3/5} M^{2/5}$ is the chirp mass parameter discussed in Sec. I. The phase of the waveform $\phi(t) = \int^t 2\pi f(t') dt'$ is

$$\phi(t) = -2 \left[\frac{1}{5} \mathcal{M}^{-1} (t_c - t) \right]^{5/8} + \phi_c, \quad (2.14)$$

where the constant of integration ϕ_c is defined by $\phi \rightarrow \phi_c$ as $t \rightarrow t_c$.

In Eqs. (2.12)–(2.14) we have omitted the (obvious) time delay between signal emission and detection, and we have implicitly assumed that the detector and the binary’s center of mass are at rest with respect to each other. The latter requires some explanation. If the detector and binary are in relative motion, the detected signal is Doppler shifted with respect to the emitted signal. One cannot determine this Doppler shift from the

detected signal, since $h(t)$, as defined by Eqs. (2.12) and (2.13), is invariant under the transformation

$$(f, \mathcal{M}, \mu, r, D, t) \rightarrow (f/\lambda, \mathcal{M}\lambda, \mu\lambda, r\lambda, D\lambda, t\lambda). \quad (2.15)$$

Thus, strictly speaking, one can extract from the signal only the “Doppler-shifted” mass and distance parameters $\lambda\mathcal{M}$, $\lambda\mu$, and λD , where λ is the Doppler-shift factor. This is not just a feature of our simplified, Newtonian waveform; it also holds for the true, general-relativistic waveforms, as can be seen on purely dimensional grounds and from the fact that general relativity does not define any preferred mass or length scales.

Similarly, for binary sources at cosmological distances, the waves will depend on and reveal the redshifted masses

$$\mathcal{M} = (1+z)\mathcal{M}_{\text{true}}, \quad \mu = (1+z)\mu_{\text{true}}, \quad (2.16)$$

where z is the source’s cosmological redshift, and also depend on and reveal its so-called luminosity distance D_L [6, 9, 26]. Our measurement-accuracy analysis applies to these *redshifted* masses and to the luminosity distance. The determination of the true masses for very distant binaries will require some method of estimating redshifts; see, e.g., Ref. [9].

It is most convenient to work directly with the Fourier transform of $h(t)$,

$$\tilde{h}(f) \equiv \int_{-\infty}^{\infty} e^{2\pi ift} h(t) dt, \quad (2.17)$$

which is easily computed using the stationary phase approximation [12]. Given a function $B(t) = A(t) \cos \phi(t)$, where $d \ln A/dt \ll d\phi(t)/dt$ and $d^2\phi/dt^2 \ll (d\phi/dt)^2$, the stationary phase approximation provides the following estimate of the Fourier transform $\tilde{B}(f)$ for $f \geq 0$:

$$\tilde{B}(f) \approx \frac{1}{2} A(t) \left(\frac{df}{dt} \right)^{-1/2} \exp[i(2\pi ft - \phi(f) - \pi/4)]. \quad (2.18)$$

In this equation, t is defined as the time at which $d\phi(t)/dt = 2\pi f$, and (in a slight abuse of notation) $\phi(f)$ is defined as $\phi[t(f)]$. Using Eqs. (2.13) and (2.14) we obtain

$$\begin{aligned} t(f) &= t_c - 5(8\pi f)^{-8/3} \mathcal{M}^{-5/3}, \\ \phi(f) &= \phi_c - 2[8\pi \mathcal{M} f]^{-5/3}. \end{aligned} \quad (2.19)$$

Hence from Eq. (2.18), the Fourier transform of the Newtonian waveform is

$$\tilde{h}(f) = \frac{Q}{D} \mathcal{M}^{5/6} f^{-7/6} \exp[i\Psi(f)] \quad (2.20)$$

for $f \geq 0$, where the phase $\Psi(f)$ is

$$\Psi(f) = 2\pi f t_c - \phi_c - \frac{\pi}{4} + \frac{3}{4}(8\pi \mathcal{M} f)^{-5/3}. \quad (2.21)$$

Equation (2.20) for $\tilde{h}(f)$ is clearly invalid at very high frequencies, because the real inspiral will terminate at some finite orbital frequency. For BH-BH and BH-NS

mergers, there will be a transition from inspiral to a final plunge [29] near the location of the last stable circular orbit, which is roughly at $r = 6M$ for nonspinning bodies [30]. The final plunge will last roughly one orbital period. (Neutron stars merging with rapidly spinning black holes may instead tidally disrupt, thereby shutting off the waves, outside the horizon [18].) For NS-NS mergers, the two bodies will collide and coalesce at roughly $r = 6M$. Generally therefore the inspiral gravitational wave $h(t)$ will “shut off” at roughly $r = 6M$, and correspondingly $\tilde{h}(f)$ will shut off at roughly $f = (6^{3/2}\pi M)^{-1}$. We therefore “correct” the waveform (2.20) by setting $\tilde{h}(f) = 0$ for $f > (6^{3/2}\pi M)^{-1}$. We note that, when $r > 6M$,

$$\frac{|r^{-1}dr/dt|}{d\phi/dt} = \frac{2}{3} \frac{d^2\phi/dt^2}{(d\phi/dt)^2} < \frac{1}{55} \left(\frac{4\mu}{M} \right), \quad (2.22)$$

so the stationary phase approximation should reproduce the Fourier transform of $h(t)$ with good accuracy throughout the inspiral. Note that, as advertised in Sec. I, in the Newtonian approximation the signal (2.20) depends on M_1 and M_2 only through the chirp mass \mathcal{M} .

Using Eqs. (2.1) and (2.20), we can see how the signal-to-noise squared accumulates as the frequency sweeps upward:

$$\begin{aligned} (S/N)^2(f) &\equiv 4 \int_0^f \frac{|\tilde{h}(f')|^2}{S_n(f')} df' \\ &= 4 \frac{Q^2}{D^2} \mathcal{M}^{5/3} \int_0^f \frac{(f')^{-7/3}}{S_n(f')} df'. \end{aligned} \quad (2.23)$$

In Fig. 2 we plot the integrand $d(S/N)^2/df = 4|\tilde{h}(f)|^2/S_n(f)$, using the advanced detector noise spectrum (2.1). The shape of this curve is universal once the noise spectrum is given: the masses, the relative angles, the distance to the source, etc., affect only the overall amplitude. (This is strictly true only for the “Newtonian” signal, but will remain true to a good approximation when post-Newtonian effects are taken into account.) While 90% of the cycles come between 10 and 40 Hz, and while most of the energy is released in the last few orbits

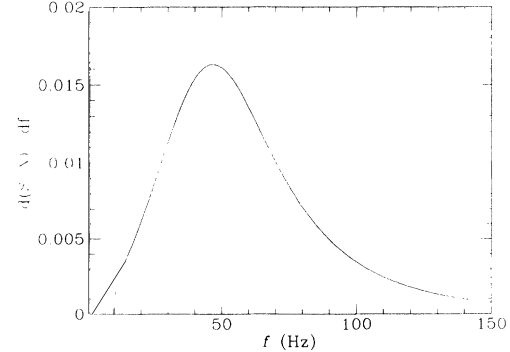


FIG. 2. This plot shows how the total signal-to-noise squared S^2/N^2 for a detected coalescing-binary waveform is distributed in frequency f , assuming the detector noise curve (2.1). Most of the signal-to-noise ratio comes not near 70 Hz where the detector sensitivity $S_n(f)^{-1}$ is highest, but rather at a somewhat lower frequency of ~ 50 Hz, because more cycles per unit frequency are received at lower frequencies.

at $f > 200$ Hz, we find that $\sim 60\%$ of the total signal-to-noise squared accumulates between 40 and 100 Hz, the frequency band in which LIGO is most sensitive.

We now evaluate the Fisher information matrix (2.7). For measurements using a single detector, there are only four parameters on which the Newtonian signal depends: an overall amplitude $\mathcal{A} \equiv (Q/D)\mathcal{M}^{5/6}$, and \mathcal{M} , t_c , and ϕ_c . The derivatives of $\tilde{h}(f)$ with respect to these parameters (for $f > 0$) are given by

$$\frac{\partial \tilde{h}}{\partial \ln \mathcal{A}} = \tilde{h}, \quad \frac{\partial \tilde{h}}{\partial t_c} = 2\pi i f \tilde{h}, \quad (2.24a)$$

$$\frac{\partial \tilde{h}}{\partial \phi_c} = -i \tilde{h}, \quad \frac{\partial \tilde{h}}{\partial \ln \mathcal{M}} = -\frac{5i}{4} (8\pi \mathcal{M} f)^{-5/3} \tilde{h}. \quad (2.24b)$$

From Eqs. (2.24) and the noise spectrum (2.1), it is straightforward to evaluate the Fisher information matrix (2.7) and its inverse Σ^{ij} [31]. General expressions for the elements of Γ_{ij} using Newtonian waveforms, valid for any detector noise spectrum, are given in Ref. [14]. We will not reproduce them here. However, for purposes of comparison to our post-Newtonian results in Sec. III, we list the rms errors $\Delta \mathcal{A}$, $\Delta \mathcal{M}$, Δt_c , and $\Delta \phi_c$ for the case of low-mass (e.g., NS-NS) binaries, assuming the approximate waveform (2.20) and the detector noise spectrum (2.1):

$$\Delta(\ln \mathcal{A}) = 0.10 \left(\frac{10}{S/N} \right), \quad (2.25a)$$

$$\Delta t_c = 0.40 \left(\frac{10}{S/N} \right) \text{ msec}, \quad (2.25b)$$

$$\Delta \phi_c = 0.25 \left(\frac{10}{S/N} \right) \text{ rad}, \quad (2.25c)$$

$$\Delta(\ln \mathcal{M}) = 1.2 \times 10^{-5} \left(\frac{10}{S/N} \right) \left(\frac{\mathcal{M}}{M_\odot} \right)^{5/3}. \quad (2.25d)$$

For low-mass binaries, the fact that we “cut off” the waveform $\tilde{h}(f)$ for $f > (6^{3/2}\pi M)^{-1}$ has little effect on the rms errors (2.25), due to the sharp rise in $S_n(f)$ at high frequency. The exact scaling of $\Delta(\ln \mathcal{M})$ as $\mathcal{M}^{5/3}$, and the fact that Δt_c and $\Delta \phi_c$ are independent of M , strictly hold only when the cutoff is unimportant. For BH-BH binaries with $S/N = 10$, one has $\Delta t_c = 0.60$ msec, $\Delta \phi_c = 0.32$ rad, and $\Delta(\ln \mathcal{M}) = 1.3 \times 10^{-5} (\mathcal{M}/M_\odot)^{5/3}$.

The rather phenomenal accuracy attainable for the chirp mass \mathcal{M} is due to the large number \mathcal{N}_{cyc} of cycles in the detectable portion of the gravitational waveform. We see from Eq. (2.13) that \mathcal{N}_{cyc} scales like $\mathcal{M}^{-5/3}$, so $\Delta(\ln \mathcal{M})$ is proportional $1/\mathcal{N}_{\text{cyc}}$, as one would expect.

The rms errors (2.25) apply to single-detector measurements. In practice, one will have a network of detectors, with different locations and orientations. For a network, $\Delta(\ln \mathcal{M})$, will be roughly given by Eq. (2.25d), but with S/N replaced by the combined signal-to-noise ρ of the detector network, defined by Eq. (1.3) above. This is because independent estimates of \mathcal{M} are obtained from each detector. The same argument does *not* apply to the rms errors in t_c , \mathcal{A} , and ϕ_c , because the gravitational waves will arrive at the different detectors at different

times, and because detectors with different orientations measure different values of \mathcal{A} and ϕ_c (cf. Sec. IV below).

We conclude this section by noting that from the measured value of the chirp mass \mathcal{M} alone, one already obtains a lower limit on the larger of the individual masses, and upper limits on the smaller mass and on the reduced mass. We adopt the convention that $M_1 \geq M_2$; i.e., M_1 always refers to the *larger* of the two masses. Then it follows by definition that

$$M_1 \geq 2^{1/5} \mathcal{M}, \quad M_2 \leq 2^{1/5} \mathcal{M}, \quad \mu \leq 2^{-4/5} \mathcal{M}. \quad (2.26)$$

However, if μ is unknown, then the mass ratio M_1/M_2 is unconstrained. The bounds (2.26) that follow from measuring \mathcal{M} may themselves be of astrophysical interest. For instance, if one determines using (2.26) that $M_1 \geq 3M_\odot$, then one may conclude that the heavier body is a black hole [assuming the redshift is small, cf. Eq. (2.16) above and associated discussion]. Also, it has been suggested [8] that from LIGO-VIRGO measurements of NS-BH coalescences where the BH is rapidly spinning, it may be possible to constrain the neutron star equation of state by measuring the frequency at which the NS’s tidal disruption causes the waves to shut off. Knowledge of this tidal-disruption frequency, coupled with an upper limit on the neutron star mass M_2 determined from the inspiral waveform, would allow one to place an upper limit on the stiffness of the equation of state.

III. POST-NEWTONIAN EFFECTS AND PARAMETER ESTIMATION

We now extend the analysis of the previous section to include post-Newtonian effects. We continue to treat the bodies as point masses, since tidal interactions have a negligible effect. Also, for the moment we will neglect the effects of the bodies’ spin angular momenta.

The post-Newtonian approximation provides the most accurate description currently available of the gravitational radiation from inspiraling, stellar-mass binaries. Corrections of order M/r ($P^1 N$ corrections) to the lowest-order, Newtonian waveform (2.12) were calculated almost 20 years ago by Wagoner and Will [32]. Calculations of the inspiral rate have recently been extended to $P^{1.5} N$ order, for the case of nonspinning bodies, by Wiseman [33] (after Cutler *et al.* [13] and Poisson [34] had determined the form of the $P^{1.5} N$ correction for the case $\mu/M \ll 1$). By “ $P^x N$ order” we mean that corrections to the quadrupole-formula radiation field and corresponding inspiral rate that are of order $(M/r)^x$ have been taken into account, along with order $(M/r)^x$ corrections to the nonradiative orbital equations which determine, e.g., the orbital frequency at a given separation. [There is no standard convention for “counting” post-Newtonian orders in calculations involving radiation; e.g., some authors refer to the lowest-order radiation field as $P^{2.5} N$. Our own terminology is motivated by the application considered here: since radiation reaction effects *cause* the inspiral, $O(M/r)$ corrections to the quadrupole formula accumulate secularly and have just as large an effect on the phase of the orbit $\phi(f)$ as do $O(M/r)$ corrections to the orbital frequency at a given radius.]

The post-Newtonian waveforms improve upon their Newtonian counterparts in three respects [35, 36]. First, they include contributions from higher-order multipoles of the stress-energy tensor (e.g., mass-octupole and current-quadrupole radiation in addition to the mass-quadrupole term), whose frequencies are different harmonics of the orbital frequency. Second, they include post-Newtonian corrections to the lowest-order expressions for the amplitude of each multipole component. And, most importantly for our purposes, post-Newtonian corrections to the energy $E(r)$ and gravitational wave luminosity $dE/dt(r)$ modify the inspiral rate and thereby the accumulated orbital phase $\Phi(t)$. We can write $h(t)$ schematically as

$$h(t) = \text{Re} \left\{ \sum_{x,m} h_m^x(t) e^{im\Phi(t)} \right\}, \quad (3.1)$$

where x indicates the term's post-Newtonian order, the integer m labels the different harmonics, and $\Phi(t)$ is the orbital phase. Each amplitude h_m^x has the form

$$h_m^x(t) \equiv \frac{\mu M}{D r(t)} g_m^x(M_1/M_2) Q_m^x(\theta, \varphi, \psi, \iota), \quad (3.2)$$

where $r(t)$ is the orbital separation, g_m^x is some function of the mass ratio, and Q_m^x is a function of the source's position on the sky and the orientation of the orbital plane. To connect with the notation of Sec. II and below, we note that the phase $\phi(t)$ of the quadrupole part of the waveform is essentially twice the orbital phase: $\phi(t) = 2\Phi(t) + k$, for some constant k that depends on the relative positions and orientations of the detector and the binary [37]. Thus, the expansion for $h(t)$ through $P^{1.5}N$ order is given by

$$h(t) = \text{Re} [(h_2^0 + h_2^1 + h_2^{1.5}) e^{2i\Phi} + (h_1^{0.5} + h_1^{1.5}) e^{i\Phi} + (h_3^{0.5} + h_3^{1.5}) e^{3i\Phi} + h_4^1 e^{4i\Phi} + h_5^{1.5} e^{5i\Phi}], \quad (3.3)$$

where $\Phi(t)$ has the post-Newtonian expansion

$$\Phi(t) = \Phi^0 + \Phi^1 + \Phi^{1.5} + O((M/r)^2). \quad (3.4)$$

In Eq. (3.4), Φ^x refers to the P^xN order contribution to the orbital phase. As indicated by Eq. (3.4), the term $\Phi^{0.5}$ vanishes identically, as do several omitted terms in Eq. (3.3). The term $h_2^0 e^{2i\Phi^0}$ is just the Newtonian, mass-quadrupole waveform given by Eq. (2.12), while the terms $h_1^{0.5} e^{i\Phi^0(t)}$ and $h_3^{0.5} e^{3i\Phi^0(t)}$ are the lowest order current-quadrupole pieces of the waveform. The term $h_2^{1.5} e^{2i\Phi}$ is the so-called “hereditary” or “tail” term produced by the interaction of the outgoing wave with the binary's gravitational potential [34, 38]. The interested reader can find explicit expressions for the amplitudes h_m^x through P^1N order in Krolak [35].

In Sec. I we argued that the waveform's accumulated phase Φ contains most of the “information” that allows sensitive measurement of the masses of the bodies. Since this paper aims at only an approximate calculation of parameter-estimation accuracies, rather than use the full $P^{1.5}N$ waveform (3.3), we calculate the Fisher informa-

tion matrix (2.7) using the “model” waveform

$$h(t) = \text{Re} \left\{ h_2^0 e^{2i[\Phi^0 + \Phi^1 + \Phi^{1.5}]} \right\}. \quad (3.5)$$

That is, we include P^1N and $P^{1.5}N$ corrections to the phase of the waveform, since these are decisive for extracting the mass and spin parameters of the binary, but we neglect the other post-Newtonian effects that are nominally of the same order. We expect that the values of ΔM_1 and ΔM_2 calculated using Eq. (3.5) will be a reasonable approximation to the error bars one would calculate using the true, general relativistic waveforms (assuming one had access to them).

There is another, practical, reason for the use of the truncated waveform (3.5). As explained in Sec. II, we can simplify the error-estimation analysis by considering only single-detector measurements, and still obtain a reasonable estimate of the accuracies attainable for mass and spin measurements. However, as stated above, each of the amplitudes h_m^x has a different dependence on the angles $(\theta, \varphi, \psi, \iota)$. These angles cannot be measured using one detector alone. The position of the source θ, φ is determined from differences in signal arrival times at (at least) three widely separated detectors [6]. Moreover at least two of the detectors must have different orientations to obtain even a crude estimate of the angles ψ, ι (which describe the principal polarization axis of the wave and the angle between the line of sight and the normal to the orbital plane, see Sec. IV below). Thus, to make use of the extra information contained in the post-Newtonian terms that we are omitting in Eq. (3.5), a full detector network would have to be modeled. Hence, for simplicity, in our model waveform (3.5) we omit all of the terms in Eq. (3.3) except for the largest one. (Although we do analyze a general network of detectors in Sec. IV below, that analysis takes advantage of the fact that the phase-evolution information and the amplitude/polarization information in the measured waveforms are largely independent, and — complementary to this section's analysis — focuses on the amplitude/polarization information alone.)

A. Parameter estimation neglecting spin effects

In this section we estimate how well the masses M_1 and M_2 could be determined from the waveform, if we knew *a priori* (or *a posteriori* by some independent means), that both bodies had negligible spin. Note that this is different from the situation where the spins *happen* to be zero, but where we have no knowledge of this fact apart from the information contained in the gravitational waveform.

In fact, it would not be justified to assume *a priori* that compact objects found in binaries have negligible spins. For one thing, the formation of close binaries generally involves a period of mass transfer, which would tend to spin up the accreting body. Observationally, there are three known NS-NS binaries that will merge within a Hubble time; at the time of merger, the pulsars in these binaries will all be spinning at roughly 1–2% of their maximum possible angular velocities [2]. (The spin rates at

merger will be roughly a factor of 2 smaller than current values, due to magnetic dipole radiation.) We show in Sec. III B below that allowing for spins of this magnitude increases the resulting error bars for mass measurements by roughly a factor of 2, compared to the error bars obtained if spins are assumed to vanish. Nevertheless, we feel it is instructive to calculate the Fisher information matrix neglecting spin effects (i.e., assuming the spins are negligible *a priori*), both to illustrate the inclusion of post-Newtonian terms and to provide a basis for comparison with the results obtained when we include spins.

We now briefly derive the $P^{1.5}N$ corrections to the phase of the waveform. Through $P^{1.5}N$ order, the orbital frequency, energy, and energy-loss rates (for nonspinning bodies) are [32, 33]

$$\Omega(r) = \frac{M^{1/2}}{r^{3/2}} \left[1 + \left(\frac{-3}{2} + \frac{\mu}{2M} \right) \frac{M}{r} + O\left(\left(\frac{M}{r}\right)^2\right) \right], \quad (3.6)$$

$$E(r) = \frac{-\mu M}{2r} \left[1 + \left(\frac{-7}{4} + \frac{\mu}{4M} \right) \frac{M}{r} + O\left(\left(\frac{M}{r}\right)^2\right) \right], \quad (3.7)$$

$$\begin{aligned} \frac{dE}{dt}(r) = -\frac{32}{5} (\mathcal{M}\Omega)^{10/3} & \left[1 + \left(\frac{-1247}{336} + \frac{35\mu}{12M} \right) \left(\frac{M}{r} \right) \right. \\ & \left. + 4\pi \left(\frac{M}{r} \right)^{3/2} + O\left(\left(\frac{M}{r}\right)^2\right) \right], \end{aligned} \quad (3.8)$$

where r is the orbital separation in de Donder gauge (the standard gauge choice for post-Newtonian calculations), and t refers to time measured at infinity.

Defining $f \equiv \Omega/\pi$, the frequency (in cycles/sec) of the quadrupolar part of the gravitational waves, we combine Eqs. (3.6)–(3.8) to obtain

$$df/dt = \frac{96}{5} \pi^{8/3} \mathcal{M}^{5/3} f^{11/3} \left[1 - \left(\frac{743}{336} + \frac{11\mu}{4M} \right) (\pi M f)^{2/3} + 4\pi (\pi M f) + O((\pi M f)^{4/3}) \right]. \quad (3.9)$$

In Eq. (3.9) and below, we use $(\pi M f)^{1/3}$ as our post-Newtonian expansion parameter, instead of $(M/r)^{1/2}$. We note that $(\pi M f)^{1/3}$ equals $(M/r)^{1/2}$ up to but not including terms of order $(M/r)^{3/2}$. This change of variables is advantageous because the frequency of the wave is a directly measurable, gauge-independent quantity (unlike the radius of the orbit). Equation (3.9) can be easily integrated to obtain $t(f)$ and $\phi(f)$, where $\phi \equiv \pi \int f dt$ is the phase of the waveform. Defining $x \equiv (\pi M f)^{2/3}$, we find that

$$\begin{aligned} t(f) = t_c - 5(8\pi f)^{-8/3} \mathcal{M}^{-5/3} & \left[1 + \frac{4}{3} \left(\frac{743}{336} + \frac{11\mu}{4M} \right) x \right. \\ & \left. - \frac{32\pi}{5} x^{3/2} + O(x^2) \right], \end{aligned} \quad (3.10)$$

$$\begin{aligned} \phi(f) = \phi_c - 2[8\pi \mathcal{M} f]^{-5/3} & \left[1 + \frac{5}{3} \left(\frac{743}{336} + \frac{11\mu}{4M} \right) x \right. \\ & \left. - 10\pi x^{3/2} + O(x^2) \right], \end{aligned} \quad (3.11)$$

where, as in Sec. II, we define t_c and ϕ_c by $t \rightarrow t_c$ and $\phi \rightarrow \phi_c$ as $f \rightarrow \infty$.

Using Eqs. (3.10) and (3.11) and the stationary phase approximation, we can repeat the analysis of Sec. II to obtain $\tilde{h}(f)$. As before, we (crudely) model the end of the inspiral at $r \approx 6M$ by setting $\tilde{h}(f) = 0$ for $f > (6^{3/2}\pi M)^{-1}$. The stationary phase result then becomes

$$\tilde{h}(f) = \begin{cases} \mathcal{A} f^{-7/6} e^{i\Psi}, & 0 < f < (6^{3/2}\pi M)^{-1}, \\ 0, & (6^{3/2}\pi M)^{-1} < f, \end{cases} \quad (3.12)$$

where $\mathcal{A} = (Q/D) \mathcal{M}^{5/6}$ and

$$\begin{aligned} \Psi(f) = 2\pi f t_c - \phi_c - \pi/4 & + \frac{3}{4} (8\pi \mathcal{M} f)^{-5/3} \\ & \times \left[1 + \frac{20}{9} \left(\frac{743}{336} + \frac{11\mu}{4M} \right) x - 16\pi x^{3/2} \right]. \end{aligned} \quad (3.13)$$

Note that the post-Newtonian correction terms in square brackets in Eq. (3.13) have their greatest effect on the phase of $\tilde{h}(f)$ at low frequencies, because they are multiplied by the overall factor $f^{-5/3}$. This may seem counterintuitive, since the post-Newtonian corrections to the inspiral rate are largest at small r , or high f ; however the high-frequency portion of the waveform contains far fewer cycles, so the cumulative effect of PN corrections on the waveform's phase is smaller there.

Our model waveform (3.13) for nonspinning bodies depends on five parameters: \mathcal{A} , ϕ_c , \mathcal{M} , μ , and t_c . It is actually somewhat simpler to compute and interpret the Fisher information matrix Γ_{ij} in terms of the following modified parameters for which the rms errors are rescaled: $\ln \mathcal{A}$, ϕ_c , $\ln \mathcal{M}$, $\ln \mu$, and $f_0 t_c$, where f_0 is some fiducial frequency. With respect to these parameters, the derivatives of $\tilde{h}(f)$ are [39]

$$\frac{\partial \tilde{h}(f)}{\partial \ln \mathcal{A}} = \tilde{h}(f), \quad (3.14a)$$

$$\frac{\partial \tilde{h}(f)}{\partial f_0 t_c} = 2\pi i (f/f_0) \tilde{h}(f), \quad (3.14b)$$

$$\frac{\partial \tilde{h}(f)}{\partial \phi_c} = -i \tilde{h}(f), \quad (3.14c)$$

$$\frac{\partial \tilde{h}(f)}{\partial \ln \mathcal{M}} = -\frac{5i}{4} (8\pi \mathcal{M} f)^{-5/3} \tilde{h}(f) \times \left[1 + \frac{55\mu}{6M} x + 8\pi x^{3/2} \right], \quad (3.14d)$$

$$\begin{aligned} \frac{\partial \tilde{h}(f)}{\partial \ln \mu} &= \frac{3i}{4} (8\pi \mathcal{M} f)^{-5/3} \tilde{h}(f) \\ &\times \left[\left(\frac{-3715}{756} + \frac{55\mu}{6M} \right) x + 24\pi x^{3/2} \right]. \end{aligned} \quad (3.14e)$$

Using Eqs. (3.14) and the noise spectrum (2.1), we have numerically computed Γ_{ij} , its inverse Σ^{ij} , and the corresponding errors $\Delta\phi_c = \sqrt{\Sigma^{\phi_c \phi_c}}$, etc. Since our model waveform includes post-Newtonian corrections to the phase but not to the amplitude, Σ^{ij} is block diagonal: $\Sigma^{\ln \mathcal{A} j} = 0$ for $j = \phi_c, \ln \mathcal{M}, \ln \mu$, or $f_0 t_c$. Hence, $\Delta\mathcal{A}/\mathcal{A} = (S/N)^{-1}$, while errors in \mathcal{A} are uncorrelated with errors in the other parameters. Table I lists $\Delta\phi_c$, Δt_c , $\Delta\mathcal{M}/\mathcal{M}$, and $\Delta\mu/\mu$ for a range of values of M_1 and M_2 . The results in Table I are for a single detector and are normalized to $S/N = 10$. For measurements by a detector network, the rms errors $\Delta\mathcal{M}/\mathcal{M}$, and $\Delta\mu/\mu$ will be approximately those given Table I, but with S/N replaced by ρ , the combined signal-to-noise (1.3) of the network. As explained in Sec. II, this is because each detector provides almost-independent estimates of \mathcal{M} and μ . The result we particularly wish to draw attention to is *if spins can be treated as negligible then μ can typically be measured to $\sim 1\%$, while \mathcal{M} can be determined to $\sim 0.01\text{--}0.1\%$* .

Table I also lists the correlation coefficient $c_{\mathcal{M}\mu} \equiv \Sigma^{\mathcal{M}\mu}/(\Sigma^{\mathcal{M}\mathcal{M}} \Sigma^{\mu\mu})^{1/2}$, a dimensionless ratio indicating the degree to which errors in \mathcal{M} and μ are correlated. The quantity $c_{\mathcal{M}\mu}$ is independent of S/N , and by definition satisfies $c_{\mathcal{M}\mu} \in [-1, 1]$. We find that typically $|c_{\mathcal{M}\mu}| > 0.90$, indicating that the errors in \mathcal{M} and μ are strongly correlated. This strong correlation implies that there exists a linear combination of \mathcal{M} and μ which can be determined much more accurately than either \mathcal{M} or μ individually [40]. In particular, $\Delta [\mathcal{M} - (\Sigma^{\mathcal{M}\mu}/\Sigma^{\mu\mu}) \mu]$ is smaller than $\Delta\mathcal{M}$ by a factor of $\sim (1 - c_{\mathcal{M}\mu}^2)^{-1/2}$. Indeed, the value of $\Delta [\mathcal{M} - (\Sigma^{\mathcal{M}\mu}/\Sigma^{\mu\mu}) \mu]$ computed using our $P^{1.5N}$ waveform (3.12) is approximately the same as $\Delta\mathcal{M}$ [cf. Eqs. (2.25) above] computed using the Newtonian waveform (2.20) [40].

How accurately can M_1 and M_2 be determined? While it is straightforward to answer this question when the mass ratio is large, we shall see that some care is required when M_1 and M_2 are comparable, since in this case the distribution of errors in M_1, M_2 is non-Gaussian. Recall that we have adopted the convention that $M_1 \geq M_2$. Then we have

$$M_{1,2} = \frac{1}{2} [\mathcal{M}^{5/2} \mu^{-3/2} \pm (\mathcal{M}^5 \mu^{-3} - 4\mathcal{M}^{5/2} \mu^{-1/2})^{1/2}]. \quad (3.15)$$

Using Eq. (3.15), $\Sigma^{M_1 M_1}$ and $\Sigma^{M_2 M_2}$ can be expressed as linear combinations of $\Sigma^{\mathcal{M}\mathcal{M}}$, $\Sigma^{\mathcal{M}\mu}$, and $\Sigma^{\mu\mu}$. However it is clear from Table I that in practice the $\Sigma^{\mu\mu}$ term will give the dominant contribution. Neglecting the terms proportional to $\Sigma^{\mathcal{M}\mathcal{M}}$ and $\Sigma^{\mathcal{M}\mu}$, we find that

$$\Sigma^{M_1 M_1} = \Sigma^{\mu\mu} \left[\frac{M(\mu - 3M_1)}{2\mu(M_1 - M_2)} \right]^2, \quad (3.16a)$$

$$\Sigma^{M_2 M_2} = \Sigma^{\mu\mu} \left[\frac{M(\mu - 3M_2)}{2\mu(M_1 - M_2)} \right]^2. \quad (3.16b)$$

For example, if $M_1 = 10M_\odot$ and $M_2 = 1.4M_\odot$, Eqs. (3.16) imply that $\Delta M_1/M_1 \approx 1.9\Delta\mu/\mu$ and $\Delta M_2/M_2 \approx 1.4\Delta\mu/\mu$.

While the expressions (3.16) for $\Sigma^{M_1 M_1}$ and $\Sigma^{M_2 M_2}$ should be adequate for estimating the distribution of errors when $M_1 \gg M_2$, these expressions unfortunately diverge when $M_1 = M_2$. This divergence is due to the fact that the Jacobian of the transformation $(M_1, M_2) \rightarrow (\mathcal{M}, \mu)$ vanishes when $M_1 = M_2$. Of course, the rms mass measurement errors do not actually become infinite. Rather, the *linear* approximation that one typically uses to estimate rms errors loses its validity. That is, the approximation that

$$\begin{aligned} \Delta\tilde{h} \approx & \frac{\partial\tilde{h}}{\partial\mathcal{A}} \Delta\mathcal{A} + \frac{\partial\tilde{h}}{\partial\phi_c} \Delta\phi_c + \frac{\partial\tilde{h}}{\partial t_c} \Delta t_c \\ & + \frac{\partial\tilde{h}}{\partial M_1} \Delta M_1 + \frac{\partial\tilde{h}}{\partial M_2} \Delta M_2, \end{aligned} \quad (3.17)$$

for variations $\Delta\tilde{h}$ of a size determined by typical realizations of the noise, becomes inaccurate when $M_1 - M_2 \rightarrow 0$, as $\partial\tilde{h}/\partial M_1 + \partial\tilde{h}/\partial M_2 \rightarrow 0$ in this limit.

To overcome this problem we proceed as explained in subsection A 7 of Appendix A below, and use the probability distribution function (PDF) for the best-fit values $\hat{\mathcal{M}}, \hat{\mu}$ of the parameters \mathcal{M}, μ , which is simply a Gaussian centered on the true parameters \mathcal{M}, μ . (Thus, we are considering so-called frequentist errors, cf. A 2 of Appendix A below.) Let \hat{M}_1 and \hat{M}_2 be the corresponding best-fit values for the individual masses. Substituting into this PDF the transformation $\hat{\mathcal{M}} = \mathcal{M}(\hat{M}_1, \hat{M}_2)$ and $\hat{\mu} = \mu(\hat{M}_1, \hat{M}_2)$ yields a non-Gaussian PDF for \hat{M}_1, \hat{M}_2 , from which we can calculate the 95% confidence limits for \hat{M}_1 and \hat{M}_2 . The use of confidence limits is somewhat crude, in the sense that it leaves out much of the information contained in the PDF, but it is suitable for our purpose of determining *roughly* how accurately these quantities can be measured. Since $\Delta\mathcal{M}$ is very small, for the purposes of this discussion we can assume \mathcal{M} has been measured exactly. Let $\tilde{\mu}$ is the true value of the binary's reduced mass. Then with 95% confidence $\hat{\mu}$ lies in the interval

$$\tilde{\mu} - 2\Delta\mu < \hat{\mu} < \tilde{\mu} + 2\Delta\mu, \quad (3.18)$$

where $\Delta\mu \equiv (\Sigma^{\mu\mu})^{1/2}$ is determined from the variance-covariance matrix. Roughly speaking, a necessary condition for the distribution of \hat{M}_1 and \hat{M}_2 to be Gaussian is that $\tilde{\mu} + 2\Delta\mu < 2^{-4/5} \mathcal{M}$ (so that the μ 's 95% confidence interval does not include the equal-mass case).

From Eqs. (3.15) and (3.18) we obtain the following 95% confidence limits on \hat{M}_1 and \hat{M}_2 :

$$M_1(\mathcal{M}, \tilde{\mu} + 2\Delta\mu) < \hat{M}_1 < M_1(\mathcal{M}, \tilde{\mu} - 2\Delta\mu), \quad (3.19a)$$

$$M_2(\mathcal{M}, \tilde{\mu} - 2\Delta\mu) < \hat{M}_2 < M_2(\mathcal{M}, \tilde{\mu} + 2\Delta\mu), \quad (3.19b)$$

where the functions M_1 and M_2 are given by Eq. (3.15) above. If $\tilde{\mu} + 2\Delta\mu$ is greater than the maximum allowed value of μ , then one should replace $\tilde{\mu} + 2\Delta\mu$ by $2^{-4/5} \mathcal{M}$ in Eqs. (3.19). For example, if $\mathcal{M} = 1.219M_\odot$, $\tilde{\mu} = 0.7M_\odot$, and $\Delta\mu/\tilde{\mu} = 0.004$ (the NS-NS case), then one can state with 95% confidence that \hat{M}_1 and \hat{M}_2 lie in the ranges

$1.4M_{\odot} < \hat{M}_1 < 1.65M_{\odot}$ and $1.2M_{\odot} < \hat{M}_2 < 1.4M_{\odot}$. Thus M_1 and M_2 are determined with much less accuracy than μ when the two masses are roughly equal.

B. Parameter estimation including spin effects

We now present a rough calculation of the degree to which mass measurement accuracy is degraded when the spins cannot be assumed to be negligible. For the same reasons as in Sec. III A, we incorporate the effects of spins on the phase of the waveform, but neglect their effects on the waveform amplitude.

Let \vec{S}_1 and \vec{S}_2 be the spin angular momenta of the two bodies, and let \vec{L} be the total orbital angular momentum. We define the unit vector \hat{L} by $\hat{L} \equiv \vec{L}/|\vec{L}|$. Then Kidder, Will, and Wiseman [41] have shown that, due to an “ $\vec{L} \cdot \vec{S}$ ” term in the two-body force law as well as spin corrections to the expressions for the system’s mass-quadrupole and current-quadrupole moments, Eq. (3.9) becomes modified at $P^{1.5}N$ order to

$$\begin{aligned} df/dt = \frac{96}{5}\pi^{8/3}\mathcal{M}^{5/3}f^{11/3} &\left[1 - \left(\frac{743}{336} + \frac{11\mu}{4M} \right)x \right. \\ &\left. + (4\pi - \beta)x^{3/2} + O(x^2) \right], \end{aligned} \quad (3.20)$$

where again $x \equiv (\pi M f)^{2/3}$, and where

$$\begin{aligned} \beta \equiv M^{-2}\hat{L} \cdot &\left[\left(\frac{113}{12} + \frac{25}{4}\frac{M_2}{M_1} \right)\vec{S}_1 \right. \\ &\left. + \left(\frac{113}{12} + \frac{25}{4}\frac{M_1}{M_2} \right)\vec{S}_2 \right]. \end{aligned} \quad (3.21)$$

Through $P^{1.5}N$ order, the six components of \vec{S}_1 and \vec{S}_2 affect the waveform’s phase only via the particular combination (3.21). (Of course, other combinations appear at higher order.)

We now discuss the magnitude of the correction due to β . For black holes, one has a strict upper limit on the magnitude of the spins: $|\vec{S}_i| \leq M_i^2$. This is also roughly the upper limit for neutron stars, though the actual upper limit depends on the (uncertain) nuclear equation of state. We can therefore estimate the maximum size of β by considering the case where the spins are aligned with \vec{L} , and where $|\vec{S}_1|/M_1^2 = |\vec{S}_2|/M_2^2 = 1$. In this case $\beta = \frac{113}{12} - \frac{19}{12}(4\mu/M)$. This maximum value β_{\max} is always within 10% of 8.5, regardless of the mass ratio.

The $P^{1.5}N$ order equations of motion also contain “ $\vec{L} \times \vec{S}$ ” terms, which do not directly affect df/dt , but do so indirectly by causing the directions of \hat{L} , \vec{S}_1 , and \vec{S}_2 to precess during the inspiral — essentially the Lense-Thirring effect. The equations describing the secular evolution of \hat{L} , \vec{S}_1 , and \vec{S}_2 through P^2N order are [42]

$$\begin{aligned} \frac{d\hat{L}}{dt} = r^{-3} &\left[a_1\vec{S}_1 + a_2\vec{S}_2 \right. \\ &\left. - \frac{3}{2}\frac{(\vec{S}_2 \cdot \hat{L})\vec{S}_1 + (\vec{S}_1 \cdot \hat{L})\vec{S}_2}{L} \right] \times \hat{L}, \end{aligned} \quad (3.22a)$$

$$\frac{d\vec{S}_1}{dt} = r^{-3} \left[a_1 L \hat{L} + \frac{1}{2}\vec{S}_2 - \frac{3}{2}(\vec{S}_2 \cdot \hat{L})\hat{L} \right] \times \vec{S}_1, \quad (3.22b)$$

$$\frac{d\vec{S}_2}{dt} = r^{-3} \left[a_2 L \hat{L} + \frac{1}{2}\vec{S}_1 - \frac{3}{2}(\vec{S}_1 \cdot \hat{L})\hat{L} \right] \times \vec{S}_2, \quad (3.22c)$$

where $a_1 = 2 + (3M_2)/(2M_1)$, $a_2 = 2 + (3M_1)/(2M_2)$, $L = |\vec{L}| = \mu\sqrt{Mr}$, and where, to this order, one can use the expression (2.11) for $r(t)$.

The precession of \hat{L} , \vec{S}_1 , and \vec{S}_2 causes β to evolve; $d\beta/dt$ as calculated from Eqs. (3.22) does not vanish identically. Fortunately, however, β is almost conserved by Eqs. (3.22), in the following sense. We integrated these equations numerically from $f=10$ Hz to $f=(6^{3/2}\pi M)^{-1}$, for a wide variety of spin magnitudes, initial spin directions, and mass ratios; we found that β never deviates from its average value by more than ~ 0.25 (or $\sim 0.03\beta_{\max}$). Moreover, the nonconstant part of β is oscillatory, which further diminishes its integrated effect on the waveform’s phase. These properties of the evolution of β are explored analytically and numerically in Appendix B.

The near constancy of β allows a considerable simplification of our model waveform: in Eq. (3.20), we simply take β to be a constant. That is, we treat β as just another parameter on which the signal depends. The Fourier transform of our model waveform, including spin effects, is therefore given by

$$\tilde{h}(f) = \begin{cases} \mathcal{A}f^{-7/6}e^{i\Psi}, & 0 < f < (6^{3/2}\pi M)^{-1}, \\ 0, & (6^{3/2}\pi M)^{-1} < f, \end{cases} \quad (3.23)$$

where now

$$\begin{aligned} \Psi(f) = 2\pi f t_c - \phi_c - \pi/4 &+ \frac{3}{4}(8\pi\mathcal{M}f)^{-5/3} \\ &\times \left[1 + \frac{20}{9}\left(\frac{743}{336} + \frac{11\mu}{4M}\right)x + (4\beta - 16\pi)x^{3/2} \right]. \end{aligned} \quad (3.24)$$

Now, for spinning bodies it is not really correct to treat the amplitude $\mathcal{A} \equiv Q(\theta, \phi, \psi, \iota)D^{-1}\mathcal{M}^{5/6}$ as constant. The precession of the orbital plane described by Eqs. (3.22) causes the angles ψ and ι to vary, and hence $Q(\theta, \phi, \psi, \iota)$ to vary, throughout the inspiral. Typically, the orbital plane precesses around the total angular momentum vector $\vec{J} \equiv \vec{L} + \vec{S}_1 + \vec{S}_2$ roughly 20 times during the observable portion of the inspiral. The result is a sinusoidal modulation of the waveform envelope [8, 43], and the amplitude of the modulation can be large when $|\vec{S}_1|$ or $|\vec{S}_2|$ is comparable to $|\vec{L}|$. Nevertheless, in the interest of simplifying the calculation, in our model waveform (3.23) we take \mathcal{A} to be a constant. We discuss further below the implications of this simplification.

The derivatives $\partial\tilde{h}/\partial\ln\mathcal{A}$, $\partial\tilde{h}/\partial(f_0 t_c)$, and $\partial\tilde{h}/\partial\phi_c$ of the signal (3.23) are given by the same expressions as in Eqs. (3.14). The derivatives of $\tilde{h}(f)$ with respect to $\ln\mathcal{M}$, $\ln\mu$, and β are

$$\begin{aligned} \frac{\partial \tilde{h}(f)}{\partial \ln \mathcal{M}} = -\frac{5i}{4}(8\pi \mathcal{M}f)^{-5/3}\tilde{h}(f) & \left[1 + \frac{55\mu}{6M}x \right. \\ & \left. +(8\pi - 2\beta)x^{3/2} \right], \end{aligned} \quad (3.25a)$$

$$\begin{aligned} \frac{\partial \tilde{h}(f)}{\partial \ln \mu} = \frac{3i}{4}(8\pi \mathcal{M}f)^{-5/3}\tilde{h}(f) & \left[\left(\frac{-3715}{756} + \frac{55\mu}{6M} \right)x \right. \\ & \left. +(24\pi - 6\beta)x^{3/2} \right], \end{aligned} \quad (3.25b)$$

$$\frac{\partial \tilde{h}(f)}{\partial \beta} = 3i(8\pi \mathcal{M}f)^{-5/3}(\pi \mathcal{M}f)\tilde{h}(f). \quad (3.25c)$$

Using Eqs. (3.25) we again compute the variance-covariance matrix Σ^{ij} for a range of values of M_1 and M_2 . One can show that $\Delta\phi_c$, Δt_c , $\Delta\mathcal{M}/\mathcal{M}$, and $\Delta\mu/\mu$ do not depend on the value of β . The simple way to prove this is to make a change of variables from $(\mathcal{A}, \phi_c, t_c, \mathcal{M}, \mu, \beta)$ to $(\mathcal{A}, \phi_c, t_c, \mathcal{M}, \mu, \beta')$, where

$$\beta' \equiv (4\beta - 16\pi)\mathcal{M}^{5/6}\mu^{-3/2}. \quad (3.26)$$

Since the waveform phase $\Psi(f)$ [Eq. (3.24)] depends linearly on $\beta'f^{-2/3}$, the Fisher information matrix calculated with respect to the new variables is independent of β' . This implies that the rms errors in the other parameters, and their correlation coefficients, are independent of the value of β . The values of $\Delta\beta$, $c_{\mathcal{M}\beta}$, and $c_{\mu\beta}$ do depend on β , however.

In Table II we list the rms errors $\Delta\phi_c$, Δt_c , $\Delta\mathcal{M}/\mathcal{M}$, $\Delta\mu/\mu$, and $\Delta\beta$ for the same fiducial binaries that appear in Table I. In computing the results in Table II we use the model of the advanced detector noise curve given by Eq. (2.1). Since we are principally concerned with how

our lack of knowledge of the bodies' spins affects how well we can determine the other parameters, we take the "true" value of β to be zero in all cases. As in Table I, the results in Table II are for a single detector and are normalized to $S/N = 10$; for a detector network, the rms errors $\Delta\mathcal{M}/\mathcal{M}$, and $\Delta\mu/\mu$ and $\Delta\beta$ will be approximately those given in Table II, but with S/N replaced by the combined signal-to-noise ratio ρ .

Summarizing the results of Table II, we find that $\Delta\mathcal{M}/\mathcal{M}$ is roughly an order of magnitude larger than predicted by the Newtonian analysis of Sec. II, but still typically less than 0.1%. Thus, despite the "confusion" introduced by the extra parameters that enter at post-Newtonian order, we conclude that \mathcal{M} can still be measured with remarkable accuracy. However, compared to the case where the bodies are assumed to have negligible spin *a priori*, we see that $\Delta\mu$ has increased by a factor which ranges from 20 to 60.

Table II also reveals the "reason" for this loss of accuracy: the correlation coefficient $c_{\mu\beta}$ is extremely close to -1 [40]. Clearly the strong correlation is due to the fact that the frequency dependence of the " $\vec{L} \cdot \vec{S}$ " term in the expression (3.24) for the waveform phase $\Psi(f)$ is very similar to the frequency dependence of the other post-Newtonian terms in Eq. (3.24). This strong correlation implies that there is a combination of μ and β which can be determined to much higher accuracy than μ itself [40]. Specifically, $\Delta(\mu - (\Sigma^{\mu\beta}/\Sigma^{\beta\beta})\beta)$ is smaller than $\Delta\mu$ by a factor of $\sim(1 - c_{\mu\beta}^2)^{-1/2}$, which is approximately 20–60 for the cases in Table II. Thus the combination $\mu - (\Sigma^{\mu\beta}/\Sigma^{\beta\beta})\beta$ can be determined with approximately the same accuracy that one could achieve for μ , if spin effects could be neglected (cf. Table I). Since both \mathcal{M} and this particular combination of μ and β can be determined to high accuracy, the inspiral gravitational wave measurement essentially constrains the parameters to lie near a thin two-dimensional strip in $(\mathcal{M}, \mu, \beta)$ space. This is

TABLE II. The rms errors for signal parameters and the correlation coefficients $c_{\mathcal{M}\mu}$, $c_{\mathcal{M}\beta}$, and $c_{\mu\beta}$, calculated using spin-dependent waveforms. The results are for a single "advanced" detector, the shape of whose noise curve is given by Eq. (2.1). For the rows marked with a † (and only for those rows), the variance-covariance matrix has been "corrected" to approximately account for the fact that the spin parameter β must satisfy $|\beta| < \beta_{\max} \approx 8.5$. The rms errors are normalized to a signal-to-noise ratio of $S/N = 10$. Except for rows marked with a †, errors scale as $(S/N)^{-1}$, while the correlation coefficients are independent of S/N . Except for rows marked with a †, if β had been chosen nonzero with M_1 and M_2 unchanged, then $\Delta\mathcal{M}/\mathcal{M}$, $\Delta\mu/\mathcal{M}$, and $c_{\mathcal{M}\mu}$ would have been unchanged (but $\Delta\beta$, $c_{\mathcal{M}\beta}$, and $c_{\mu\beta}$ would have been altered). As in Table I, M_1 and M_2 are in units of M_\odot , while Δt_c is in msec. The results for the LIGO-VIRGO network of detectors, for a signal with combined signal-to-noise ratio from all the detectors of 10, will be approximately the same as those shown here; see text.

M_1	M_2	β	$\Delta\phi_c$	Δt_c	$\Delta\mathcal{M}/\mathcal{M}$	$\Delta\mu/\mu$	$\Delta\beta$	$c_{\mathcal{M}\mu}$	$c_{\mathcal{M}\beta}$	$c_{\mu\beta}$
2.0	1.0	0	4.13	1.14	0.034%	8.44%	1.04	-0.988	0.993	-0.9989
1.4	1.4	0	4.09	1.13	0.034%	9.65%	1.24	-0.988	0.993	-0.9991
10	1.4	0	6.24	2.03	0.19%	15.2%	1.99	-0.990	0.994	-0.9994
5	1.4	0	4.89	1.44	0.10%	13.4%	1.73	-0.989	0.994	-0.9992
15	5	0	9.26	3.53	1.06%	76.4%	11.4	-0.992	0.994	-0.99980
15	5	0 †	5.77	2.40	0.64%	45.8%	6.81	-0.978	0.984	-0.9995
10	10	0	9.26	3.53	1.42%	125%	19.5	-0.992	0.994	-0.99988
10	10	0 †	4.13	1.92	0.59%	49.9%	7.79	-0.953	0.964	-0.9992

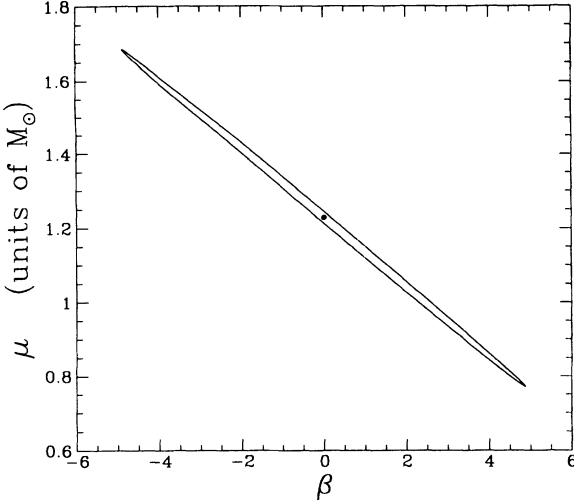


FIG. 3. This plot shows the curve of constant probability on the $\mu\beta$ plane for a NS-BH binary, where μ is the binary's reduced mass and β is a dimensionless spin-related parameter, such that the true values of these parameters lie inside the ellipse with 95% confidence. The strong correlation between possible values of μ and β is evident. To a good approximation, the chirp mass \mathcal{M} is measured to arbitrarily high accuracy. Hence in the three-dimensional space of the parameters $(\mathcal{M}, \mu, \beta)$, the true values of these parameters are confined with high confidence to a thin strip of the above ellipsoidal shape in a plane of constant \mathcal{M} .

illustrated in Fig. 3, for the case of a BH-NS binary.

Up to this point, the formalism we have been using to calculate measurement accuracies neglects *a priori* constraints on the parameters, and thus implicitly assumes that β can take on arbitrary values. This assumption should be adequate as long as the 95% confidence intervals determined from $\Sigma^{\beta\beta}$ are well within the "allowed" range: $|\beta| \leq \beta_{\max} \approx 8.5$. However we see from Table II that this criterion is not satisfied when both bodies are heavier than a few solar masses. For example, when $M_1 = M_2 = 10M_\odot$ we calculate $\Delta\beta = 19.5$. We can (somewhat crudely) incorporate the restricted range of β into our formalism, as follows. We replace the *a priori* information $|\beta| < \beta_{\max}$ at hand by an assumed Gaussian distribution $p^{(0)}(\beta) \propto e^{-\frac{1}{2}(\beta/\beta_{\max})^2}$ for β . In Appendix A we derive an expression for the variance-covariance matrix which incorporates the effect of an (assumed Gaussian) *a priori* probability distribution for the signal parameters. We have used this result [Eq. (A43) below] to reevaluate the variance-covariance matrix for the two high-mass binaries shown in Table II. (Taking the restricted range of β into account makes little difference to the other cases in Table II.) These reevaluated results are marked in Table II with a dagger (\dagger). Again, the rms errors listed are for $S/N = 10$; note however that since $p^{(0)}(\beta)$ is fixed, the rms errors no longer scale simply as $(S/N)^{-1}$. We see that taking the restricted range of β into account leads to the improved estimate $\Delta\mu/\mu \approx 50\%$ in both the high-mass cases.

We mentioned above that in the three known short-period NS-NS binaries, the radio pulsars will, at the time of merger, all have spin angular momenta that are $\lesssim 2\%$

of their maximum possible values. We feel it is an interesting exercise to calculate what measurement accuracies could be attained if we knew that NS's in nature were slowly spinning in general, e.g., if we knew *a priori* that $\beta < 0.02\beta_{\max}$ for NS-NS mergers. Repeating the procedure used above, we take $p^{(0)}(\beta) \propto e^{-\frac{1}{2}(\beta/0.1)^2}$, and we use Eq. (A43) to calculate the variance-covariance matrix for the NS-NS case, for $S/N = 10$. We find $\Delta\mu/\mu \approx 0.9\%$, which is roughly twice the value obtained in Sec. III A, where spin effects were taken to be completely negligible.

We turn again to the question of how accurately the individual masses can be measured. The procedure for calculating ΔM_1 and ΔM_2 in terms of $\Delta\mathcal{M}$ and $\Delta\mu$ is of course the same as described in Sec. III A. Thus for the BH-NS case, using the fact that $\Delta\mu/\mu \approx 15\%$, we find from Eqs. (3.16) that $\Delta M_1/M_1 \approx 30\%$ and $\Delta M_2/M_2 \approx 20\%$. In Sec. III A we explained that the distribution of errors in M_1 and M_2 will be non-Gaussian if $\mu + 2\Delta\mu > 2^{-4/5}\mathcal{M}$. By this criterion, if $\Delta\mu/\mu \approx 15\%$, then we can reliably estimate ΔM_1 and ΔM_2 by using Eqs. (3.16) only if $M_1/M_2 \geq 5.5$.

Again, even when the Gaussian approximation is invalid, one can still use Eqs. (3.19) to place 95% confidence limits on M_1 and M_2 . Consider again the NS-NS case, which we looked at in this context in Sec. III A, with the *true* values of the masses being $M_1 = M_2 = 1.4M_\odot$. Then $\mathcal{M} = 1.22M_\odot$, and, using the 2σ error bar indicated by Table II (for $S/N = 10$) we see that, 95% of the time, the observers would measure μ to be between $0.56M_\odot$ and $0.70M_\odot$. Correspondingly, the measured values of M_1 and M_2 would lie in the ranges $1.4M_\odot < M_1 < 3.2M_\odot$ and $0.7M_\odot < M_2 < 1.4M_\odot$. Thus, in the NS-NS case, measuring μ to within 20% means determining the individual masses only to within a factor of ~ 2 . The constraints obtained on M_1 and M_2 , for this case and the BH-NS case, are illustrated in Fig. 4.

Finally, we repeat these calculations using the flatter spectrum (2.2) instead of (2.1) as our model of the advanced detector noise. The results are shown in Table III. We see that the main conclusions which we drew from Table II are unchanged, but that (for fixed signal-to-noise) the relative errors $\Delta\mathcal{M}/\mathcal{M}$ and $\Delta\mu/\mu$ are a factor of ~ 1.5 times smaller with the flatter noise spectrum (2.2). This is presumably due to the fact that noise spectrum (2.2) exhibits better sensitivity at low frequencies, where most of the gravitational wave cycles (and hence most of the sensitivity) come from.

C. Caveats and future work

Since the results in Tables I–III were obtained using several approximations and simplifying assumptions, we feel that it is useful to collect the most important of these in one place. They are as follows.

First, we restricted attention to statistical errors arising from detector noise. In practice, theoretical template waveforms will be quite difficult to compute accurately [8, 13]. Hence some systematic error may also arise from fitting the data to imperfect template waveforms. Cur-

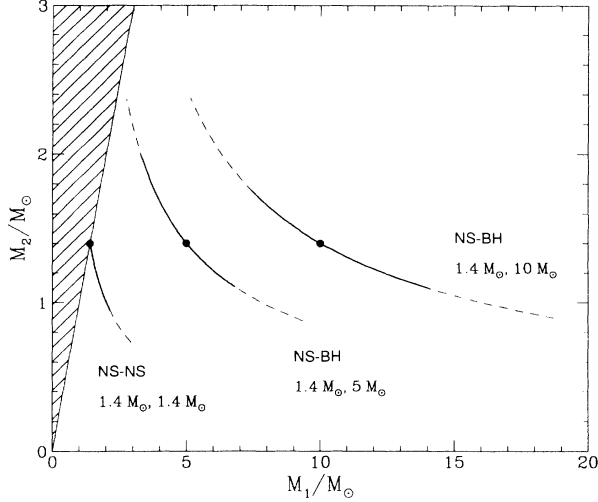


FIG. 4. A diagram showing the information obtained from the gravitational wave signal, constraining the individual masses M_1 and M_2 of the binary components, in various cases. Because of the highly accurate measurement of the chirp mass \mathcal{M} in each case, the individual masses are essentially constrained to lie on a curve of constant $\mathcal{M} \equiv (M_1 M_2)^{3/5} (M_1 + M_2)^{-1/5}$ in the $M_1 M_2$ plane. The measured value of \mathcal{M} provides a sharp lower bound for the larger mass M_1 , and a sharp upper bound for the smaller mass M_2 , since the constant- \mathcal{M} curves terminate sharply at the forbidden, hatched region. The measurement of the reduced mass μ gives some (but not much) information about where along the constant \mathcal{M} curve the binary is most likely to be located. In each case, the solid circles show the true values of M_1 and M_2 , the solid curve denotes the 68% (1σ) confidence interval, and the dashed extension denotes the 95% (2σ) confidence interval. The detector noise spectrum (2.1) was assumed.

rently a large effort is underway in the relativity community to calculate templates sufficiently accurately that these systematic errors will be smaller than the statistical errors due to noise — at least $P^2 N$ and possibly higher order templates will be required. We note that template inaccuracies, while giving rise to important systematic errors in parameter extraction, will not significantly diminish our ability to detect the waves [8].

Second, we assumed the “advanced LIGO” noise-curve shape, for which we have used two estimates: Eq. (2.1) and Eq. (2.2). As emphasized above, these are only

rough estimates of the spectral shape that the LIGO and VIRGO detectors will actually achieve. We have seen, however, that our results do not depend very sensitively on the exact shape of the noise spectrum.

Third, we have used the approximate, linearized error-estimation formalism described in Sec. II B and Appendix A; the rms errors so calculated are guaranteed to be accurate only in the limit that the errors are small. When the errors are so large that the linearized approach is invalid, then our approach will probably generally underestimate the true variances. To avoid the limitations of the linearized error analysis, we are currently performing a Monte Carlo simulation of the parameter extraction process.

Fourth, we calculated the variance-covariance matrix Σ^{ij} using the simplified model waveform (3.23), which is qualitatively inaccurate in a number of respects. In particular, our model waveform depends on the spins of the two bodies only through a single parameter, β . We have neglected the spin-induced precession of the orbital plane, which also arises at $P^{1.5}N$ order, and we have neglected the effect of the spin-spin coupling on inspiral rate, which arises at P^2N order. We have also neglected higher-order multipole radiation (except insofar as the energy carried away by the higher multipoles affects the inspiral rate), and have only crudely modeled the cutoff of the waveform during the bodies’ final tidal-disruption, plunge, or coalescence. (In particular, we have made no attempt to model the spin dependence of the cutoff.)

It is unclear to us whether the inadequacies of our model waveform have led us to underestimate or overestimate parameter-extraction accuracies. On the one hand, the P^2N spin-spin interaction term that we have neglected would, if included, inevitably lead to some degradation of parameter-extraction accuracy (as always happens when there are more parameters to fit for). On the other hand, it seems clear that the effect on $\Delta\mu$ of adding the spin-spin term to the waveform will be far less dramatic than the inclusion of the spin-orbit term β , for two reasons: (i) as shown by Kidder *et al.* [41], for the BH-NS and NS-NS cases, the effect of the spin-spin term on the accumulated phase of the waveform is a factor of at least 20 smaller than the effect of the spin-orbit term and (ii) the correlation coefficient $|c_{\mu\beta}|$ is so close to 1 because the frequency dependences of the μ and β terms in the waveform phase $\Psi(f)$ are so similar; the μ and spin-spin terms are less similar in their frequency dependence.

TABLE III. Measurement accuracies, including spins, as in Table II except that we take the shape of the noise curve to be given by Eq. (2.2).

M_1	M_2	β	$\Delta\phi_c$	Δt_c	$\Delta\mathcal{M}/\mathcal{M}$	$\Delta\mu/\mu$	$\Delta\beta$	$c_{\mathcal{M}\mu}$	$c_{\mathcal{M}\beta}$	$c_{\mu\beta}$
2.0	1.0	0	2.21	0.47	0.021%	5.12%	0.641	-0.986	0.992	-0.9988
1.4	1.4	0	2.19	0.46	0.021%	5.84%	0.757	-0.986	0.992	-0.9990
10	1.4	0	3.90	1.06	0.13%	10.1%	1.33	-0.990	0.994	-0.9993
5	1.4	0	2.81	0.66	0.065%	8.47%	1.11	-0.988	0.993	-0.9992
15	5	0	6.72	2.40	0.75%	55.1%	8.18	-0.992	0.994	-0.99980
15	5	0 †	4.95	1.85	0.55%	39.7%	5.90	-0.985	0.989	-0.9996
10	10	0	6.72	2.40	1.00%	90.0%	14.0	-0.992	0.994	-0.99988
10	10	0 †	3.71	1.49	0.53%	46.7%	7.27	-0.972	0.978	-0.9995

Finally, by neglecting higher-order multipoles, spin-precession effects, and the details of the final plunge, we have effectively thrown away information that would be contained in the true waveform. In a more complete analysis, this “additional” information could perhaps decrease measurement uncertainties. In particular, if in some cases the spin-related modulation of the waveform carries substantial information about β , then it is clear from Fig. 2 that $\Delta\mu$ and consequently ΔM_1 and ΔM_2 could be reduced by large factors. This is an important possibility which we are currently investigating.

IV. ACCURACY OF DISTANCE MEASUREMENTS

A. Overview

In the previous sections we have investigated how accurately the masses of the inspiraling compact objects can be measured from the phase evolution of the detected gravitational waveforms. The other interesting parameters that are measurable from the outputs of a network of detectors are the distance D to the source, and its position on the sky. These parameters will be encoded in the amplitudes, phases, and arrival times of the signals $h_a(t)$ read out from the detectors. At least three geographically separated detectors will be needed in order to determine the distance [6]. We start by describing, in detail, the dependence of the signals $h_a(t)$ on the binary’s distance and sky location.

Let \mathbf{x}_a be the position and \mathbf{d}_a be the polarization tensor of the a th detector in a detector network. By polarization tensor we mean that tensor \mathbf{d}_a for which the detector’s output is given in terms of the waves’ transverse traceless strain tensor $\mathbf{h}(\mathbf{x}, t)$ by

$$h_a(t) = \mathbf{d}_a : \mathbf{h}(\mathbf{x}_a, t). \quad (4.1)$$

Here the colon denotes a double contraction. If the arms of the detector are in the directions of the unit vectors l and \mathbf{m} , then $\mathbf{d}_a = (l \otimes l - \mathbf{m} \otimes \mathbf{m})/2$ [45].

We introduce a spherical polar coordinate system (θ, φ) centered at the Earth so that the axis $\theta = 0$ is the Earth’s axis of rotation. The angle φ is longitude and $\pi/2 - \theta$ is North latitude for $\theta < \pi/2$. Let $\mathbf{n} = (\sin \theta \cos \varphi, \sin \theta \sin \varphi, \cos \theta)$ be the unit vector in the direction (θ, φ) , and let \mathbf{e}_n^+ and \mathbf{e}_n^\times be a basis for the transverse traceless tensors perpendicular to \mathbf{n} . If we demand in the usual way that $\mathbf{e}_n^A : \mathbf{e}_n^B = 2\delta^{AB}$, for $A, B = +, \times$, then this basis is unique up to rotations of the form

$$\mathbf{e}^+ + i\mathbf{e}^\times \rightarrow e^{2i\Delta\psi}(\mathbf{e}^+ + i\mathbf{e}^\times). \quad (4.2)$$

The quantities

$$F_a^A(\mathbf{n}) \equiv \mathbf{e}_n^A : \mathbf{d}_a, \quad (4.3)$$

for $A = +, \times$, are the so-called detector beam-pattern functions for the a th detector [12].

Consider a coalescing binary source in the direction \mathbf{n} . As in Sec. III B, let $\hat{\mathbf{L}}$ denote the unit vector in the

direction of the binary’s orbital angular momentum, and let

$$v = \cos \iota = \hat{\mathbf{L}} \cdot \mathbf{n}, \quad (4.4)$$

so that ι is the inclination angle of the orbit to the line of sight. As seen from the Earth, the orbit looks elliptical, and the principal axes of the ellipse give a preferred polarization basis $\mathbf{e}'^+, \mathbf{e}'^\times$ for the waves. Specifically, we define

$$\mathbf{e}'_x = \frac{\mathbf{n} \times \hat{\mathbf{L}}}{\|\mathbf{n} \times \hat{\mathbf{L}}\|}, \quad (4.5)$$

$$\mathbf{e}'_y = \frac{-\mathbf{n} \times \mathbf{e}'_x}{\|\mathbf{n} \times \mathbf{e}'_x\|}, \quad (4.6)$$

where the minus sign is inserted to accord with standard conventions; the waves propagate in the direction $-\mathbf{n}$. The preferred basis is $\mathbf{e}'^+ = \mathbf{e}'_x \otimes \mathbf{e}'_x - \mathbf{e}'_y \otimes \mathbf{e}'_y$, $\mathbf{e}'^\times = \mathbf{e}'_x \otimes \mathbf{e}'_y + \mathbf{e}'_y \otimes \mathbf{e}'_x$. In terms of this basis, the waves’ strain tensor is $\mathbf{h}(t) = h_+(t)\mathbf{e}'^+ + h_\times(t)\mathbf{e}'^\times$, where in the quadrupole-moment approximation the waveforms $h_+(t)$ and $h_\times(t)$ are as given in, e.g., Ref. [12]. Taking the Fourier transform we find

$$\tilde{h}_A(f) = \chi_A(v) \tilde{h}_0(f), \quad (4.7)$$

where $\chi_+(v) = (1 + v^2)/2$, $\chi_\times(v) = -iv$, and

$$\tilde{h}_0(f) = \sqrt{\frac{5}{24}} \pi^{-2/3} D^{-1} \mathcal{M}^{5/6} f^{-7/6} \exp[i\Psi(f)] \quad (4.8)$$

for $f \geq 0$. The phase $\Psi(f)$ is the same as previously given in Eq. (3.24), and depends only on the parameters \mathcal{M} , μ , β , t_c , and ϕ_c .

If we fix a polarization basis $\mathbf{e}^+, \mathbf{e}^\times$, then we have

$$\mathbf{e}'^A = R_B^A(2\psi) \mathbf{e}^B \quad (4.9)$$

for some polarization angle ψ , where R_B^A is the rotation matrix

$$R_B^A(2\psi) = \begin{pmatrix} \cos(2\psi) & \sin(2\psi) \\ -\sin(2\psi) & \cos(2\psi) \end{pmatrix}. \quad (4.10)$$

The conventional definitions of $\mathbf{e}^+, \mathbf{e}^\times$ and the corresponding definition of ψ for a single detector are given in Refs. [12, 43]. A network of several detectors, however, determines a different preferred basis $\mathbf{e}^+, \mathbf{e}^\times$ (see below), so for the moment we allow the basis to be arbitrary and define ψ via Eq. (4.9). By combining Eqs. (4.1), (4.3), (4.7), and (4.9) we obtain the signal read out from the a th detector:

$$\tilde{h}_a(f) = R_B^A(2\psi) \chi_A(v) F_a^B(\mathbf{n}) e^{2\pi i \tau_a f} \tilde{h}_0(f), \quad (4.11)$$

where $\tau_a = -\mathbf{n} \cdot \mathbf{x}_a$ [46]. The first three factors in Eq. (4.11) taken together are proportional to the quantity $Q(\theta, \varphi, \psi, \iota)$ that appears in Eqs. (2.12) and (2.20).

Now the overall amplitude \mathcal{A} of the signal at one detector can be measured to an accuracy (cf. Sec. II)

$$\frac{\Delta \mathcal{A}}{\mathcal{A}} = \frac{1}{\rho_a}, \quad (4.12)$$

where $\rho_a = (h_a | h_a)^{1/2}$ is the signal-to-noise ratio (SNR) measured at that detector. Since

$$\mathcal{A} \propto \frac{Q(\theta, \varphi, \psi, \iota)}{D} \quad (4.13)$$

we expect the accuracy of distance measurements to be very roughly $\Delta D/D \approx 1/\rho$, where $\rho^2 = \sum \rho_a^2$ is the SNR (A27), giving an accuracy of $\sim 10\%$ for typical detected signals. However from Eq. (4.13) the signal amplitudes are also strongly affected by the angles θ, φ, ψ , and most importantly the inclination angle ι . Hence, there will be correlations between the measured values of D and of these angles, and the accuracy of distance measurement will be reduced relative to the above naive estimate based on Eq. (4.12).

It is straightforward in principle to calculate the effect of all the correlations by calculating the Fisher information matrix (2.7) from the waveform (4.11) for all of the variables D, \mathbf{n}, v , and ψ together with the variables $\mathcal{M}, \phi_c, t_c, \mu$, and β discussed in Secs. II and III. An analysis of this sort, but without including the post-Newtonian parameters μ and β , has been carried out by Jaranowski and Krolak [15], who numerically calculate the rms error ΔD for various different values of the angular variables. They use the three detector network consisting of the two LIGO detectors and the VIRGO detector in Pisa, Italy, with their planned orientations. Although these authors do not take into account post-Newtonian effects, it seems likely, for reasons which we discuss below in Sec. IV C and Appendix C, that their results for ΔD will not be sensitive to this restriction. Similar numerical calculations have been carried out by Marković [9], who assumed the same network of detectors. He identified a useful approximation for calculating $\Delta D/D$, based on identifying those variables with which the distance measurement is most strongly correlated, and neglecting the effect of the much smaller correlations with the other variables.

In Sec. IV C below we present an analytic calculation of $\Delta D/D$ which simplifies the treatments given in Refs. [9, 15]. Because the rms error ΔD depends on several angular variables, it is difficult to explore its behavior over the whole parameter space using numerical calculations of the type in Refs. [9, 15]. Here, by using Marković's approximation, we derive an approximate analytic expression for ΔD , which is valid for any network of detectors.

We also extend the analysis of Refs. [9, 15] in the following two respects. First, we parametrize the dependence of the result on the positions and orientations of all of the detectors in the following useful way. We show that, for a given position θ, φ on the sky, the detector network parameters influence ΔD *only* through (i) the selection of a preferred polarization basis $(\mathbf{e}^+, \mathbf{e}^\times)$ [or equivalently a preferred polarization angle $\psi(\mathbf{n})$, cf. Eq. (4.2) above] and (ii) two quantities $\sigma_D(\mathbf{n})$ and $\varepsilon_D(\mathbf{n})$, where we call $\sigma_D(\mathbf{n})$ the amplitude sensitivity and $1 - \varepsilon_D(\mathbf{n})$ the polarization sensitivity [47]. We discuss these "network sensitivity functions" in detail in Sec. IV B below. They are defined in such a way that the total signal-to-noise ratio squared (A27) of a detected signal coming from direction \mathbf{n} with polarization ψ is of the form [cf. Eq. (4.26) below]

$$\rho^2 \propto \sigma_D(\mathbf{n}) [1 + \varepsilon_D(\mathbf{n}) \cos(4\psi + \text{const}) f(v)], \quad (4.14)$$

where the function

$$f(v) \equiv \frac{(1 - v^2)^2}{1 + 6v^2 + v^4} \quad (4.15)$$

is independent of \mathbf{n} and ψ . The values of σ_D and ε_D are, as an example, $\sigma_D = 1$ and $\varepsilon_D = 0$ for the case of two detectors at the same location, rotated with respect to each other by 45° , and for vertically incident waves. In Figs. 5 and 6 below we show plots of these quantities as functions of the angles θ and φ , for the three-detector, LIGO-VIRGO network.

Second, we extend in Sec. IV D the analysis beyond the linear, Gaussian approximation outlined in Appendix A, which is normally used to estimate the rms errors. We do this by calculating the exact (within the Marković approximation), non-Gaussian probability distribution for the distance D which incorporates both our *a priori* knowledge and the information obtained from a gravitational wave measurement. This extension becomes important in two different regimes. The first regime is when $v = \cos \iota \rightarrow 1$, corresponding to binaries that we perceive to be almost face-on. In the limit $v \rightarrow 1$, the value of ΔD predicted by the linear approximation becomes infinite. As shown by Marković [9], this is because two of the signal parameters become degenerate (i.e., the derivatives $\partial \mathbf{h} / \partial \theta^i$ become linearly dependent) as $v \rightarrow 1$. Marković gave rough estimates of the effect of this breakdown of the linear formalism on the predicted value of ΔD ; the effect is not treated in the exact numeric calculations of Ref. [15]. Here, using the non-Gaussian distribution for D , we obtain an improved approximation to ΔD near the points of degeneracy. The second regime where our non-Gaussian extension of the error-estimation method is important is the limit of low signal-to-noise, and correspondingly of large relative errors in the measured binary parameters. Since the Fisher matrix method of calculating the rms errors in the measured parameters gives essentially the leading order term in an expansion in powers of $(S/N)^{-1}$, this method will be inaccurate at low values of S/N . By using an approximation which takes into account the dominant effects that are nonlinear in $(S/N)^{-1}$, we numerically estimate ΔD for different values of the parameters \mathbf{n}, v , and ψ . We show that the linear estimates for ΔD are typically off by factors $\gtrsim 2$, even for signal-to-noise ratios of more than twice the threshold value for detection, due in some cases to large non-Gaussian tails in the PDF for D . Thus, effects that are nonlinear in $(S/N)^{-1}$ are often *not* a small correction for typical detected signals.

Finally, in Sec. IV E we apply our nonlinear error estimation method to calculate the distribution of measurement accuracies for the LIGO-VIRGO network, using a Monte Carlo simulation. We estimate that $\sim 8\%$ of the distance measurements will be accurate to $\leq 15\%$, and $\sim 60\%$ to $\leq 30\%$.

Our analyses are applicable to binaries at cosmological distances, provided we interpret D as the luminosity distance to the source, and \mathcal{M} as $(1+z)$ times the true chirp mass, where z is the source's redshift [6, 9, 14]. However, a potentially important effect that we neglect is the spin-induced modulation of the signal amplitudes discussed

in Sec. III B and Ref. [43]. Hence, our results for ΔD should be regarded as rough estimates (and probably also as lower limits, since it seems most likely that including spin effects in the computation will increase ΔD). However, the tools we develop below will be useful in future, more complete analyses of distance measurement accuracies.

We use throughout this section the notations of Appendix A.

B. The network functions $\sigma_D(\mathbf{n})$ and $\varepsilon_D(\mathbf{n})$

The overall SNR (A27) and the Fisher information matrix (A30) are determined by inner products involving the signal $\mathbf{h}(t)$ and its derivatives $\partial\mathbf{h}/\partial\theta^i$ with respect to the signal parameters θ^i . We now show that a large class of these inner products depends on the network properties (i.e., the detector positions \mathbf{x}_a and polarization tensors \mathbf{d}_a) only through the two functions of sky location, $\sigma_D(\mathbf{n})$ and $\varepsilon_D(\mathbf{n})$. We start by defining the complex amplitudes

$$\mathcal{A}_B \equiv R_B^A(2\psi) \chi_A(v) e^{-i\phi_c} / D \quad (4.16)$$

which are intrinsic to the incident waves, and the detector amplitudes

$$\mathcal{A}_a = \sum_{B=+, \times} \mathcal{A}_B F_a^B(\mathbf{n}) \quad (4.17)$$

which characterize the signals seen at the various detectors. In terms of these quantities, the signal (4.11) can be written as

$$\tilde{h}_a(f) = \mathcal{A}_a e^{2\pi i \tau_a f} \tilde{k}(f), \quad (4.18)$$

where $\tilde{k}(f) \equiv D e^{i\phi_c} \tilde{h}_0(f)$ is independent of D and ϕ_c . The inner product of two signals \mathbf{h} and \mathbf{h}' written in this way, with amplitude parameters \mathcal{A}_A and \mathcal{A}'_A , is given by Eqs. (4.8), (4.18), and (A7):

$$(\mathbf{h} | \mathbf{h}') = \text{Re} [\mathcal{A}_a^* \mathcal{A}'_b \kappa^{ab}] (\tilde{k} | \tilde{k}). \quad (4.19)$$

Here the positive definite Hermitian matrix κ^{ab} is

$$\kappa^{ab} = \frac{\int_0^\infty df f^{-7/3} [\mathbf{S}_n(f)^{-1}]^{ab} e^{2\pi i f(\tau_b - \tau_a)}}{\int_0^\infty df f^{-7/3} / S_n(f)}, \quad (4.20)$$

and $S_n(f)$ in the denominator is the average of the spectral noise densities in all the detectors. If the detectors are all identical, and correlated sources of noise [represented by the off-diagonal elements of $\mathbf{S}_n(f)$] are unimportant, then κ^{ab} is just δ^{ab} .

In terms of the wave amplitudes \mathcal{A}_A , the inner product (4.19) is, from Eq. (4.17),

$$(\mathbf{h} | \mathbf{h}') = \text{Re} [\mathcal{A}_A^* \mathcal{A}'_B \Theta^{AB}] (\tilde{k} | \tilde{k}), \quad (4.21)$$

where the matrix Θ is given by

$$\Theta^{AB}(\mathbf{n}) = \sum_{a,b} F_a^A(\mathbf{n}) F_b^B(\mathbf{n}) \kappa^{ab}. \quad (4.22)$$

We see that all inner products of the type (4.19) depend on the network parameters only through the 2×2 Hermitian matrix Θ . Two key simplifications now arise.

First, correlated sources of noise will presumably be limited to pairs of detectors at the same detector site, so that the detector-network noise matrix (A3) will have a block-diagonal form with each block corresponding to a detector site. If the detectors at each site are all oriented the same way, as is likely, then the product of beam pattern functions appearing in Eq. (4.22) will be constant over each block in the indices a, b that corresponds to a nonzero subblock of the matrix $\mathbf{S}_n(f)$. Hence, from Eqs. (4.20) and (4.22), we see that the imaginary part of Θ will vanish. Second, if we change the basis \mathbf{e}^+ , \mathbf{e}^\times by a transformation of the form (4.2), which amounts to redefining the polarization angle ψ by

$$\psi \rightarrow \bar{\psi} = \psi + \Delta\psi, \quad (4.23)$$

then Θ will transform according to $\Theta \rightarrow \mathbf{R}(2\Delta\psi) \cdot \Theta \cdot \mathbf{R}(-2\Delta\psi)$. For fixed \mathbf{n} , we can by choosing $\Delta\psi$ suitably make Θ diagonal, and so be of the form

$$\Theta = \sigma_D \begin{pmatrix} 1 + \varepsilon_D & 0 \\ 0 & 1 - \varepsilon_D \end{pmatrix}, \quad (4.24)$$

where $0 \leq \varepsilon_D \leq 1$. This defines the network functions $\sigma_D(\mathbf{n})$ and $\varepsilon_D(\mathbf{n})$. The required value of $\Delta\psi = \Delta\psi(\mathbf{n})$ is given by

$$\tan(4\Delta\psi) = \frac{2\Theta_{++}}{\Theta_{++} + \Theta_{\times\times}}. \quad (4.25)$$

The combined SNR (A27) can be determined in terms of these network functions by combining Eqs. (4.16), (4.21), and (4.24) to give

$$\rho^2 = \rho_0^2 \sigma_D(\mathbf{n}) [c_0(v) + \varepsilon_D(\mathbf{n}) c_1(v) \cos(4\bar{\psi})], \quad (4.26)$$

where $c_0(v) = (1+v^2)^2/4+v^2$, $c_1(v) = (1+v^2)^2/4-v^2 = (1-v^2)^2/4$, and $\bar{\psi}$ is given by Eqs. (4.23) and (4.25). The quantity

$$\rho_0^2 \equiv D^{-2}(\tilde{k} | \tilde{k}) = (\tilde{h}_0 | \tilde{h}_0) = 4 \int_0^\infty \frac{|\tilde{h}_0(f)|^2}{S_n(f)} df \quad (4.27)$$

appearing in Eq. (4.26) is the SNR that would apply to one detector if a face-on ($v = 1$) binary were directly overhead. From Eqs. (4.8) and (4.27), we find $\rho_0 = r_0/D$, where for the noise spectrum (2.1) the distance r_0 is

$$r_0 = 6.5 \text{ Gpc} \left(\frac{\mathcal{M}}{M_\odot} \right)^{5/6} \left(\frac{f_0}{70 \text{ Hz}} \right)^{-2/3} \times \left(\frac{S_0}{3 \times 10^{-48} \text{ sec}} \right)^{-1/2}. \quad (4.28)$$

The fiducial values of the detector parameters S_0 and f_0 used here are those appropriate for the advanced LIGO detectors [3], cf. Sec. II above. Note that the dependence of the SNR (4.26) on the polarization angle ψ vanishes when the binary is perceived to be face-on ($v = 1$), as we would expect physically due to rotational invariance about the line of sight. In the opposite limit of edge-on binaries ($v \rightarrow 0$), the incident waves are highly linearly polarized, and the SNR typically depends strongly on ψ , varying by factors of ~ 10 or more as ψ is varied [see Fig. 6

below].

We now derive simple formulae for the functions σ_D and ε_D . From Eq. (4.24), it is clear that σ_D is just half of the trace of the matrix Θ , which is invariant under rotations. Using Eqs. (4.3) and (4.22) gives

$$2\sigma_D = \left\{ \sum_A (\mathbf{e}_n^A)_{ij} (\mathbf{e}_n^A)_{kl} \right\} \left\{ \sum_{a,b} \kappa^{ab} (\mathbf{d}_a)_{ij} (\mathbf{d}_a)_{kl} \right\}. \quad (4.29)$$

If we denote the first term in curly brackets by S_{ijkl} , then it is straightforward to show that

$$\begin{aligned} S_{ijkl} = & -\delta_{ij}\delta_{kl} + (\delta_{ik}\delta_{jl} + \delta_{il}\delta_{jk}) + (\delta_{ij}n_k n_l + \delta_{kl}n_i n_j) \\ & -(\delta_{ik}n_j n_l + \delta_{il}n_j n_k + \delta_{jk}n_i n_l + \delta_{jl}n_i n_k) \\ & + n_i n_j n_k n_l. \end{aligned} \quad (4.30)$$

This yields for the amplitude sensitivity function the formula

$$\begin{aligned} \sigma_D(\mathbf{n}) = & \frac{1}{2} \kappa^{ab} [2 \mathbf{d}_a : \mathbf{d}_b - 4 \mathbf{n} \cdot (\mathbf{d}_a \cdot \mathbf{d}_b) \cdot \mathbf{n} \\ & + (\mathbf{n} \cdot \mathbf{d}_a \cdot \mathbf{n})(\mathbf{n} \cdot \mathbf{d}_b \cdot \mathbf{n})], \end{aligned} \quad (4.31)$$

where we have used the property $\text{Tr } \mathbf{d}_a = 0$.

It is similarly straightforward to evaluate the polarization sensitivity $1 - \varepsilon_D(\mathbf{n})$. We introduce the notation

$$\langle \mathbf{d}_a | \mathbf{d}_b \rangle_n \equiv (\mathbf{d}_a)_{ij} S_{ijkl} (\mathbf{d}_b)_{kl} \quad (4.32)$$

$$= 2 \mathbf{d}_a^\perp : \mathbf{d}_b^\perp - (\text{Tr } \mathbf{d}_a^\perp)(\text{Tr } \mathbf{d}_b^\perp), \quad (4.33)$$

where \mathbf{d}_a^\perp denotes the projection $(\delta_{ik} - n_i n_k)(\delta_{jl} - n_j n_l)(\mathbf{d}_a)_{kl}$ of \mathbf{d}_a perpendicular to \mathbf{n} . Then, using the relation from Eq. (4.24) that $\text{Tr } \Theta^2 = 2\sigma_D^2(1 + \varepsilon_D^2)$, and Eqs. (4.3) and (4.22), gives

$$\varepsilon_D(\mathbf{n})^2 = \frac{1}{2\sigma_D(\mathbf{n})^2} \sum_{abcd} \langle \mathbf{d}_a | \mathbf{d}_b \rangle_n \langle \mathbf{d}_c | \mathbf{d}_d \rangle_n \kappa^{ac} \kappa^{bd} - 1. \quad (4.34)$$

We now evaluate σ_D and ε_D for the LIGO-VIRGO detector network. Let $\mathbf{e}_\hat{\theta} = \mathbf{n}$, $\mathbf{e}_\hat{\phi}$ and \mathbf{e}_ϕ be the usual basis of orthonormal vectors. Then for a detector at position θ, φ on the Earth's surface, such that the angle measured anticlockwise from the local eastward directed meridian to the bisector of the detector arms is α , the polarization tensor is

$$\begin{aligned} \mathbf{d} = & -\sin(2\alpha)(\mathbf{e}_\theta \otimes \mathbf{e}_\theta - \mathbf{e}_\phi \otimes \mathbf{e}_\phi)/2 \\ & + \cos(2\alpha)(\mathbf{e}_\theta \otimes \mathbf{e}_\phi + \mathbf{e}_\phi \otimes \mathbf{e}_\theta)/2. \end{aligned} \quad (4.35)$$

The values of $(\theta, \varphi, \alpha)$ for the various detectors are $(59.4^\circ, -90.8^\circ, 243^\circ)$ for the LIGO detector in Hanford, Washington, $(43.5^\circ, -119.4^\circ, 171^\circ)$ for the LIGO detec-

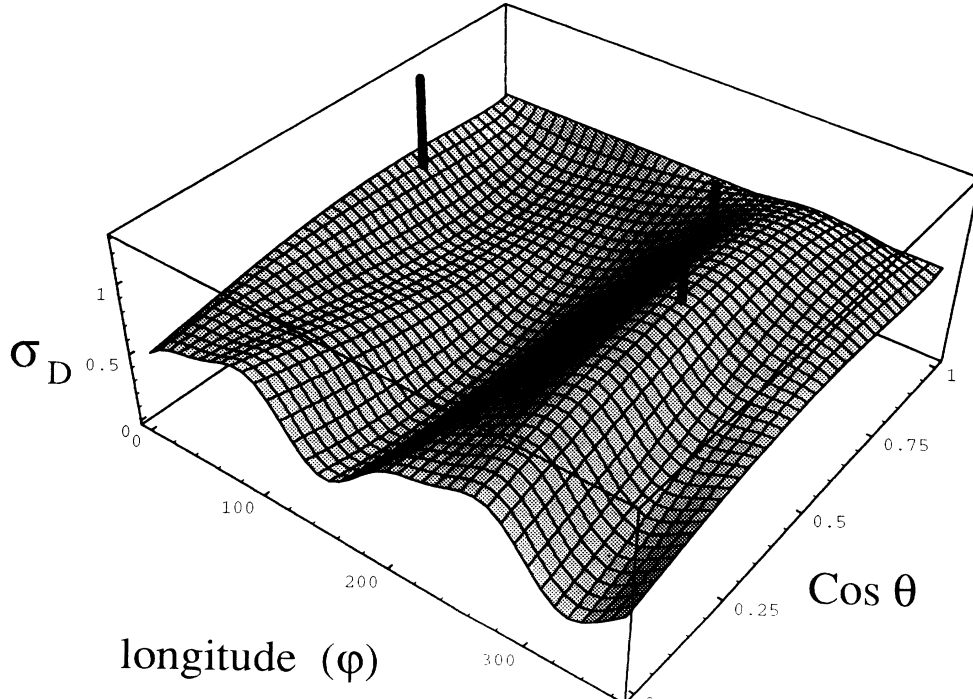


FIG. 5. The amplitude sensitivity function $\sigma_D(\mathbf{n})$, as a function of position on the sky parametrized by the Earth-fixed coordinates θ and φ , for the detector network consisting of the two LIGO detectors in Hanford, Washington and Livingston, Louisiana, and the VIRGO detector in Pisa, Italy. The axis $\theta = 0$ is the Earth's axis of rotation, and $\varphi = 0^\circ$ longitude. Only sky positions over the northern hemisphere are shown, because σ_D takes the same values at antipodal points. The function $\sigma_D(\mathbf{n})$ has the following meaning: for a source of waves in the direction \mathbf{n} , the combined signal-to-noise ratio of the whole network, averaged over all polarization angles ψ of the source (equivalently, averaged over rotations of the source in the plane perpendicular to the line of sight), will be proportional to $\sigma_D(\mathbf{n})$. The thick black lines indicate the positions of the three detectors. This plot can be generated by combining Eqs. (4.31) and (4.35) of the text with the network parameters given after Eq. (4.35).

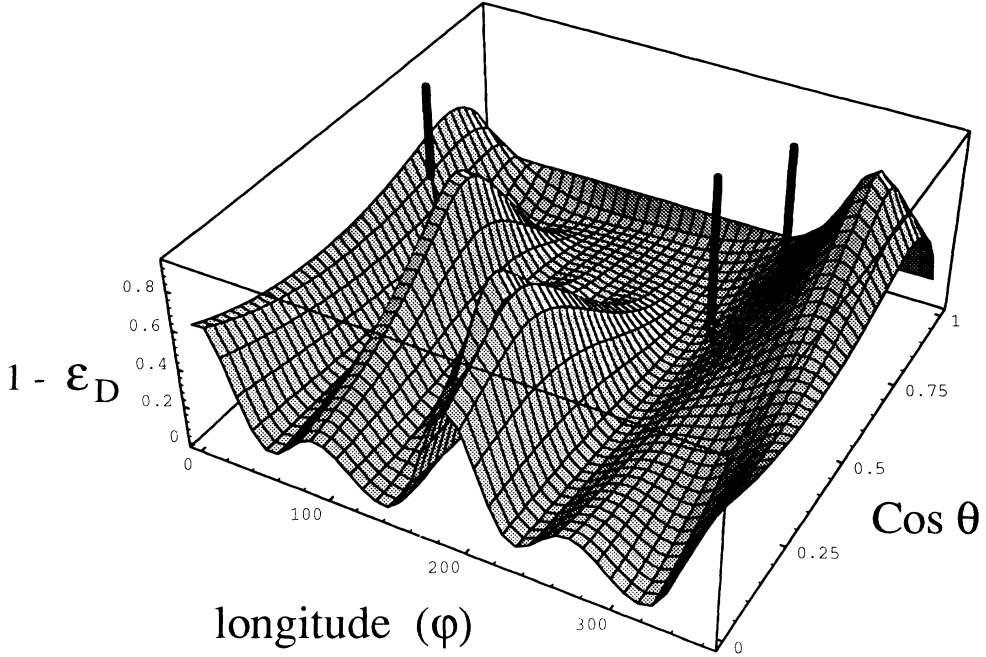


FIG. 6. The polarization sensitivity function $1 - \varepsilon_D(\mathbf{n})$, for the LIGO-VIRGO detector network; see caption of Fig. 5. This plot can be generated by combining Eqs. (4.30), (4.32), (4.34), and (4.35) of the text. The quantity $\varepsilon_D(\mathbf{n})$ essentially measures the “skewness” or asymmetry in the sensitivities of the network to the two independent polarization components of waves propagating in the direction \mathbf{n} . When $\varepsilon_D \approx 0$, the network has roughly equal sensitivity to both polarization components. When $\varepsilon_D \approx 1$, on the other hand, one polarization component can be measured far more accurately than its orthogonal counterpart. In this case the signal-to-noise ratio for incident, strongly linearly polarized bursts of waves (e.g., those from edge-on coalescing binaries) will depend sensitively on the polarization axis, i.e., it would vary by large factors if the source were rotated in the plane perpendicular to the line of sight. Note that the polarization sensitivity is poor ($\lesssim 0.2$) for directions directly overhead the two LIGO detectors (because the two detectors are nearly parallel), and is typically $\lesssim 0.3$ over most of the sky. Good sensitivity is achieved in isolated regions.

tor in Livingston, Louisiana, and $(46.4^\circ, 10.25^\circ, 117^\circ)$ for the VIRGO detector in Pisa, Italy [15]. We assume that the detectors at all three sites are identical and that noise sources are uncorrelated, so that from Eq. (4.20), $\kappa^{ab} = \delta^{ab}$. The resulting plots of σ_D and $1 - \varepsilon_D$ are shown in Figs. 5 and 6.

C. The Marković approximation

We now explain the approximation method used by Marković [9], which we modify slightly below. We start by considering the accuracy $\Delta\mathbf{n}$ with which a given source can be located on the sky. The location \mathbf{n} will be largely determined by “time of flight” measurements between the various detectors, i.e., measurements of the quantities $\tau_a - \tau_b = -\mathbf{n} \cdot (\mathbf{x}_a - \mathbf{x}_b)$ in Eq. (4.11) [6, 15]. Hence, the variables \mathbf{n} and τ_a will be strongly correlated, and $\Delta\mathbf{n}$ will be largely determined by the ratio of the timing accuracies $\Delta(\tau_a - \tau_b)$ to the light travel times between the various detectors. Schutz [6] has estimated the resulting angular resolution to be ~ 1 square degree for typical detected signals, which is roughly in agreement with the recent detailed coalescing binary calculations of Jaranowski and Krolak [15]. It is also in rough agreement with numerical simulations of Gürsel and Tinto [7], which were carried out in the context of arbitrary bursts

of gravitational waves. Hence, we see from Eq. (4.11) that typical variations in \mathbf{n} will give rise to variations in the measured value of D that are small compared to ΔD . Thus, the correlations between D and \mathbf{n} should be small, and to a good approximation we can treat \mathbf{n} as known when calculating ΔD [9].

In the approximation that \mathbf{n} is constant, we can divide the remaining parameters into two groups. The first consists of the four “amplitude” parameters D, v, ψ , and ϕ_c , which determine the two complex amplitudes \mathcal{A}_+ and \mathcal{A}_\times via Eq. (4.16). The second group of parameters consists of \mathcal{M}, t_c, μ , together with some spin parameters, which enter only in the phase $\Psi(f)$ of the Fourier transform of the signal, and control the evolution in time of the phase of the waveform [48]. In Appendix C we show that the second group of parameters decouples from the first to linear order in $1/\rho$, and in the constant \mathbf{n} approximation. More precisely: if one calculates the Fisher matrix (A30) for all of the variables except \mathbf{n} , inverts it to obtain the covariance matrix Σ^{ij} , and takes the 4×4 subblock of Σ^{ij} corresponding to the amplitude group of parameters, then the result is the same as if one computes the Fisher matrix for just the four amplitude parameters alone, and then inverts that. Heuristically what this means is that the effect of the correlations between (D, v, ψ) and all of the parameters ϕ_c, t_c, \mathcal{M} , etc., can be computed by

considering the correlations with just one phase variable, namely, ϕ_c , the orbital phase at coalescence [48].

We now calculate the Fisher information matrix (A30) for the four amplitude parameters D , v , ψ , and ϕ_c , and for an arbitrary detector network, as this should yield a good approximation to ΔD . The approximation that was used in Ref. [9] was in fact to consider only D , v , and ψ ; below we find [cf. Eqs. (4.37) and (4.39)] that the fractional corrections due to also including ϕ_c are of order $\varepsilon_D(\mathbf{n}) \sin(4\bar{\psi})$, where $\bar{\psi}$ is given by Eqs. (4.23) and (4.25). Since $0 \leq \varepsilon_D \leq 1$ always, the fractional corrections are always $\lesssim 1$ [49].

From Eq. (A30), it is clear that the Fisher matrices calculated using two different sets of variables are simply related by transforming with the Jacobian matrix of the variable transformation. Hence, we can use any convenient set of variables to evaluate Γ_{ij} and Σ^{ij} , and afterward transform to the physical variables of interest. We define the variables α and β by

$$\begin{pmatrix} \alpha \\ \beta \end{pmatrix} = \frac{1}{D} \begin{pmatrix} v \\ (1+v^2)/2 \end{pmatrix}. \quad (4.36)$$

The waveform (4.11) depends linearly on these variables, which simplifies the computation.

Using Eqs. (4.16) – (4.18), (4.21), (4.24), (4.27), (A30), and the relation $\rho_0 = r_0/D$, we obtain

$$\Gamma_{ij} = r_0^2 \sigma_D(\mathbf{n}) [F_{ij} + \varepsilon_D(\mathbf{n}) G_{ij}], \quad (4.37)$$

where the variables are $\theta^i = (\psi, \alpha, \beta, \phi_c)$. Defining $c_0 = \alpha^2 + \beta^2$, $c_1 = \beta^2 - \alpha^2$, $c_4 = \cos(4\bar{\psi})$, and $s_4 = \sin(4\bar{\psi})$, the matrices \mathbf{F} and \mathbf{G} are given by

$$\mathbf{F} = \begin{bmatrix} 4c_0 & 0 & 0 & -4\alpha\beta \\ 0 & 1 & 0 & 0 \\ 0 & 0 & 1 & 0 \\ -4\alpha\beta & 0 & 0 & c_0 \end{bmatrix} \quad (4.38)$$

and

$$\mathbf{G} = \begin{bmatrix} -4c_1c_4 & 2\alpha s_4 & -2\beta s_4 & 0 \\ 2\alpha s_4 & -c_4 & 0 & -\beta s_4 \\ -2\beta s_4 & 0 & c_4 & \alpha s_4 \\ 0 & -\beta s_4 & \alpha s_4 & c_1 c_4 \end{bmatrix}. \quad (4.39)$$

Inverting the matrix (4.37) and taking the 2×2 subblock corresponding to the variables α, β , we find with the help of MATHEMATICA that

$$\Sigma^{ij} = \frac{1}{r_0^2 \sigma_D(1-\varepsilon_D^2)} \begin{bmatrix} 1 + \varepsilon_D c_4 & 0 \\ 0 & 1 - \varepsilon_D c_4 \end{bmatrix}. \quad (4.40)$$

Finally, transforming this with the Jacobian of the transformation (4.36) and taking the (D, D) element of the resulting matrix yields

$$\Delta D^2 = \frac{8D^4}{n_d r_0^2} \Upsilon(\mathbf{n}, v, \psi)^2, \quad (4.41)$$

where

$$\Upsilon(\mathbf{n}, v, \psi)^2 = \frac{n_d [(1+v^2) - \varepsilon_D \cos(4\bar{\psi}) (1-v^2)]}{2\sigma_D (1-\varepsilon_D^2) (1-v^2)^2}, \quad (4.42)$$

and n_d is the number of detectors. The dimensionless function Υ satisfies

$$\Upsilon(\mathbf{n}, v, \psi) \geq 1, \quad (4.43)$$

since from Eqs. (4.31), (4.33), and (4.24) it follows that $\sigma_D \leq n_d/2$ and $0 \leq \varepsilon_D \leq 1$ always, for any detector network.

Equation (4.41) is the main result of this subsection. We now discuss its properties and range of applicability. It clearly breaks down and overestimates ΔD when $v \rightarrow 1$. As shown by Marković, this is because $\partial \mathbf{h} / \partial D \propto \partial \mathbf{h} / \partial v$ at $v = 1$, so that the linear error-estimation method breaks down. However, it will *underestimate* the true measurement error for sufficiently small values of the SNR ρ , because of the inadequacy of the linear error-estimation formalism in this regime (cf. Appendix A). In Sec. IV D below we numerically calculate more accurate values of $\Delta D/D$, and show that even for small values of v , and even for relatively large values of ρ (e.g., $\rho \gtrsim 20$, more than twice the threshold), the results predicted by the formula (4.41) can be off by factors $\gtrsim 2$.

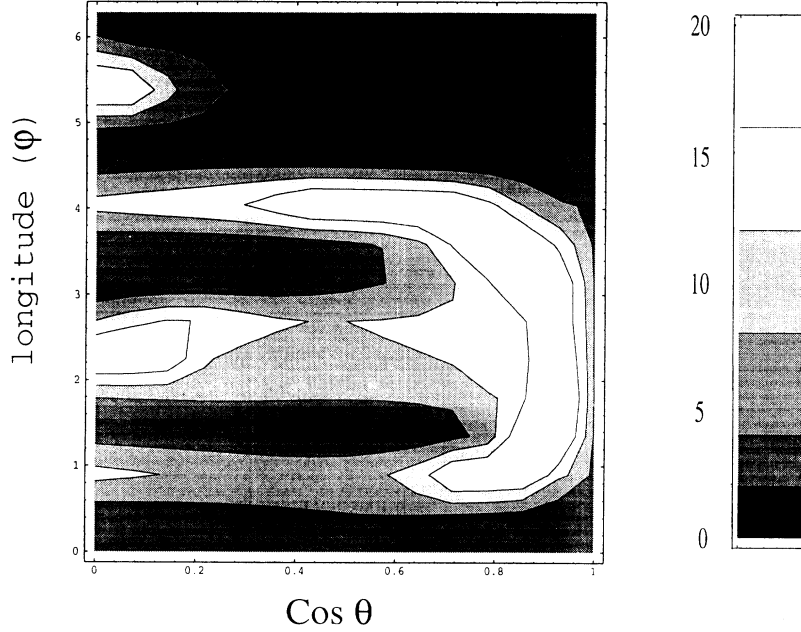
Hence, the formula (4.41) is of only limited applicability. Its main virtue is that it allows one to understand qualitatively how the distance measurement accuracy is influenced by the parameters σ_D , ε_D , ψ , and (to a more limited extent) v ; and thereby by using Figs. 5 and 6 how it varies with sky location \mathbf{n} . We now discuss the dependence of $\Delta D/D$ on these parameters.

As the polarization angle ψ is varied, it can be seen that

$$\Upsilon_{\min}(\mathbf{n}, v) \leq \Upsilon(\mathbf{n}, v, \psi) \leq \Upsilon_{\max}(\mathbf{n}, v), \quad (4.44)$$

where Υ_{\min} and Υ_{\max} are given by substituting $\cos(4\bar{\psi}) = \pm 1$ in Eq. (4.42). As an illustration, Figs. 7 and 8 show Υ_{\min} and Υ_{\max} as functions of \mathbf{n} at $v = 1/\sqrt{2}$. It can be seen that the distance measurement accuracy can vary over the sky by factors of order ~ 20 , for binaries at a fixed distance and with fixed inclination angle. The reason for this strong variation of more than an order of magnitude is easy to understand. A key feature of the result (4.42) is the factor of $1/(1-\varepsilon_D^2)$, which diverges in the limit $\varepsilon_D \rightarrow 1$. This divergence is *not* an artifact of our approximate, linear error-estimation method (unlike the divergence in Υ at $v \rightarrow 1$). The physical reason for the divergence as $\varepsilon_D \rightarrow 1$ is that for directions \mathbf{n} such that $1 - \varepsilon_D(\mathbf{n}) \ll 1$, the detector network has very poor ability to disentangle the two polarization components of the incident waves, both of which are needed in order to determine D . As shown in Fig. 6, there are large regions on the sky in which the polarization sensitivity $1 - \varepsilon_D$ of the LIGO-VIRGO network is poor, which correspond to the regions of high $\Delta D/D$ in Figs. 7 and 8 [50].

Part of the reason for the low values of $1 - \varepsilon_D$ for the LIGO-VIRGO network is that the two LIGO detectors are nearly parallel, so that they access essentially a single polarization component of the gravitational wave field. (They were chosen in this way in order to enhance the reliability of detection of burst sources.) The addition of a fourth detector would greatly improve the polarization sensitivity of the network. In Fig. 9 we plot that



fraction $\Omega(\varepsilon_D)/4\pi$ of the sky in which the polarization sensitivity is $\leq 1 - \varepsilon_D$, for the LIGO-VIRGO network. We also as an illustration plot the same quantity for a hypothetical four-detector network consisting of the LIGO and VIRGO detectors together with a detector in Perth, Australia, whose parameters [cf. Eq. (4.35) above] are assumed to be $(\theta, \varphi, \alpha) = (121^\circ, 116^\circ, 90^\circ)$.

The quantity $\Upsilon(\mathbf{n}, v, \psi)$ shown in Figs. 7 and 8 gives distance-measurement accuracy as a function of *Earth-fixed* coordinates (θ, φ) . The distance-measurement accuracy for coalescing binaries at a given right ascension and declination, averaged over many sources with different arrival times, will clearly be given by the average over

FIG. 7. The dependence of the distance measurement accuracy $\Delta D/D$ on the sky location \mathbf{n} , the polarization angle ψ , and the cosine v of the angle of inclination of the orbit to the line of sight is approximately given by $\Delta D/D \propto \Upsilon(\mathbf{n}, v, \psi)$, where the dimensionless function Υ is defined in Eq. (4.42). Here we plot for the LIGO-VIRGO detector network the quantity Υ_{\max} obtained by maximizing Υ over all polarization angles ψ , at $v^2 = 1/2$, as a function of θ and φ . Higher values of Υ indicated by regions of lighter shading correspond to poorer measurement accuracy.

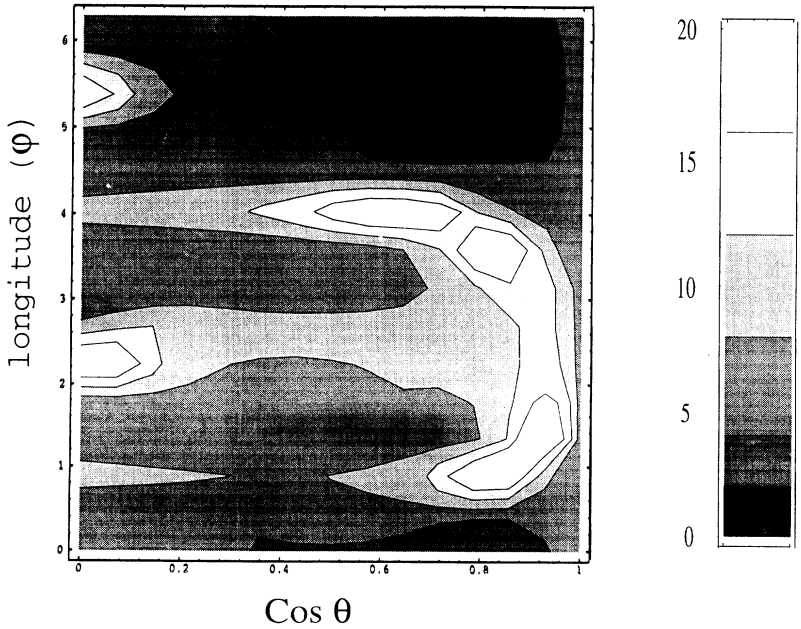


FIG. 8. The quantity Υ_{\min} which is obtained by minimizing $\Upsilon(\mathbf{n}, v, \psi)$ over ψ , at $v^2 = 1/2$; see caption of Fig. 7.

φ of Υ (due to the Earth's rotation). Values of this averaged accuracy in the band $0.15 \lesssim |\cos \theta| \lesssim 0.65$ are typically a factor of ~ 2 better than those outside this band, over the poles and near the celestial equator. Similarly, the average over φ of $1/\sigma_D(\theta, \varphi)$ is roughly proportional to the average maximum distance to which sources can be seen at a given declination; it does not vary by more than $\sim 20\%$. Note that the distribution of sources on the sky is expected to be approximately isotropic because the large distance ($\gtrsim 200$ Mpc) to typical coalescences.

Lower bounds for $\Delta D/D$ can be obtained by combining Eqs. (4.27), (4.41), and (4.42) and minimizing over \mathbf{n} , v , and ψ . If we define

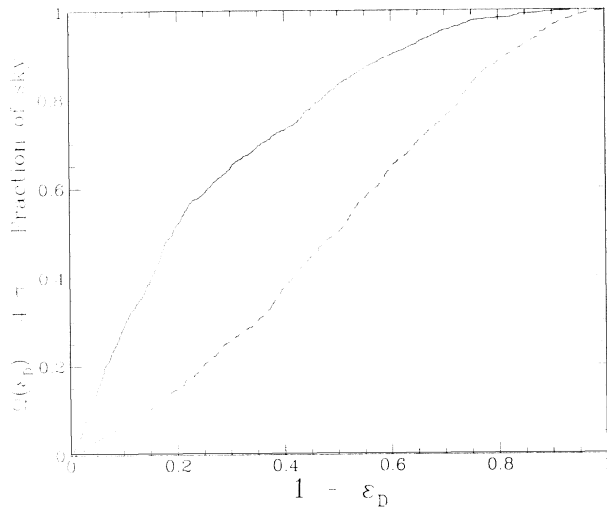


FIG. 9. The quantity $\Omega(\varepsilon_D)$, which is the solid angle on the sky for which the polarization sensitivity is less than $1 - \varepsilon_D$, for two different detector networks. The solid line indicates the LIGO-VIRGO detector network, and the dashed line a four-detector network consisting of the LIGO and VIRGO detectors together with a hypothetical detector in Perth, Australia. These plots were generated using 1000 randomly chosen directions \mathbf{n} . The great improvement in polarization sensitivity due to the additional detector is apparent: e.g., the polarization sensitivity is ≤ 0.25 over $\sim 60\%$ of the sky for the three-detector network, but only over $\sim 20\%$ of the sky for the four-detector network.

$$\sigma_{\max} = \max_{\mathbf{n}} \sigma_D(\mathbf{n}) \quad (4.45)$$

$$= 1.04 \quad (\text{for LIGO-VIRGO}), \quad (4.46)$$

we obtain the following lower bounds on $\Delta D/D$:

$$\frac{\Delta D}{D} \geq \frac{2}{\sqrt{\sigma_{\max}}} \frac{D}{r_0}, \quad (4.47)$$

$$\frac{\Delta D}{D} \geq \frac{1}{\rho}, \quad (4.48)$$

together with the upper bound for the overall SNR ρ ,

$$\rho \leq \sqrt{2\sigma_{\max}} \frac{r_0}{D}. \quad (4.49)$$

These bounds remain roughly valid when effects that are nonlinear in r_0/D are approximately taken into account (cf. Figs. 13–17 below).

D. Extension of analysis to beyond the Gaussian approximation

As explained in Appendix A, the Fisher matrix approach to calculating the probability distribution function (PDF) for the measured parameters is an approximation whose validity depends in part on the particular set of variables one uses to evaluate the Fisher matrix. In particular, the approximation works best for parameters on which the signal $\mathbf{h}(t)$ depends *linearly*. The key idea for dealing with the degeneracy limit $v \rightarrow 1$ is to calculate the Gaussian probability distribution for the amplitudes

\mathcal{A}_A , which is exact because the signal depends linearly on these amplitudes (see subsection A 6 of Appendix A below). Substituting Eq. (4.16) into this PDF then yields the exact, non-Gaussian distribution for the parameters D , v , ψ , and ϕ_c , where we mean “exact” in the context of the Marković approximation $\Delta\mathbf{n} = 0$. From this non-Gaussian distribution, values of ΔD can be determined which are more accurate than those given by Eq. (4.41) in the regime $v \rightarrow 1$ and for low signal-to-noise ratios.

In this subsection we calculate so-called Bayesian errors instead of frequentist errors. The distinction is carefully explained in Appendix A 2. The distinction is important only beyond leading order in $1/\rho$, and hence unimportant elsewhere in this paper. In practical terms, the use of Bayesian errors means that the rms errors will be expressed as functions of the measured, best-fit values for the source parameters, instead of their true values.

By using Eqs. (4.19) and (4.27) one finds that the exponential factor in Eq. (A10), given a gravitational wave measurement, is proportional to

$$\exp \left[-\frac{r_0^2}{2} (\mathcal{A}_a - \hat{\mathcal{A}}_a)^* (\mathcal{A}_b - \hat{\mathcal{A}}_b) \kappa^{ab} \right]. \quad (4.50)$$

Here the quantities $\hat{\mathcal{A}}_a$ are the amplitudes that we measure at each detector (by using matched filtering). The corresponding PDF for the intrinsic amplitudes \mathcal{A}_A is, from Eqs. (4.17) and (A10),

$$\begin{aligned} p(\mathcal{A}_A) &= \mathcal{N} p^{(0)}(\mathcal{A}_A) \\ &\times \exp \left[-\frac{r_0^2}{2} (\mathcal{A}_A - \hat{\mathcal{A}}_A)^* (\mathcal{A}_B - \hat{\mathcal{A}}_B) \Theta^{AB} \right], \end{aligned} \quad (4.51)$$

where

$$\hat{\mathcal{A}}_A \equiv (\Theta^{-1})_{AB} F_a^B \hat{\mathcal{A}}_b \kappa^{ab}. \quad (4.52)$$

Here $p^{(0)}(\mathcal{A}_A)$ is our *a priori* PDF for the amplitude parameters, and \mathcal{N} is a normalization constant.

As an aside, Eq. (4.52) provides us with the maximum-likelihood estimator \hat{D} (in the constant \mathbf{n} approximation) of the distance to the binary in terms of the measured amplitudes $\hat{\mathcal{A}}_a$. This is because Eq. (4.16), reexpressed in terms of caret quantities, may be inverted to determine \hat{D} in terms of the $\hat{\mathcal{A}}_A$'s:

$$\hat{D} = \frac{\hat{\beta} - \sqrt{\hat{\beta}^2 - \hat{\alpha}^2}}{\hat{\alpha}^2}, \quad (4.53)$$

where [cf. Eq. (4.36) above]

$$\hat{\alpha}^2 = \frac{1}{2} \left[|\hat{\mathcal{A}}_+|^2 + |\hat{\mathcal{A}}_\times|^2 - |\hat{\mathcal{A}}_+^2 + \hat{\mathcal{A}}_\times^2| \right] \quad (4.54)$$

and

$$\hat{\beta}^2 = \frac{1}{2} \left[|\hat{\mathcal{A}}_+|^2 + |\hat{\mathcal{A}}_\times|^2 + |\hat{\mathcal{A}}_+^2 + \hat{\mathcal{A}}_\times^2| \right]. \quad (4.55)$$

The PDF $p^{(0)}(\mathcal{A}_A)$ in Eq. (4.51) represents our *a priori* information about the distribution of the parameters \mathcal{A}_A [or equivalently from Eq. (4.16) of the parameters (D, v, ψ, ϕ_c)], given that a signal has been detected. Since we expect sources to be uniformly dis-

tributed in orientation and in space (on the relevant scales of $\gtrsim 100$ Mpc), we take

$$\begin{aligned} dp^{(0)} \propto & d\psi d\phi_c \Theta(1 - v^2) dv \\ & \times \Theta(D) \Theta(D_{\max} - D) D^2 dD. \end{aligned} \quad (4.56)$$

Here Θ is the step function, and the cutoff for distances greater than D_{\max} is a (somewhat crude) representation of our knowledge that very distant sources would not have been detected. A suitable choice for D_{\max} is the distance r_0 , cf. Eqs. (4.26) and (4.28) above. Our results below are insensitive to the exact location of this cutoff, but it must be included to make the PDF (4.51) formally normalizable. Now let D_0 , v_0 , ψ_0 , and ϕ_{c0} be the parameters obtained from the amplitudes \hat{A}_A by inverting Eq. (4.16), so that, in particular, $D_0 = \hat{D}$. Substituting Eqs. (4.16) and (4.56) into (4.51) yields a non-Gaussian PDF for the variables (D, v, ψ, ϕ_c) which depends on the parameters $(D_0, v_0, \psi_0, \phi_{c0})$. From this PDF it is straightforward in principle to calculate ΔD , by first integrating over v , ψ , and ϕ_c to determine the reduced PDF $p(D)$ for D alone. If one first expands the argument of the exponential to second order in the quantities $D - D_0$, $v - v_0$, $\psi - \psi_0$, and $\phi_c - \phi_{c0}$, the result obtained is just Eq. (4.41) above, which is accurate to linear order in $1/\rho$.

Thus, in order to go beyond this linear approximation, one has to integrate the PDF (4.51) over v , ψ , and ϕ_c . Because this is difficult to do exactly, we now make an approximation which treats the correlations between D and (ψ, ϕ_c) to linear order in $1/\rho$, but treats more precisely the strong correlations between D and v . This approximation should give rough estimates of effects that are nonlinear in $1/\rho$, and moreover removes the singularity in our previous result (4.41) at $v = 1$. The approximation consists of expanding the argument of the exponential in Eq. (4.51) to second order in $\psi - \psi_0$ and $\phi_c - \phi_{c0}$, and integrating over ψ and ϕ_c . One then obtains a function of v , D , v_0 , D_0 , and ψ_0 ; the dependence on ϕ_{c0} drops out. This function is of the form (prefactor) \times (exponential factor). The prefactor depends only weakly on D and v in comparison to the exponential factor, so we can approximate it to be constant [52]. We then obtain the following PDF, which may also be obtained by substituting the transformation (4.36) into the Gaussian PDF for the variables α, β that corresponds to the variance-covariance matrix (4.40).

The result is, in terms of the rescaled distance $\mathcal{D} = D/D_0$,

$$\begin{aligned} dp(v, \mathcal{D}) = & \mathcal{N} \mathcal{D}^2 \exp \left\{ -\frac{1}{2\Delta_1^2} \left(\frac{v}{\mathcal{D}} - v_0 \right)^2 \right. \\ & \left. - \frac{1}{2\Delta_2^2} \left[\frac{1+v^2}{2\mathcal{D}} - \frac{1+v_0^2}{2} \right]^2 \right\} \\ & \times \Theta(\mathcal{D}) \Theta(D_{\max}/D_0 - \mathcal{D}) \Theta(1 - v^2) dv d\mathcal{D}. \end{aligned} \quad (4.57)$$

Here Θ is the step function, \mathcal{N} is a normalization constant,

$$\Delta_1 = \frac{D_0}{r_0} \sqrt{\frac{1 + \epsilon_D \cos(4\bar{\psi}_0)}{\sigma_D(1 - \epsilon_D^2)}}, \quad (4.58a)$$

$$\Delta_2 = \frac{D_0}{r_0} \sqrt{\frac{1 - \epsilon_D \cos(4\bar{\psi}_0)}{\sigma_D(1 - \epsilon_D^2)}}, \quad (4.58b)$$

and $\bar{\psi}_0 = \psi_0 + \Delta\psi(\mathbf{n})$ [cf. Eq. (4.25) above]. In terms of these quantities, the previous, approximate result (4.41) is

$$\frac{\Delta D}{D_0} = \frac{2\sqrt{v_0^2\Delta_1^2 + \Delta_2^2}}{1 - v_0^2}. \quad (4.59)$$

From the PDF (4.57) one can numerically calculate the reduced PDF for \mathcal{D} alone,

$$p(\mathcal{D}) = \int_{-1}^1 dv p(v, \mathcal{D}), \quad (4.60)$$

and thereby determine ΔD . As an example we show in Fig. 10 a plot of $p(D)$ for a particular choice of the parameters D_0 , v_0 , ψ_0 , and for a particular direction on the sky. The non-Gaussian fall off in this figure at large values of D is a general feature, although its magnitude in this example is larger than is typical. It can be seen

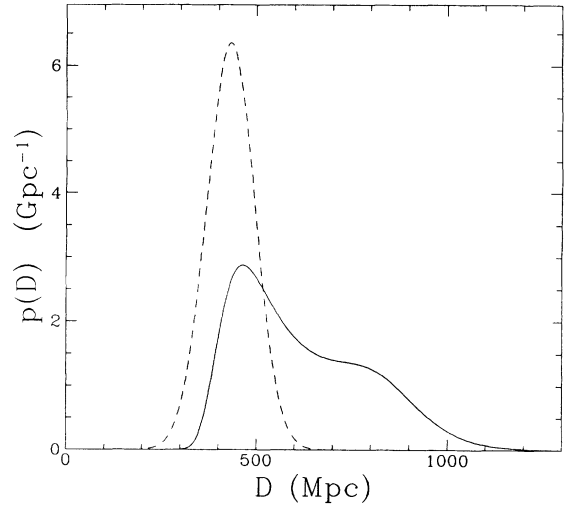


FIG. 10. An example illustrating the necessity of going beyond the Gaussian approximation. Consider a neutron-star–neutron-star binary merger in the direction given by $(\theta, \varphi) = (50^\circ, 276^\circ)$. The LIGO-VIRGO network parameters for this direction are $\sigma_D = 1.03$ and $\epsilon_D = 0.74$. Suppose that an experimenter determines from the measured signal the following “best-fit” (maximum-likelihood) parameters: distance $D_0 = 432$ Mpc [corresponding to a signal-to-noise ratio of $\rho = 12.8$, assuming the advanced detector sensitivity level (2.1)], masses $M_1 = M_2 = 1.4M_\odot$, cosine of inclination angle $v_0 = 0.31$, and polarization angle $\bar{\psi}_0 = 56.5^\circ$. Then the distribution that she would infer by a Bayesian analysis for the distance to the source is shown by the solid curve; it is given by Eqs. (4.57), (4.60), and (4.28) of the text. The Gaussian approximation [Eq. (4.41) of the text] to this distribution is shown by the dashed curve. The distance measurement accuracy is atypically poor in this example; see Fig. 16 below.

that the distance measurement accuracy is a factor of ~ 2 worse than that predicted by Eq. (4.41).

Now from Fig. 10 it can be seen that the value of D which maximizes $p(D)$ is *not* the same as D_0 , i.e., the D component of the point (v_0, D_0) which maximizes $p(v, D)$. Hence, the “maximum-likelihood” method for estimating signal parameters is ambiguous — the results obtained for one variable depend on whether or not other variables are integrated out before the maximum is taken. As explained in Appendix A, we advocate as the “best-fit” value of D the expected value

$$\langle D \rangle = \int D p(D) dD = \int D p(v, D) dv dD, \quad (4.61)$$

instead of the maximum-likelihood estimate D_0 . (Maximum-likelihood estimation will need to be used, however, to obtain initial estimates of the signal parameters.) Correspondingly, to estimate distance measurement errors we use the quantity

$$\frac{\Delta D}{D} \equiv \frac{\sqrt{\langle D^2 \rangle - \langle D \rangle^2}}{\langle D \rangle}. \quad (4.62)$$

This can be calculated numerically from Eqs. (4.57) and (4.60), and in general will depend in a complicated way on the parameters Δ_1 , Δ_2 , and v_0 , and very weakly on the rescaled cutoff D_{\max}/D_0 . For the binary merger example of Fig. 10, we show in Fig. 11 how the accuracy (4.62) varies with v_0 , and in Fig. 12 how it varies (through the parameters Δ_1 and Δ_2) with the distance D_0 .

The merger of a BH-NS binary of masses $10M_\odot$ and $1.4M_\odot$ would produce a signal whose amplitude is 2.11 times stronger than the NS-NS merger of Fig. 12 [from Eq. (4.28) above]. Hence, taking also into account a cosmological enhancement factor of $(1+z)^{5/6}$ [9], a plot of

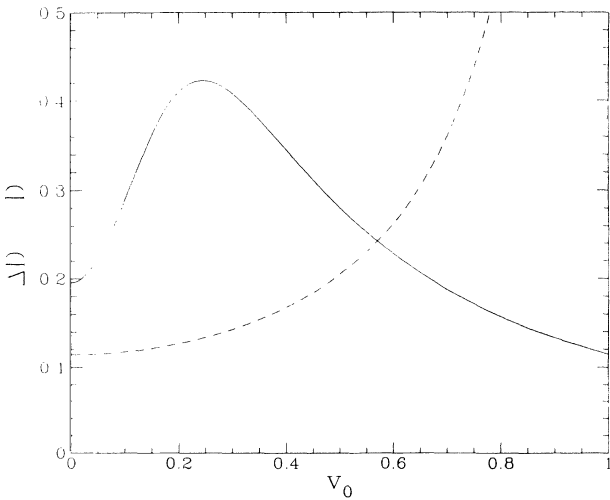


FIG. 11. The solid line shows the distance measurement accuracy $\Delta D/D$ for the binary merger discussed in the caption of Fig. 10 (for which $\Delta_1 = 0.10$, $\Delta_2 = 0.057$), as a function of the cosine of the angle of inclination, v_0 . The improvement in accuracy at high values of v_0 is due in part to an increased signal-to-noise ratio there. The dashed curve shows the prediction (4.41) of the linear error-estimation theory, which diverges as $v_0 \rightarrow 1$.

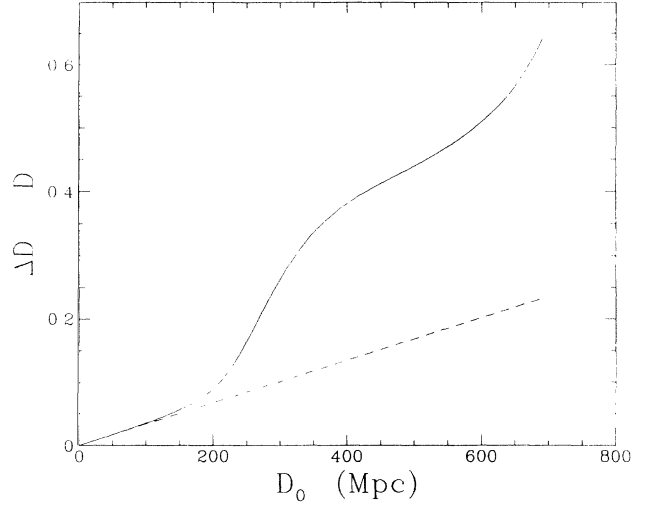


FIG. 12. The distance measurement accuracies that result from displacing along the line of sight to the Earth, to various distances D_0 , the binary merger of Fig. 10. As in Fig. 11, the dashed curve shows the approximate linear estimate (4.41), and the solid curve shows the more accurate estimate (4.62). The curves terminate at that distance (~ 700 Mpc) beyond which the merger is no longer visible, assuming the detector sensitivity level (2.1) and a combined signal-to-noise threshold of 8.5.

$\Delta D/D$ versus D_0 for a BH-NS binary otherwise the same as the binary in Fig. 10 would look roughly the same as Fig. 12, but rescaled to extend to luminosity distances ~ 2 Gpc (the exact value depending on the cosmological model) [9].

E. Simulation of what the LIGO-VIRGO network will measure

In order to explore more completely the distance measurement accuracy (4.62) over the whole parameter space, we carried out the following Monte Carlo calculation. Random values of D_0 , v_0 , $\bar{\psi}_0$, θ , and φ were chosen, distributed according to the measure $dD_0^3 dv_0 d\bar{\psi}_0 d\cos\theta d\varphi$. Those parameter choices for which the combined SNR (4.27) (for NS-NS binaries) was less than the threshold of 8.5 were discarded, and samples were generated until 1000 NS-NS signals had been “detected.” Because of this thresholding procedure (which roughly corresponds to the actual thresholding procedure that will be used), the distribution of values of D_0 , v_0 , etc., for detected events will not be given by $dD_0^3 dv_0 d\bar{\psi}_0 d\cos\theta d\varphi$. For example, there is a significant bias in detected events toward high values of v_0 , i.e., toward face-on binaries.

Scatterplots of the distances D_0 , signal-to-noise ratios ρ , and distance measurement accuracies (4.62) for these randomly generated data points are shown in Figs. 13–15. We used the LIGO-VIRGO network functions shown in Figs. 5 and 6. Figures 13–15 give some idea of the potential capability of the LIGO-VIRGO network. The distance scale in these graphs is determined by the detector sensitivity level (2.1) that we have assumed, which

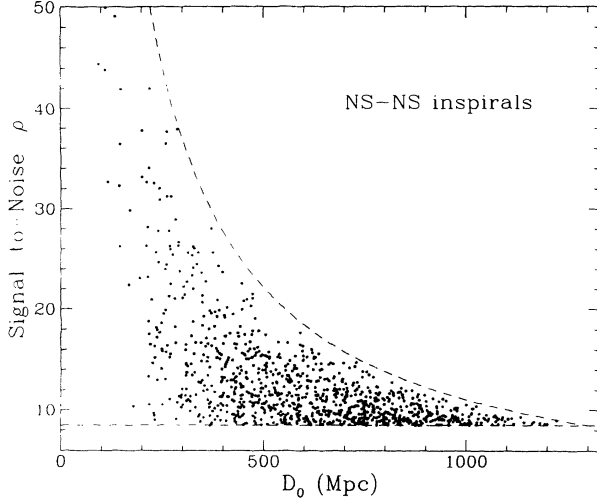


FIG. 13. The distances D_0 for 1000 NS-NS binaries whose locations and orientations were randomly chosen, and the corresponding predicted signal-to-noise ratios ρ for the LIGO-VIRGO network. The lower dashed line is the signal-to-noise threshold of 8.5, below which sample points were discarded; the upper dashed line shows the maximum possible value (4.49) of ρ at a given distance. Six points with ρ between 50 and 90 are not shown. The number of sources with ρ larger than a given value ρ_* is proportional to ρ_*^{-3} . The detection of this many binary inspirals with the advanced LIGO-VIRGO detectors would take several years, if merger rates are as currently estimated [1, 2], and assuming the detector sensitivity level (2.1).

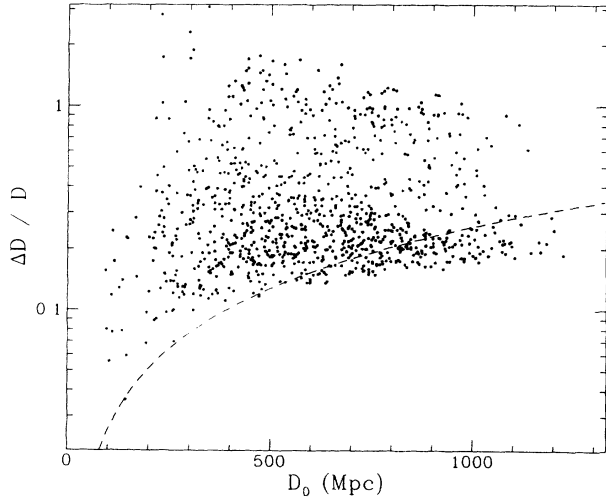


FIG. 14. The distance measurement accuracy $\Delta D/D$ computed from Eq. (4.62) for the same 1000 NS-NS binaries, versus the distance D_0 ; see caption of Fig. 13. The spread in the values of $\Delta D/D$ is due to different source directions and orientations. Note that the accuracy for sources within 200 Mpc (of which there are estimated to be ~ 3 per year [1, 2]) can vary between $\sim 2\%$ and $\sim 25\%$. For the most distant detectable sources (at ~ 1200 Mpc), the accuracy can sometimes be as good as $\sim 20\%$. The dashed line shows the theoretical lower bound (4.47) derived using the linear error-estimation formalism; points below this line mostly have values of v_0 close to one for which value the linear error-estimation theory fails.

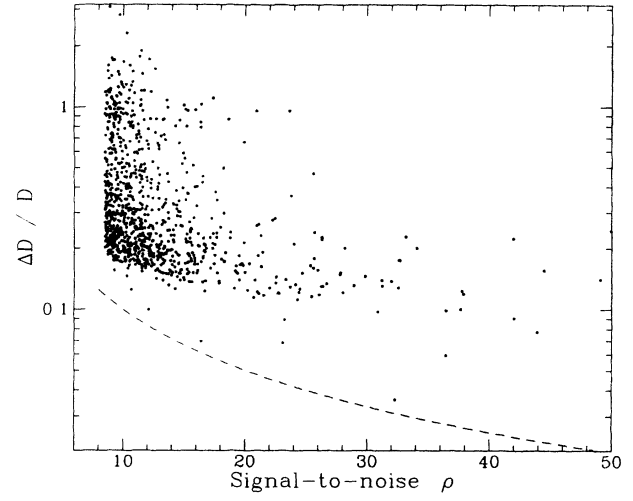


FIG. 15. Distance measurement accuracy versus signal-to-noise for the same 1000 NS-NS binaries; see caption of Fig. 13. The dashed line shows the theoretical lower bound (4.48). As in Fig. 13, six points with ρ between 50 and 90 are not shown.

is uncertain to within a factor of ~ 2 . The distance scale would also be 2 to 3 times larger for NS-BH binaries, as mentioned above. By contrast, the distribution of measurement accuracies, which we show in Fig. 16, is independent of the scale of the detector noise. This figure shows that the measurement accuracy will be better than 30% for over half of the detected sources.

A relatively large fraction, about 1/5, of detected events have poor ($\geq 50\%$) measurement accuracies. This

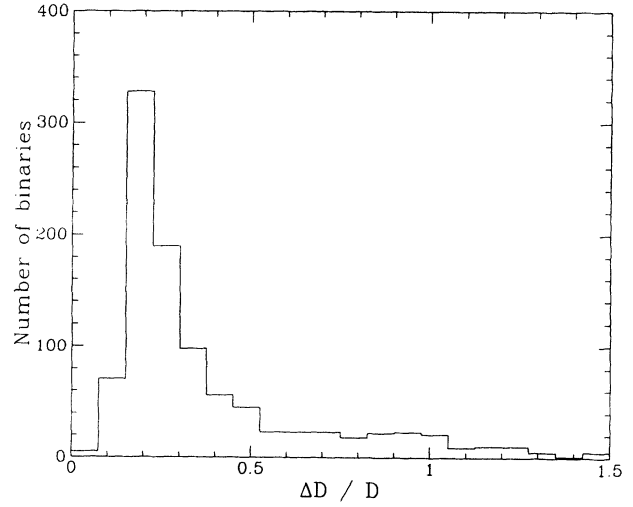


FIG. 16. The frequency of occurrence of different ranges of $\Delta D/D$, out of a total of 1000 signals, for the LIGO-VIRGO detector network. It can be seen that $\sim 8\%$ of detected signals will have distance measurement accuracies of better than 15%, while $\sim 60\%$ of them will have accuracies of better than 30%. These conclusions are insensitive to the overall scale of the detectors' intrinsic noise, which essentially sets the event-detection rate. By contrast, they are sensitive to the number of detectors in the detector network, and to their orientations; see text and also Fig. 9.

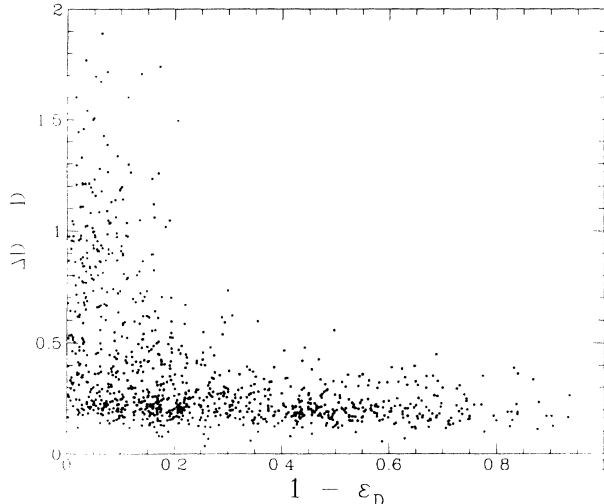


FIG. 17. Distance measurement accuracy versus the detector network polarization sensitivity $1 - \varepsilon_D(\mathbf{n})$, for 1000 NS-NS binaries; see caption of Fig. 13. The strong correlation between very poor distance-measurement accuracy and low polarization sensitivity is evident — essentially all points with $\Delta D/D > 0.5$ have $1 - \varepsilon_D \lesssim 0.2$.

is primarily due to the effect discussed in Sec. IV C: low values of the detector network polarization sensitivity $1 - \varepsilon_D(\mathbf{n})$ over much of the sky. The effect of the polarization sensitivity can be clearly seen in Fig. 17, which is a scatterplot of polarization sensitivity versus distance measurement accuracy.

Finally, we emphasize that our results should be regarded as fairly rough estimates, because we have neglected the following effects: (i) The spin-related modulation of the amplitudes \mathcal{A}_A mentioned in Sec. IV A and discussed in Ref. [43]; (ii) the correlations between the variables D, v and ψ, ϕ_c , except to linear order in $1/\rho$; and (iii) the correlations between the parameters D, v, ψ, ϕ_c and the “phase parameters” \mathcal{M}, μ, β . As discussed above, we show in Appendix C that these correlations vanish to linear order in $1/\rho$, but there will be some correlation effects at higher order. Despite these neglected effects, we feel that the approximation method that we have used based on Eqs. (4.57) and (4.60) gives results that are considerably more accurate than previous linear treatments [as summarized by Eq. (4.41)], because the dominant correlations at linear order in $1/\rho$ are those between D and v , and we have treated these correlations exactly.

V. CONCLUSIONS

Modulo the caveats in Sec. III C, we have confirmed the general conclusion that one can measure the binary’s chirp mass \mathcal{M} with rather astonishing accuracy. While our estimates of $\Delta\mathcal{M}/\mathcal{M}$ are a factor of ~ 20 greater than those obtained from the less accurate Newtonian analysis [14, 15], we have found that $\Delta\mathcal{M}/\mathcal{M}$ should still be 0.01%–1% for typical measurements.

We have investigated the idea that detailed phase information might also allow accurate determination of the

binary’s reduced mass μ . A calculation that neglected the effects of the bodies’ spins on the waveform suggested that μ might typically be measured to within $\sim 1\%$. However a more complete analysis showed that errors in μ can be substantially masked by compensating errors in the spin parameter β . Including the correlations with β , we estimated that $\Delta\mu/\mu \approx 10\%$ for low-mass (NS-NS) binaries and that $\Delta\mu/\mu \approx 50\%$ for high-mass (BH-BH) binaries. Moreover, $\Delta M_1/M_1$ and $\Delta M_2/M_2$ are generally much greater than $\Delta\mu/\mu$ unless $M_1/M_2 \gg 1$ (BH-NS case).

These results are somewhat disappointing; it would have been more exciting to find that post-Newtonian effects allow both masses to be determined to within a few percent. In this regard, however, it is useful to keep two points in mind. First, since typical measurements will have $S/N \approx 10$, one should detect events with $S/N \geq 50$ roughly 1% of the time. For the advanced-detector noise curve (2.1), and assuming the coalescence rates estimated in Ref. [2], such strong events should be seen \sim once per year for NS-NS binaries, and several times per year for NS-BH and BH-BH binaries [22]. For these strongest sources, measurement errors will be a factor of ~ 5 lower than their typical values. Second, the measurement-derived PDF on the parameter space constrains the values of M_1, M_2 , and β much more strongly than is indicated by their individual variances, as illustrated in Fig. 3 above. The large rms errors are due to correlations between the measured parameters; certain linear combinations of the parameters (eigenvectors of the covariance matrix) are determined with high accuracy [40]. This may be useful when combined with information obtained by other means.

With regard to potential accuracy of distance measurements, our key conclusions are the following.

(i) We have confirmed the general conclusion reached previously [15, 9] that correlations between the distance D and other angular variables (primarily the angle of inclination of the binaries orbit) will reduce ΔD by a factor of typically 2 or 3 from the naive estimate $\Delta D/D = 1/(signal-to-noise)$; see Fig. 15 above.

(ii) Distance measurement accuracy will depend strongly on the direction toward the source relative to the detectors, as shown in Figs. 7 and 8. This is because of the different *polarization sensitivities* of the detector network in different directions, and the fact that the complex amplitudes of both polarization components of the incident waves are needed in order to determine the distance. The polarization sensitivity of the LIGO-VIRGO network is somewhat poor in this regard (because the two LIGO detectors are almost parallel); it would be substantially improved by the addition of a fourth detector. This provides additional motivation for the construction of additional interferometers around the world, which would also improve the angular accuracy of sky-location measurements [7].

(iii) Previous estimates of distance measurement errors have been accurate only to linear order in $1/D$. Our results indicate that this linear approximation will be inadequate for typical detected signals, so that the incorporation of nonlinear effects will be necessary in order

to accurately ascertain measurement errors (and also to accurately estimate the distances themselves; see subsection A 3 of Appendix A).

(iv) We have carried out a Monte Carlo simulation of distance measurement accuracies for a large number of randomly chosen sources, using a method of calculation which roughly estimates the nonlinear effects, and incorporating the amplitude sensitivity and polarization sensitivity of the LIGO-VIRGO detector network. Our results suggest that $\sim 8\%$ of measured distances will be accurate to better than $\sim 15\%$, and that $\sim 60\%$ of them will be accurate to better than 30%.

ACKNOWLEDGMENTS

It is a pleasure to thank the following people for helpful discussions: Theocharis Apostolatos, Lars Bildsten, Sam Finn, Daniel Kennefick, Andrzej Krolak, Dragoljub Marković, Eric Poisson, Bernard Schutz, Gerald Sussman, Cliff Will, Alan Wiseman, and especially Kip Thorne, who provided much of the inspiration for this paper. We are grateful to Finn for sharing with us the results of his research, on which much of our work is based, at a preliminary stage. We thank Thorne and Bildsten for carefully reading the manuscript, and for detailed comments. Our understanding of some subtle issues in parameter estimation owes much to a recent review article by Tom Loredo [53]. This work was supported in part by NSF Grant No. PHY-9213508.

APPENDIX A: ESTIMATION OF SIGNAL PARAMETERS

In this appendix we review some aspects of the statistical theory of estimation of signal parameters as applied to gravitational wave astronomy. This subject has been concisely summarized in Appendix A of Ref. [27], and has recently been treated in detail by Finn [26]. Hence in many places we merely write down the key results, without proof, in order to establish notation and equations for use in the text. However, we also present some extensions to the formalism developed by Finn [26]: We carefully distinguish between Bayesian and frequentist estimates of errors, and discuss the validity of these two methods of error calculation. We show that maximum-likelihood parameter estimation, while useful, is not the optimal data-processing strategy, and, following Davis [53], suggest the use of the so-called Bayes estimator. We derive an expression for the minimum signal-to-noise ratio (S/N)_{min} necessary in order that the usual Gaussian approximation for estimation of measurement accuracy be valid, and explain how to treat degenerate points in parameter space at which the Gaussian approximation breaks down. Finally we give a discussion of the effects of including *a priori* information, which corrects the corresponding material in Ref. [26].

1. Basic formulas

The output of a network of detectors can be represented as a vector $\mathbf{s}(t) = (s_1(t), \dots, s_{n_d}(t))$, where n_d is

the number of detectors, and $s_a(t)$ is the strain amplitude read out from the a th detector. There will be two contributions to the detector output $\mathbf{s}(t)$ — the intrinsic detector noise $\mathbf{n}(t)$ (a vector random process), and the true gravitational wave signal $\mathbf{h}(t)$ (if present):

$$\mathbf{s}(t) = \mathbf{h}(t) + \mathbf{n}(t). \quad (\text{A1})$$

We assume that the signal is a burst of known form, but depending on several unknown parameters $\theta = (\theta^1, \dots, \theta^k)$, so that $\mathbf{h}(t) = \mathbf{h}(t; \theta)$. Thus, we do not consider the cases of periodic or stochastic waves [12]. We also assume for simplicity that the detector noise is stationary and Gaussian. For the LIGO and VIRGO detectors, the stationarity assumption is justified for the analysis of short, burst waves [27]. However, the actual noise may have important non-Gaussian components, the implications of which for the purposes of signal detection thresholds and data analysis are not yet fully understood. We do not deal with this issue here.

With these assumptions, the statistical properties of the detector noises can be described by the auto-correlation matrix

$$\begin{aligned} C_n(\tau)_{ab} &= \langle s_a(t + \tau) s_b(t) \rangle - \langle s_a(t + \tau) \rangle \langle s_b(t) \rangle \\ &= \langle n_a(t + \tau) n_b(t) \rangle - \langle n_a(t + \tau) \rangle \langle n_b(t) \rangle, \end{aligned} \quad (\text{A2})$$

where the angular brackets mean an ensemble average or a time average. The Fourier transform of the correlation matrix, multiplied by two, is the power spectral density matrix:

$$S_n(f)_{ab} = 2 \int_{-\infty}^{\infty} d\tau e^{2\pi i f \tau} C_n(\tau)_{ab}. \quad (\text{A3})$$

This satisfies the formal equation

$$\langle \tilde{n}_a(f) \tilde{n}_b(f')^* \rangle = \frac{1}{2} \delta(f - f') S_n(f)_{ab}, \quad (\text{A4})$$

or more generally and precisely

$$\begin{aligned} \left\langle \exp \left\{ i \int dt \mathbf{w}(t) \cdot \mathbf{n}(t) \right\} \right\rangle \\ = \exp \left\{ -\frac{1}{2} \int_0^{\infty} df \tilde{\mathbf{w}}^{\dagger} \cdot \mathbf{S}_n \cdot \tilde{\mathbf{w}} \right\}, \end{aligned} \quad (\text{A5})$$

for any sufficiently well-behaved test functions $w_a(t)$. Here tildes denote Fourier transforms, according to the convention that

$$\tilde{h}(f) = \int_{-\infty}^{\infty} e^{2\pi i f t} h(t) dt.$$

We note that there are two different commonly used definitions of power spectral density in the literature. The above convention is used in Refs. [3, 12, 26, 35, 44]. The alternative convention is to use a spectral noise density defined by $S_n^{(2)}(f) \equiv S_n(f)/2$, as used in Refs. [21, 27, 54–56].

The Gaussian random process $\mathbf{n}(t)$ determines a natural inner product $(\dots | \dots)$ and associated distance or norm on the space of functions $\mathbf{h}(t)$. As discussed in Sec. II B, this is defined so that the probability that the

noise takes a specific value $\mathbf{n}_0(t)$ is

$$p[\mathbf{n} = \mathbf{n}_0] \propto e^{-(\mathbf{n}_0|\mathbf{n}_0)/2}, \quad (\text{A6})$$

and it is given by [28]

$$\langle \mathbf{g} | \mathbf{h} \rangle \equiv 4 \operatorname{Re} \int_0^\infty df \tilde{g}_a(f)^* [\mathbf{S}_n(f)^{-1}]^{ab} \tilde{h}_b(f). \quad (\text{A7})$$

It also satisfies the equation [26]

$$\langle (\mathbf{n}| \mathbf{g}) (\mathbf{n}| \mathbf{h}) \rangle = \langle \mathbf{g} | \mathbf{h} \rangle, \quad (\text{A8})$$

for any functions \mathbf{g} and \mathbf{h} .

In this paper we are interested only in the estimation of signal parameters once a gravitational wave burst has been detected. Thus, we suppose that we have measured some detector output $\mathbf{s}(t)$, and that it satisfies the appropriate criterion for us to conclude that it contains a signal of the form $\mathbf{h}(t; \tilde{\theta})$ for some unknown set of parameters $\tilde{\theta}$:

$$\mathbf{s}(t) = \mathbf{h}(t; \tilde{\theta}) + \mathbf{n}(t). \quad (\text{A9})$$

The central quantity of interest is then the probability distribution function (PDF) for $\tilde{\theta}$ given the output $\mathbf{s}(t)$. As Finn has shown [26], this is given by

$$p[\tilde{\theta} | \mathbf{s}, \text{detection}] = \mathcal{N} p^{(0)}(\tilde{\theta}) e^{-\frac{1}{2}(\mathbf{h}(\tilde{\theta}) - \mathbf{s} | \mathbf{h}(\tilde{\theta}) - \mathbf{s})}. \quad (\text{A10})$$

Here $\mathcal{N} = \mathcal{N}(\mathbf{s})$ is a normalization constant, and $p^{(0)}(\tilde{\theta})$ is the PDF that represents our *a priori* knowledge.

2. Two types of measurement accuracy

We now discuss how to characterize the accuracy of measurement of the parameters θ . Normally statistical “ 1σ ” experimental errors are defined operationally in terms of the average of the actual errors over an ensemble of repeated identical measurements (which corresponds mathematically to the width of an appropriate PDF). Now in practice one cannot repeat or duplicate a given gravitational wave measurement, but in principle one can do so by waiting a sufficiently long time and throwing away all detected signals that do not match the original one. In this manner one can operationally define an ensemble of “identical” measurements. The notion of error which results then depends in a crucial way on what is meant by “identical.” One can either demand that the signals $\mathbf{h}(t)$ incident on the detectors be identical and consider the resulting spread in the values of the detector outputs $\mathbf{s}(t)$ given by Eq. (A9), or demand that the detector outputs $\mathbf{s}(t)$ be identical and consider the resulting spread in the values of the incident signals $\mathbf{h}(t)$. The two notions of error which result can be called Bayesian errors and frequentist errors, adopting the terminology from common usage in a more general context [52]. We now discuss in more detail the definition and meaning of these two types of error, in order to clarify the relationship between our method of calculating measurement error and previous work in this area [26, 27, 15,

61]. The following discussion is based on that of Loredo [52].

In the frequentist approach, one first specifies the algorithm the experimenters should use to determine the “best-fit” values $\hat{\theta}$ of the parameters θ from the gravitational wave measurement \mathbf{s} :

$$\hat{\theta} = \hat{\theta}(\mathbf{s}). \quad (\text{A11})$$

This is also called a statistic or estimator. Next, one assumes that Eq. (A9) holds for some value of $\tilde{\theta}$, and by substituting this equation into Eq. (A11), and using Eq. (A6), one derives the PDF $p(\hat{\theta} | \tilde{\theta})$ for $\hat{\theta}$ given $\tilde{\theta}$. Then the expected value with respect to this PDF of $\hat{\theta}^i - \tilde{\theta}^i$,

$$\begin{aligned} b^i &= \langle \hat{\theta}^i \rangle - \tilde{\theta}^i \\ &= \int \hat{\theta}^i p(\hat{\theta} | \tilde{\theta}) d\hat{\theta} - \tilde{\theta}^i, \end{aligned} \quad (\text{A12})$$

gives the “bias” b^i of the estimator $\hat{\theta}(\mathbf{s})$. The diagonal elements of the expected value of $(\hat{\theta}^i - \tilde{\theta}^i)(\hat{\theta}^j - \tilde{\theta}^j)$ characterize the measurement error. More specifically, we define

$$\begin{aligned} \Sigma_{\text{freq}}^{ij} &= \Sigma_{\text{freq}}^{ij}[\tilde{\theta}; \hat{\theta}(\cdot)] \\ &= \left\langle \left\{ \hat{\theta}^i [\mathbf{h}(\tilde{\theta}) + \mathbf{n}] - \tilde{\theta}^i \right\} \left\{ \hat{\theta}^j [\mathbf{h}(\tilde{\theta}) + \mathbf{n}] - \tilde{\theta}^j \right\} \right\rangle_{\mathbf{n}}. \end{aligned} \quad (\text{A13})$$

Here the notation on the first line indicates that Σ_{freq} depends on the functional form of the estimator $\hat{\theta}$ as well as the assumed signal parameters $\tilde{\theta}$, and the angular brackets on the second line denote expectation value with respect to the noise \mathbf{n} . The matrix (A13) is a measure of parameter-extraction accuracy that includes the effect of the bias, since

$$\Sigma_{\text{freq}}^{ij} = \langle \delta\hat{\theta}^i \delta\hat{\theta}^j \rangle + b^i b^j, \quad (\text{A14})$$

where $\delta\hat{\theta}^i \equiv \hat{\theta}^i - \langle \hat{\theta}^i \rangle$.

The physical meaning of the quantity (A13) is the following. Suppose that a large number of identical gravitational wave trains, described by the parameter values $\tilde{\theta}$, impinge on the detector network. For each measured signal, the experimenters calculate using the algorithm $\hat{\theta}$ the best-fit values of the source parameters. Then the rms average deviation of these best-fit values from the true value $\tilde{\theta}$ is given by Eq. (A13). Moreover, the usual method of implementing a Monte Carlo simulation of the measurement process would also predict errors given by (A13) [61].

In the frequentist method, one focuses attention on a particular incident signal $\mathbf{h}(t; \tilde{\theta})$, and considers different possible measured detector outputs $\mathbf{s}(t)$. By contrast, in the Bayesian approach, one focuses attention on a particular measured detector output \mathbf{s} . The error in measurement is simply taken to be the width (variance-covariance matrix) of the PDF (A10) for the true value $\tilde{\theta}$ of θ given the measurement \mathbf{s} . Thus,

$$\begin{aligned}\Sigma_{\text{Bayes}}^{ij} &= \Sigma_{\text{Bayes}}^{ij}[\mathbf{s}; p^{(0)}(\cdot)] \\ &= \int (\tilde{\theta}^i - \langle \tilde{\theta}^i \rangle) (\tilde{\theta}^j - \langle \tilde{\theta}^j \rangle) p(\tilde{\theta} | \mathbf{s}) d\tilde{\theta},\end{aligned}\quad (\text{A15})$$

where $\langle \tilde{\theta}^i \rangle = \int \tilde{\theta}^i p(\tilde{\theta} | \mathbf{s}) d\tilde{\theta}$. Note that this measure of error depends on different quantities than its frequentist counterpart (A13) — the measured signal \mathbf{s} , and the *a priori* PDF $p^{(0)}$.

The physical meaning of the quantity (A15) is the following. Suppose that a large number of different gravitational wave trains are incident upon the detector network, where the distribution of the wave parameters $\tilde{\theta}$ is given by the PDF $p^{(0)}$. Only a small fraction of these will produce, at the output of the detectors, the signal $\mathbf{s}(t)$. In this small fraction, however, there will be some spread of values of the parameters $\tilde{\theta}$, because of different realizations of the detector noise $\mathbf{n}(t)$ that combine with the incident waves to produce the measured signal according to Eq. (A9). This spread is characterized by the matrix (A15).

The measure of error (A15) characterizes the total amount of information that is contained in the measured signal \mathbf{s} , which is independent of how the experimenters choose to process this signal. In practical situations, however, one typically would like to know what accuracy can be achieved by a given, imperfect, data-processing algorithm (e.g., one which takes a manageable amount of computer time). It is possible to define a more general Bayesian error that is appropriate for the situation where a particular algorithm or statistic $\hat{\theta}(\cdot)$ is chosen to estimate the signal parameters θ from the measured signal \mathbf{s} . This measure of error is

$$\begin{aligned}\Sigma_{\text{Bayes}}^{ij} &= \Sigma_{\text{Bayes}}^{ij}[\mathbf{s}, \hat{\theta}(\mathbf{s}); p^{(0)}(\cdot)] \\ &= \int [\tilde{\theta}^i - \hat{\theta}(\mathbf{s})] [\tilde{\theta}^j - \hat{\theta}(\mathbf{s})] p(\tilde{\theta} | \mathbf{s}) d\tilde{\theta}.\end{aligned}\quad (\text{A16})$$

Physically this quantity is just the (square of the) rms average, over the small fraction of incident waves discussed above, of the difference between the true value $\tilde{\theta}$ of the parameters and the “measured value” $\hat{\theta}(\mathbf{s})$. It is clear that the rms errors $\Sigma_{\text{Bayes}}^{ii}[\mathbf{s}, \hat{\theta}(\mathbf{s}); p^{(0)}(\cdot)]$ will be minimized and take on their minimum values $\Sigma_{\text{Bayes}}^{ii}[\mathbf{s}; p^{(0)}(\cdot)]$ when one chooses for $\hat{\theta}$ the so-called Bayes estimator [54]

$$\hat{\theta}_{\text{Be}}^i(\mathbf{s}) \equiv \int \tilde{\theta}^i p(\tilde{\theta} | \mathbf{s}) d\tilde{\theta}. \quad (\text{A17})$$

One final point about Bayesian errors is the following. Suppose that the experimenters calculate from the measured signal \mathbf{s} the best-fit value $\hat{\theta} = \hat{\theta}(\mathbf{s})$, and then discard all the remaining information contained in the signal \mathbf{s} . Then there are very many signals \mathbf{s}' that could have been measured and that are compatible with the experimenters’ measurements, in the sense that $\hat{\theta}(\mathbf{s}') = \hat{\theta}$ [26]. Correspondingly, there is a larger spread of possible values of θ , and hence the predicted rms measurement errors based on the measurement $\hat{\theta}$ alone are given by the following modification of Eq. (A16):

$$\begin{aligned}\Sigma_{\text{Bayes}}^{ij} &= \Sigma_{\text{Bayes}}^{ij}[\hat{\theta}; p^{(0)}(\cdot)] \\ &= \int (\tilde{\theta}^i - \hat{\theta})(\tilde{\theta}^j - \hat{\theta}) p(\tilde{\theta} | \hat{\theta}) d\tilde{\theta}.\end{aligned}\quad (\text{A18})$$

Here $p(\tilde{\theta} | \hat{\theta})$ is the probability distribution introduced by Finn [26] for the true parameter values $\tilde{\theta}$ given the estimated values $\hat{\theta}$. It is given by the standard Bayesian formula

$$p(\tilde{\theta} | \hat{\theta}) = \bar{N} p^{(0)}(\tilde{\theta}) p(\hat{\theta} | \tilde{\theta}), \quad (\text{A19})$$

where $\bar{N} = \bar{N}(\hat{\theta})$ is a normalization constant that depends on $\hat{\theta}$. Note that the matrix (A18) depends only on the measured value $\hat{\theta}$ of the estimator and not on its functional form $\hat{\theta}(\cdot)$.

The predicted measurement error (A18) differs from the previously defined measurement error (A16) because the measured signal \mathbf{s} contains information about the likely size of the error, so that discarding \mathbf{s} makes a difference. For example, suppose that a detector-output data train contains a signal from a coalescing binary, and that by some standard algorithm the experimenters determine best-fit values of the binaries parameters. Then given these best-fit values, one can estimate the likely size of the measurement error — this is given by Eq. (A18). However, if they also determined that the data train contains an uncommonly large non-Gaussian burst of noise that accounts for 20% of the estimated signal amplitude, the estimates of the likely parameter-extraction errors would clearly have to be modified.

Which of the above-defined measurement errors is appropriate to assess the capability of the LIGO-VIRGO detector network? It is generally accepted that, if one has a given measurement \mathbf{s} , the Bayesian approach is the fundamental and correct one, and that the frequentist approach is justified only to the extent that it reproduces the results of Bayesian analyses. This is essentially because, given a particular measurement \mathbf{s} , it is irrelevant to consider an ensemble of other, different measurements \mathbf{s}' [52]. However, for our purpose of trying to *anticipate* the capability of gravitational wave detectors before any measurements are available, it seems that this message loses its bite. It certainly seems reasonable to imagine a fixed gravitational wave train incident upon the detector network, and to inquire about the spread (A13) in measured values of the source parameters due to differing realizations of the detector noise.

In fact, there is a certain sense in which frequentist errors and Bayesian errors are equivalent, which is well known: the average of the predicted frequentist error over the whole parameter space is the same as a suitable average of the predicted Bayesian error. Thus, in a sense the same errors are being calculated in each case; it is just their dependence on parameters that is being changed. In particular, if the predicted errors do not vary strongly with the parameters $\tilde{\theta}$, then the two types of error will be approximately equal. A precise statement of this “equality of averages” which is straightforward to derive is

$$\int d\tilde{\theta} p^{(0)}(\tilde{\theta}) \Sigma_{\text{freq}}^{ij}[\tilde{\theta}; \hat{\theta}(\cdot)] = \int \frac{\mathcal{D}\mathbf{s}}{\mathcal{N}(\mathbf{s})} \Sigma_{\text{Bayes}}^{ij}[\mathbf{s}, \hat{\theta}(\mathbf{s}); p^{(0)}(\cdot)] \quad (\text{A20a})$$

$$= \int \frac{d\hat{\theta}}{\bar{\mathcal{N}}(\hat{\theta})} \Sigma_{\text{Bayes}}^{ij}[\hat{\theta}; p^{(0)}(\cdot)]. \quad (\text{A20b})$$

Here the various matrices Σ^{ij} are defined in Eqs. (A13), (A16), and (A18), respectively, and the factors $\mathcal{N}(\mathbf{s})$ and $\bar{\mathcal{N}}(\hat{\theta})$ are the normalization constants appearing in Eqs. (A10) and (A19), respectively. The (formal) measure $\mathcal{D}\mathbf{s}$ is defined such that

$$\langle F[\mathbf{n}] \rangle = \int \mathcal{D}\mathbf{n} F[\mathbf{n}] e^{-(\mathbf{n}|\mathbf{n})/2}, \quad (\text{A21})$$

for any functional $F[\mathbf{n}]$ of the noise \mathbf{n} .

Because of this equality of averages, we conclude that either Bayesian or frequentist errors can be used to anticipate the capabilities of the LIGO-VIRGO network, essentially because one is only interested in the range of possible errors and not their value at a fixed point in parameter space. Similarly, if one is using Bayesian errors, it is appropriate to use the matrix (A18) instead of (A16) to anticipate measurement accuracies, since from Eqs. (A20) the measure of error (A18) is simply an average of (A16) over values of \mathbf{s} for which $\hat{\theta}(\mathbf{s}) = \hat{\theta}$. This conclusion has already been reached in a recent paper of Finn's [26] in which he advocates the use of what in our notation is essentially $\Sigma_{\text{Bayes}}^{ij}[\hat{\theta}_{\text{ML}}; p^{(0)}(\cdot)]$, where $\hat{\theta}_{\text{ML}}$ is the so-called maximum-likelihood estimator (see below). (However, his calculation of this quantity does not incorporate the *a priori* PDF quite correctly, as we show below.) Previous analyses of parameter-extraction accuracy for gravitational wave detectors by Echeverria [57] and by Krolak and collaborators [15, 27, 35, 61] have used the frequentist error $\Sigma_{\text{freq}}^{ij}[\tilde{\theta}; \hat{\theta}_{\text{ML}}(\cdot)]$. By contrast, in Sec. IV of this paper we have calculated the Bayesian error

$$\Sigma_{\text{Bayes}}^{ij}[\mathbf{s}; p^{(0)}(\cdot)] = \Sigma_{\text{Bayes}}^{ij}[\mathbf{s}, \hat{\theta}_{\text{Be}}(\mathbf{s}); p^{(0)}(\cdot)], \quad (\text{A22})$$

because, as we argue below, it is more accurate to use $\hat{\theta}_{\text{Be}}$ rather than $\hat{\theta}_{\text{ML}}$.

One final important point about the two types of error is the following well-known fact: to leading order in $1/\rho$, where ρ is the signal-to-noise ratio [Eq. (A27) below], the two approaches yield identical results. More specifically, assuming the Gaussian noise statistics (A6), we have

$$\Sigma_{\text{freq}}^{ij}[\tilde{\theta}; \hat{\theta}_{\text{ML}}(\cdot)] = \Sigma_{\text{Bayes}}^{ij}[\hat{\theta}_{\text{ML}}; p^{(0)}(\cdot)] \times [1 + O(\rho^{-1})] \quad (\text{A23})$$

when $\hat{\theta}_{\text{ML}} = \tilde{\theta}$. Moreover the same quantity [given by Eq. (A34) below] is also obtained to leading order using the Bayes estimator (A17), and also from the estimator-independent measure of error (A15). This is essentially because to this order, all the PDFs are Gaussian. These assertions are straightforward to prove using the tools developed by Finn [26], and moreover are well known in more general statistical contexts. Hence the distinctions that we have been drawing only matter when ef-

fects that are nonlinear in $1/\rho$ contribute significantly to the predicted accuracies (as for example when measuring distances to coalescing binaries), or when ρ is sufficiently small that the *a priori* information represented by $p^{(0)}$ becomes significant. (However, this may be the rule rather than the exception for typical detected gravitational wave bursts; see Sec. IV D above.)

3. Choice of data-processing algorithm $\hat{\theta}(\cdot)$

Given a particular measurement \mathbf{s} , the PDF (A10) in principle contains all the information contained in the measurement about the source parameters $\tilde{\theta}$. However in practice one often wants to focus on a small portion of this information, by calculating a "best estimate" value $\hat{\theta}(\mathbf{s})$ together with estimates of the statistical errors. The choice of estimator $\hat{\theta}(\cdot)$ is determined both by practical considerations, and by whatever criteria are adopted to judge "good" estimators; there is no unique choice.

One obvious criterion is to choose that estimator which minimizes the expected error in parameter extraction. However, one could choose to minimize either Bayesian or frequentist errors, and also the errors depend on the parameter values ($\tilde{\theta}$ or $\hat{\theta}$). If one minimizes the average over parameter space of the measurement error [as given by the common value of Eqs. (A20)], then the resulting best estimator is just the Bayes estimator (A17), which we have used in Sec. IV D. Its use for gravitational wave data analysis has been suggested by Davis [53]. Unfortunately, as Davis indicates, calculation of the Bayes estimator is very computationally intensive, as it typically involves a multidimensional integral of a function whose evaluation at each point requires the numerical calculation of an inner product of the type (A7). Our application of the Bayes estimator in Sec. IV D was an exception in this regard, because all the inner products could be evaluated analytically. Hence, it seems likely that the Bayes estimator will be used only after preliminary estimates of the signal parameters have been made using Wiener optimal filtering. The use of the Bayes estimator also goes by the name of "nonlinear filtering" [53].

A simpler estimator that has been proposed by Finn [26, 14], Krolak [61], and others in the gravitational wave data-analysis context is the so-called maximum-likelihood estimator $\hat{\theta}_{\text{ML}}(\mathbf{s})$. This is defined to be the value of $\tilde{\theta}$ which maximizes the PDF (A10). It is convenient because it is closely related to the Wiener optimal filtering method [12] that will be used to detect the signals — the detection procedure outlined in Sec. I will essentially return the maximum-likelihood estimates of the source parameters (see below). However, once the signals have been detected, there is no reason to only use maximum-likelihood estimation — other estimation methods can be used to give better results. Hence, the quantities $\Sigma_{\text{Bayes}}^{ij}[\hat{\theta}_{\text{ML}}; p^{(0)}(\cdot)]$ or $\Sigma_{\text{freq}}^{ij}[\tilde{\theta}; \hat{\theta}_{\text{ML}}(\cdot)]$ represent the *potential* accuracy of measurements only to leading order in $1/\rho$. (If maximum-likelihood estimation is the only estimation method used, then they represent the actual accuracy of measurement). We note that the quantities $\hat{\theta}_{\text{ML}}(\mathbf{s})$ and $\hat{\theta}_{\text{Be}}(\mathbf{s})$ can differ by substantial factors

for detected gravitational wave signals, as for example in Fig. 10 above where $\langle D \rangle = 1.44D_0$.

Maximum-likelihood estimation also has the following disadvantages. First, as discussed in Sec. IV D, the maximum-likelihood estimator for a particular variable does not necessarily maximize the reduced PDF for that variable obtained by integrating over the other variables. By contrast, the value of the Bayes estimator (A17) for a given variable does not depend on whether or not other variables have been integrated out. Second, the best-fit point obtained by the maximum-likelihood method depends on the choice of variables used to parametrize the waveform $\mathbf{h}(t; \tilde{\theta})$. For example, in Sec. III of this paper we could have used as variables either the individual masses M_1 and M_2 of the binaries components, or the chirp and reduced masses \mathcal{M} and μ . Since probability distributions for (M_1, M_2) and (\mathcal{M}, μ) are related by a nontrivial Jacobian factor, a local maximum of one of them will not correspond to a local maximum of the other. A slightly different kind of maximum-likelihood estimator, which maximizes the likelihood ratio $\Lambda(\tilde{\theta}) \propto \exp[-(\mathbf{h}(\tilde{\theta}) - \mathbf{s})^\top \mathbf{h}(\tilde{\theta}) - \mathbf{s}/2]$ instead of the PDF (A10), does not suffer from this problem. This is the maximum-likelihood estimator that is usually discussed in the statistics literature. However, it does not take into account in any way our *a priori* knowledge.

We conclude that calculations of measurement accuracy using $\hat{\theta}_{\text{ML}}$ represent the true potential measurement accuracy only to leading order in $1/\rho$. If this leading order approximation becomes invalid (as occurs for sufficiently small SNR's), then one should use instead either the Bayesian error (A22) or $\Sigma_{\text{Bayes}}^{ij}[\hat{\theta}_{\text{Be}}; p^{(0)}(\cdot)]$. One could also use $\Sigma_{\text{freq}}^{ij}[\tilde{\theta}; \hat{\theta}_{\text{Be}}(\cdot)]$, but this is much more difficult to calculate than (A22) when the large ρ limit does not apply.

4. Relation between maximum-likelihood estimation and Wiener optimal filtering

In Sec. II, we discussed a method for finding best-fit parameters $\hat{\theta}$ which was based on maximizing the overlap of the measured signal with theoretical templates [cf. Eq. (1.2) above]. We now briefly indicate the relationship of this method to the maximum-likelihood procedure. That the two methods are equivalent in general has been shown by Echeverria [58].

Given the measured signal $\mathbf{s}(t)$, define for any θ the quantity

$$\rho[\theta] = \frac{(\mathbf{h}(\theta) | \mathbf{s})}{\sqrt{(\mathbf{h}(\theta) | \mathbf{h}(\theta))}}. \quad (\text{A24})$$

This is the signal-to-noise ratio (SNR) defined in Eq. (1.2), and can be calculated by integrating the signal $\mathbf{s}(t)$ against a Wiener optimal filter whose Fourier transform is proportional to $\mathbf{S}_n(f)^{-1} \cdot \tilde{\mathbf{h}}(f; \theta)$. The quantity $\rho[\theta]$ is a random variable with Gaussian PDF of unit variance. Its expected value is zero if no signal is present, when $\mathbf{s}(t) = \mathbf{n}(t)$. If a signal is present, so that Eq. (A9) holds for some $\tilde{\theta}$, then the expected value of $\rho[\theta]$ is

$$\langle \rho[\theta] \rangle = \frac{(\mathbf{h}(\theta) | \mathbf{h}(\tilde{\theta}))}{\sqrt{(\mathbf{h}(\theta) | \mathbf{h}(\theta))}}. \quad (\text{A25})$$

Now if the *a priori* probability $p^{(0)}(\tilde{\theta})$ can be approximated to be constant, then the value $\hat{\theta}_{\text{ML}}$ of $\tilde{\theta}$ which maximizes the PDF (A10) for a given signal \mathbf{s} also maximizes $\rho[\theta]$ [58]. Hence we can find $\hat{\theta}_{\text{ML}}$ (up to the overall amplitude of the signal [59]) by computing the overlap (A24) of the signal with various templates, and by choosing the template which gives the maximum overlap.

When a signal is present and the signal-to-noise ratio is large, the maximum value $\rho[\hat{\theta}_{\text{ML}}]$ of $\rho[\theta]$ will approximately given by

$$\rho[\hat{\theta}_{\text{ML}}]^2 \approx (\mathbf{h}(\tilde{\theta}) | \mathbf{h}(\tilde{\theta})) \approx (\mathbf{h}(\hat{\theta}_{\text{ML}}) | \mathbf{h}(\hat{\theta}_{\text{ML}})). \quad (\text{A26})$$

The quantity

$$\rho^2 = (\mathbf{h}(\tilde{\theta}) | \mathbf{h}(\tilde{\theta})) \quad (\text{A27})$$

is what is usually referred to as the (square of) the SNR of the signal $\mathbf{h}(t; \tilde{\theta})$. When correlated sources of noise are unimportant so that the matrix (A3) is diagonal, this overall SNR will be given by combining in quadrature the SNR's for each individual detector, cf. Eq. (1.3) above.

5. The Gaussian approximation and conditions for its validity

We now consider the high signal-to-noise limit in which many of the subtleties that we have been discussing become unimportant. In particular, in this limit the Bayes and maximum-likelihood estimators become identical. From Eq. (A10), the maximum-likelihood estimator $\hat{\theta}_{\text{ML}}$ satisfies

$$(\mathbf{h}_{,i}(\hat{\theta}_{\text{ML}}) | \mathbf{h}(\hat{\theta}_{\text{ML}}) - \mathbf{s}) - [\ln p^{(0)}]_{,i}(\hat{\theta}_{\text{ML}}) = 0, \quad (\text{A28})$$

where the subscript $,i$ means derivative with respect to θ^i for $1 \leq i \leq k$, and k is the number of parameters. If the *a priori* information is unimportant so that the last term in Eq. (A28) is negligible, then as outlined in Sec. III the following simple geometric interpretation applies: Let \mathcal{S} be the finite dimensional surface formed by the set of all signals $\mathbf{h}(t; \theta)$ in the space of all possible signals $\mathbf{h}(t)$. Then the measured signal $\mathbf{s}(t)$ will generally not lie on the surface \mathcal{S} , and the best-fit point $\mathbf{h}(t; \hat{\theta}_{\text{ML}})$ is just that point on \mathcal{S} that is closest to $\mathbf{s}(t)$, where distance is measured using the norm $\|\mathbf{f}\|^2 \equiv (\mathbf{f} | \mathbf{f})$ derived from the inner product (A7). Correspondingly, $\mathbf{h}(\hat{\theta}_{\text{ML}})$ can be obtained by just dropping a perpendicular from $\mathbf{s}(t)$ onto the surface \mathcal{S} , which is the content of Eq. (A28) and is illustrated in Fig. 1.

When the SNR ρ is sufficiently large, one can find approximate expressions for $\Sigma_{\text{freq}}[\tilde{\theta}; \hat{\theta}_{\text{ML}}(\cdot)]$ and $\Sigma_{\text{Bayes}}[\hat{\theta}_{\text{ML}}; p^{(0)}(\cdot)]$. Such a calculation has been carried out by Finn [26]. We now briefly outline the calculation, and also extend it to determine the next-to-leading order terms in an expansion in $1/\rho$, in order to determine how large ρ needs to be for the leading order term to be a good approximation. Throughout this subsection

we assume that the *a priori* PDF $p^{(0)}$ is approximately constant; in Appendix A 6 we consider the effects of non-constant $p^{(0)}$.

First we find an approximate solution to Eq. (A28). Abbreviating $\hat{\theta}_{\text{ML}}$ as $\tilde{\theta}$, inserting Eq. (A9) into Eq. (A28) and expanding in the difference $\delta\theta = \hat{\theta} - \tilde{\theta}$, we obtain

$$\tilde{\theta}^i = \theta^i + [\Gamma(\tilde{\theta})^{-1}]^{ij} (\mathbf{n} | \mathbf{h}_{,j}) + \delta^{(2)}\theta^i + \delta^{(3)}\theta^i + O(\mathbf{n}^4). \quad (\text{A29})$$

Here

$$\Gamma(\tilde{\theta})_{ij} \equiv (\mathbf{h}_{,i}(\tilde{\theta}) | \mathbf{h}_{,j}(\tilde{\theta})) \quad (\text{A30})$$

is the so-called Fisher information matrix [cf. Eq. (2.7) above]. The second-order term $\delta^{(2)}\theta$ is

$$\begin{aligned} \delta^{(2)}\theta^i &= (\mathbf{n} | \mathbf{h}^i_{,j}) (\mathbf{n} | \mathbf{h}^j) \\ &- [(\mathbf{h}^i_{,j} | \mathbf{h}_k) + \frac{1}{2} (\mathbf{h}^i | \mathbf{h}_{jk})] (\mathbf{n} | \mathbf{h}^j) (\mathbf{n} | \mathbf{h}^k). \end{aligned} \quad (\text{A31})$$

$$\begin{aligned} {}^{(2)}\Sigma^{ij} &= (\mathbf{h}^i_{,k} | \mathbf{h}^{jk}) - (\mathbf{h}^i_{,k} | \mathbf{h}_l) (\mathbf{h}^{jk} | \mathbf{h}^l) + \frac{1}{4} (\mathbf{h}^i | \mathbf{h}^k_{,k}) (\mathbf{h}^j | \mathbf{h}^l_{,l}) + \frac{1}{2} (\mathbf{h}^i | \mathbf{h}_{kl}) (\mathbf{h}^j | \mathbf{h}^{kl}) \\ &- (\mathbf{h}^i | \mathbf{h}^{jk}_{,k}) - (\mathbf{h}^{ij} | \mathbf{h}_k^{,k}) + (\mathbf{h}^{ij} | \mathbf{h}_k) (\mathbf{h}^k | \mathbf{h}^l_{,l}) \\ &+ (\mathbf{h}^i | \mathbf{h}^{jk}) (\mathbf{h}_k | \mathbf{h}^l_{,l}) + 2(\mathbf{h}^i | \mathbf{h}_{kl}) (\mathbf{h}^k | \mathbf{h}^{jl}). \end{aligned} \quad (\text{A35})$$

In the case where there is only one variable so that $\theta = (\theta^1, \dots, \theta^k) = (\theta^1)$, it follows from Eqs. (A33) and (A35) that

$$\Sigma_{\text{freq}}^{11} = \frac{1}{(\mathbf{h}' | \mathbf{h}')^2} \left[1 - \frac{(\mathbf{h}' | \mathbf{h}'')}{(\mathbf{h}' | \mathbf{h}')^2} + \frac{15}{4} \frac{(\mathbf{h}'' | \mathbf{h}')^2}{(\mathbf{h}' | \mathbf{h}')^3} \right], \quad (\text{A36})$$

where primes denote derivatives with respect to θ^1 . The correction terms in the square brackets in this expression will be small whenever

$$\|\mathbf{h}''\| \ll \|\mathbf{h}'\|^2 \quad \text{and} \quad \|\mathbf{h}'''\| \ll \|\mathbf{h}'\|^3. \quad (\text{A37})$$

Using Eq. (A7), the equation $\rho^2 = (\mathbf{h} | \mathbf{h})$, and assuming for simplicity that $\mathbf{S}_n(f) = S_n(f)\mathbf{1}$, this reduces to the condition

$$\rho^2 \gg \frac{\langle\langle (\tilde{\mathbf{h}}'^{\dagger} \cdot \tilde{\mathbf{h}}'') / (\tilde{\mathbf{h}}^{\dagger} \cdot \tilde{\mathbf{h}}) \rangle\rangle}{\langle\langle (\tilde{\mathbf{h}}'^{\dagger} \cdot \tilde{\mathbf{h}}') / (\tilde{\mathbf{h}}^{\dagger} \cdot \tilde{\mathbf{h}}) \rangle\rangle^2}, \quad (\text{A38})$$

where for any function of frequency $F(f)$, we define the weighted average $\langle\langle F(f) \rangle\rangle$ to be $(F\mathbf{h} | \mathbf{h}) / (\mathbf{h} | \mathbf{h})$.

Equations (A37) or (A38) give sufficient conditions for the Gaussian approximation to be valid, when there is only one unknown parameter θ^1 . When there are several unknown parameters, a generalization of Eq. (A37) is obtained by interpreting the prime to mean the operator $v^i \partial / \partial \theta^i$ that differentiates in some direction v^i in the space of parameters θ , and requiring the condition to hold for all directions v^i . This yields the condition

$$\|\mathbf{h}_{,ij} v^i v^j\| \ll \|\mathbf{h}_{,i} v^i\|^2 = \Gamma_{ij} v^i v^j, \quad (\text{A39})$$

which is required to hold for all v^i . We note that,

In this expression and below we have for brevity omitted the commas denoting derivatives, and all quantities are evaluated at $\tilde{\theta}$. We lower and raise indices with the tensor (A30) and its inverse, so that, for example,

$$\mathbf{h}^i_{,j} \equiv (\Gamma^{-1})^{ik} \mathbf{h}_{,kj}. \quad (\text{A32})$$

There is a similar expression for $\delta^{(3)}\theta^i$. Equations (A29) and (A6) now determine the PDF $p(\hat{\theta} | \tilde{\theta})$. Using Eq. (A8) and its extension to fourth-order moments, and Eqs. (A29) and (A13), we obtain

$$\Sigma_{\text{freq}}^{ij}[\tilde{\theta}; \hat{\theta}_{\text{ML}}(\cdot)] = (\Gamma^{-1})^{ij} + {}^{(2)}\Sigma^{ij}. \quad (\text{A33})$$

At leading order, $p(\hat{\theta} | \tilde{\theta})$ is a multivariate Gaussian with mean $\tilde{\theta}$ and variance-covariance matrix given by the first term in Eq. (A33):

$$\Sigma = \Gamma^{-1}, \quad (\text{A34})$$

cf. Eq. (2.6) above. The correction term in Eq. (A33) is

although Eq. (A33) does correctly indicate the regime (A38) where the Gaussian approximation is valid, the correction term ${}^{(2)}\Sigma^{ij}$ is *not* an accurate expression for the leading-order correction to the measurement accuracy, because as we have argued above the true potential measurement accuracy is given by using the estimator $\hat{\theta}_{\text{Be}}(\cdot)$ and not $\hat{\theta}_{\text{ML}}(\cdot)$.

One frequent source of confusion about the leading order expression (A34) for the measurement error is the following. A general theorem in statistics called the Cramer-Rao inequality [27, 55] states that for *any* unbiased estimator $\hat{\theta}$ [60],

$$\Sigma_{\text{freq}}[\tilde{\theta}; \hat{\theta}(\cdot)] \geq \Gamma(\tilde{\theta})^{-1}. \quad (\text{A40})$$

Hence, one might imagine that the quantity (A34) is a lower bound for the accuracy obtainable by most reasonable estimators, and also for low signal-to-noise ratios. That this is not the case can be seen from the following consideration, which we discuss in the body of the paper: at degenerate points $\tilde{\theta}_0$ for which the signal derivatives $\partial \mathbf{h} / \partial \theta^i$ become linearly dependent, the matrix (A30) becomes degenerate, and the predicted rms errors given by the matrix (A34) become infinite. More careful calculations of, for example, $\Sigma_{\text{freq}}[\tilde{\theta}; \hat{\theta}_{\text{ML}}(\cdot)]$ at such degenerate points, going beyond linear order, give finite results. Hence the inverse of the Fisher matrix is *not* a generic, useful lower bound. The reason that the Cramer-Rao inequality does not apply is that most estimators are not unbiased and cannot easily be made so. When one generalizes the inequality (A40) to incorporate the effects of bias [55], an extra factor appears on the right-hand side multiplying the Fisher matrix, which can be small.

This can allow $\Sigma_{\text{freq}}[\tilde{\theta}; \hat{\theta}(\cdot)]$ to be much smaller than the inverse of the Fisher matrix, for some statistics $\hat{\theta}$.

6. Incorporation of *a priori* probabilities

We now turn to the effects of *a priori* information. First, we remark that it is not necessary for *a priori* information to be very detailed or restrictive in order that it have a significant effect on parameter-extraction accuracy. All that is necessary is that it be more restrictive than the information contained in the waveform, for some of the parameters θ^i . In other words it will be important whenever the statistical error $\langle (\Delta\theta^i)^2 \rangle$ which we obtain from Eq. (A34) for some parameter θ^i is much larger than our *a priori* constraints on θ^i . For example, this would be the case if we obtained rms errors for measurements of the dimensionless spin parameter a of a black hole to be larger than one, since we expect $|a| \leq 1$ always. If we include such poorly determined variables in a calculation of the variance-covariance matrix Σ and neglect the *a priori* restrictions, then the results obtained for the rms error in θ^i may be severely overestimated. This is not unexpected; what is more surprising is that due to the effects of correlations, the rms errors obtained for the other parameters may also be overestimated by large factors (see, e.g., Sec. III B above). We now extend the approximate calculations of the previous subsection to incorporate *a priori* information, and also now calculate Bayesian as well as frequentist errors. Our results in this subsection correct Eq. (3.19) of Ref. [26].

Roughly speaking, *a priori* information will be unimportant when the PDF $p^{(0)}$ does not vary substantially within 1 or 2σ of the best-fit point $\hat{\theta}$. This condition is logically independent of the condition (A38), although both will be satisfied in the high ρ limit. Hence, we can treat separately deviations from the leading order measurement accuracy (A34) that are due to second-order derivatives $\mathbf{h}_{,ij}$ of the signal [cf. Eq. A35 above], and that are due to *a priori* information. In the remainder of this subsection we therefore assume the condition (A38) and consistently neglect all second-order derivatives $\mathbf{h}_{,ij}$. In particular we treat the Fisher matrix (A30) as a constant in this approximation. [Note that our results will be exact in the case where the dependence of $\mathbf{h}(\tilde{\theta})$ on the parameters $\tilde{\theta}$ is exactly linear, as in Sec. IV D above.]

We start by considering the Bayes error (A15). When we neglect second-order derivatives of \mathbf{h} we find that the PDF (A10) takes the form

$$\begin{aligned} p[\tilde{\theta} | \mathbf{s}, \text{detection}] &= \mathcal{N}' p^{(0)}(\tilde{\theta}) \\ &\times \exp[-\frac{1}{2}\Gamma_{ij}(\tilde{\theta}^i - s^i)(\tilde{\theta}^j - s^j)]. \end{aligned} \quad (\text{A41})$$

Here we have decomposed the measured signal according to

$$\mathbf{s} = s^j \mathbf{h}_{,j} + \mathbf{s}^\perp, \quad (\text{A42})$$

where $(\mathbf{h}_{,i} | \mathbf{s}^\perp) = 0$ for $1 \leq i \leq k$, and have absorbed a factor of $\exp[-||\mathbf{s}^\perp||^2/2]$ into the normalization con-

stant \mathcal{N}' . If the PDF $p^{(0)}$ simply restricts the allowed ranges of the parameters, then the PDF (A41) is a truncated Gaussian distribution whose variance-covariance matrix $\Sigma_{\text{Bayes}}[\mathbf{s}; p^{(0)}(\cdot)]$ will normally be within a factor of ~ 2 or so of Γ^{-1} . If $p^{(0)}$ is approximately Gaussian with variance-covariance matrix Σ_0 , then we see from Eqs. (A15) and (A41) that

$$\Sigma_{\text{Bayes}}[\mathbf{s}; p^{(0)}(\cdot)] = \{\Gamma + \Sigma_0^{-1}\}^{-1}. \quad (\text{A43})$$

This is the formula which we use in Sec. III B above to incorporate our *a priori* knowledge about the spin parameter β .

Next we calculate an approximate expression for the second type of Bayesian error given by Eq. (A18), which is appropriate for the situation where we discard all information about the measured signal \mathbf{s} except the best estimate values $\hat{\theta}(\mathbf{s})$ of the parameters. For simplicity, we assume that $p^{(0)}(\tilde{\theta})$ is a Gaussian with mean θ_0 and width Σ_0 . We also use the maximum-likelihood estimator $\hat{\theta}_{\text{ML}}$; however, the same results are obtained for the Bayes estimator $\hat{\theta}_{\text{Be}}$. From Eqs. (A28) and (A9) and neglecting second-order derivatives of \mathbf{h} , we find

$$(\Sigma_1^{-1})_{ij} (\hat{\theta}_{\text{ML}}^j - \tilde{\theta}^j) = (\mathbf{h}_{,i} | \mathbf{n}) + (\Sigma_0^{-1})_{ij} (\theta_0^j - \tilde{\theta}^j), \quad (\text{A44})$$

where $\Sigma_1^{-1} \equiv \Gamma + \Sigma_0^{-1}$. Together with Eq. (A8) this implies that

$$p(\hat{\theta}_{\text{ML}} | \tilde{\theta}) \propto \exp\left[-\frac{1}{2}\mathbf{v}^T \cdot \Gamma \cdot \mathbf{v}\right], \quad (\text{A45})$$

where

$$\mathbf{v} = \hat{\theta} - \Sigma_1 \cdot \Gamma \cdot \tilde{\theta} - \Sigma_1 \cdot \Sigma_0^{-1} \cdot \theta_0 \quad (\text{A46})$$

$$= \Sigma_1 \cdot \Gamma \cdot (\tilde{\theta} - \text{const}). \quad (\text{A47})$$

Using Eqs. (A13), (A45), and (A46) we see that the result (A33) becomes modified to read

$$\Sigma_{\text{freq}}[\tilde{\theta}; \hat{\theta}_{\text{ML}}(\cdot)] = \Gamma^{-1} + \mathbf{b} \otimes \mathbf{b}, \quad (\text{A48})$$

where the bias $\mathbf{b} = \Sigma_1 \cdot \Sigma_0^{-1} \cdot (\theta_0 - \tilde{\theta})$. A more interesting quantity is the Bayesian error (A18), which from Eqs. (A19) and (A47) is given by

$$\begin{aligned} \Sigma_{\text{Bayes}}[\hat{\theta}_{\text{ML}}; p^{(0)}(\cdot)]^{-1} &= \Sigma_{\text{Bayes}}[\hat{\theta}_{\text{Be}}; p^{(0)}(\cdot)]^{-1} \\ &= \Sigma_0^{-1} + \Gamma \cdot \Sigma_1 \cdot \Gamma \cdot \Sigma_1 \cdot \Gamma. \end{aligned} \quad (\text{A49})$$

This expression gives approximately the same results as Eq. (A43), the differences never being more than $\sim 25\%$. The variances Σ^{ii} given by Eq. (A49) are always larger than those given by Eq. (A43), as a result of our having thrown away all the information in \mathbf{s} apart from $\hat{\theta}(\mathbf{s})$.

The result (A49) disagrees with a corresponding analysis of Finn (Eq. (3.19) of Ref. [26]). The reason for the disagreement is that Finn solves Eq. (A28) to obtain $\tilde{\theta}$ as a function of $\hat{\theta}_{\text{ML}}$ and \mathbf{n} , and then invokes the PDF (A6) of the noise to find $p(\tilde{\theta} | \hat{\theta}_{\text{ML}})$. This method of calculation [analogous to the method used for calculating $p(\hat{\theta}_{\text{ML}} | \tilde{\theta})$]

is invalid because it implicitly assumes that

$$p[\mathbf{n} = \mathbf{n}_0 | \hat{\theta}_{\text{ML}}] = p[\mathbf{n} = \mathbf{n}_0], \quad (\text{A50})$$

which is not the case. The fact that Eq. (A50) does not hold can be seen from the joint PDF for $\tilde{\theta}$, $\hat{\theta}_{\text{ML}}$ and \mathbf{n} , which is

$$p[\hat{\theta}_{\text{ML}}, \tilde{\theta}, \mathbf{n}] \propto p^{(0)}(\tilde{\theta}) e^{-(\mathbf{n} \cdot \mathbf{n})/2} \delta(\hat{\theta}_{\text{ML}} - \hat{\theta}_{\text{ML}}[\mathbf{h}(\tilde{\theta}) + \mathbf{n}]). \quad (\text{A51})$$

7. Treatment of degenerate variables

As we have noted in Sec. IV D, the accuracy of the linear approximation (A39) which yields the simple PDF (A41), depends in part on what set of variables θ^i are used in the calculation. A different PDF will be obtained from this approximation if one first makes a nonlinear change of coordinates $\theta^i \rightarrow \bar{\theta}^i(\theta^j)$. Hence, the PDF (A41) will approximate most closely the true PDF when it is computed using variables for which $\mathbf{h}_{,ij}$ is as small as possible.

Consequently, there are two qualitatively different ways in which the linear approximation may break down. First, for sufficiently low signal-to-noise ratios, the extrinsic curvature of the surface \mathcal{S} formed by the set of waveforms $\mathbf{h}(t; \theta)$ may be sufficiently large that Eq. (A39) is not a good approximation for *any* set of coordinates θ^i . In this case the “Gaussian” method breaks down completely. Second, the approximation may break down simply because of a bad choice of coordinates. This is usually the case at points of degeneracy where the vectors $\partial\mathbf{h}/\partial\theta^i$ become linearly dependent, which we discuss in Secs. III and IV and at the end of Appendix A 5 above. At such points the straightforward linear approximation method breaks down, but can usually be remedied by first making a nonlinear change of variables, applying the linear approximation, and then changing back to the original variables. One then obtains a PDF in terms of the original variables which is non-Gaussian, as in Sec. IV D above, from which measurement errors can be calculated. As has been pointed out by Marković [9], measurement errors at such points typically scale like $1/\sqrt{\rho}$ instead of like $1/\rho$. This will be true if the lowest-order derivative of \mathbf{h} , which is nonvanishing in all directions, is the second derivative.

APPENDIX B: APPROXIMATE CONSTANCY OF THE SPIN PARAMETER β THAT INFLUENCES THE WAVEFORM’S PHASE

The leading order contribution of the bodies’ spins to the secular growth of the gravitational-wave phase has been derived by Kidder, Will, and Wiseman [41], and is given by the term proportional to $4\pi - \beta$ in Eq. (3.20). The quantity β is defined by Eq. (3.21) and depends on the masses of the two bodies M_1 and M_2 , their spins \vec{S}_1 and \vec{S}_2 , and the unit vector in the direction of the orbital angular momentum \hat{L} . Over the course of the inspiral β will evolve, because the directions of the vectors \hat{L} , \vec{S}_1 , \vec{S}_2 will be changing due to spin-orbit and spin-spin

interactions.

Nevertheless, in our analysis in the body of the paper, we have assumed that the factor $\chi = 4\pi - \beta$ which appears in Eq. (3.20) can be treated as constant. This assumption is necessary to make the analysis tractable. In this appendix we present evidence which strongly suggests that χ is always constant apart from some small amplitude oscillations, showing that our assumption of constant χ is a reasonable one for all coalescing binaries. We calculate the evolution of χ by integrating the orbit-averaged equations (3.22) governing the evolution of the spins, using both analytic and numerical methods. A more complete discussion of the evolution of the spins and orbital angular momentum, and of their influence on the emitted gravitational waves, can be found in Ref. [43].

We start by introducing some dimensionless variables. Let \hat{S}_j be the unit vector in the direction of \vec{S}_j for $j = 1, 2$, and define

$$\alpha_1 = \hat{S}_1 \cdot \hat{L}, \quad (\text{B1})$$

$$\alpha_2 = \hat{S}_2 \cdot \hat{L}, \quad (\text{B2})$$

$$\alpha_3 = \hat{S}_1 \times \hat{S}_2 \cdot \hat{L}, \quad (\text{B3})$$

and

$$\alpha_4 = \hat{S}_1 \cdot \hat{S}_2. \quad (\text{B4})$$

The α_j ’s are not all independent variables as they satisfy the constraint

$$\alpha_1^2 + \alpha_2^2 + \alpha_3^2 + \alpha_4^2 = 1 + 2\alpha_1\alpha_2\alpha_4. \quad (\text{B5})$$

The reason that it is convenient to use these variables is the following. The spin-evolution equations (3.22) comprise nine equations in nine unknowns, with three conserved quantities (the magnitudes of the three vectors). Thus, there are effectively 6 degrees of freedom. If we specify the three independent values of the variables $\alpha_1, \dots, \alpha_4$, then the remaining 3 degrees of freedom can be parametrized by an overall rotation matrix. More precisely, given the vectors \hat{S}_1 , \hat{S}_2 , and \hat{L} , there will be a unique rotation matrix \mathbf{R} which takes \hat{L} into $\hat{L}' = \hat{e}_z$ (the unit vector along the z axis), \hat{S}_1 into a vector \hat{S}'_1 in the x - z plane, and \hat{S}_2 into some \hat{S}'_2 . The vectors \hat{S}_1 , \hat{S}_2 , and \hat{L} are determined by \mathbf{R} and by the variables $\alpha_1, \dots, \alpha_4$. Hence, the variables $\alpha_j(t)$ for $1 \leq j \leq 4$ and $\mathbf{R}(t)$ can be used instead of the vectors themselves to parametrize a solution to the spin-evolution equations. Now it turns out that the evolution of the α_j ’s *decouples* from the evolution of \mathbf{R} , in the sense that each $d\alpha_j/dt$ depends only on $\alpha_1, \dots, \alpha_4$ and is independent of \mathbf{R} . This greatly simplifies our analysis.

If we use units in which $M = 1$ and define $s_j = |\vec{S}_j|$ for $j = 1, 2$, then we obtain from Eqs. (3.22), (B1), and (2.10) the following coupled system of equations for $\alpha_1, \dots, \alpha_4$:

$$\frac{d\alpha_1}{dr} = \frac{-15}{128\mu} \left[\frac{1}{M_2} - \frac{s_1\alpha_1}{L} \right] s_2\alpha_3, \quad (\text{B6})$$

$$\frac{d\alpha_2}{dr} = \frac{15}{128\mu} \left[\frac{1}{M_1} - \frac{s_2\alpha_2}{L} \right] s_1\alpha_3, \quad (\text{B7})$$

$$\frac{d\alpha_4}{dr} = \frac{-15\alpha_3}{128\mu} \left[\left(\frac{M_2}{M_1} - \frac{M_1}{M_2} \right) L + s_1\alpha_1 - s_2\alpha_2 \right]. \quad (\text{B8})$$

Here $L \equiv \mu\sqrt{r}$ denotes the magnitude of the orbital angular momentum, and we have changed the dependent variable from time t to orbital separation r . The omitted equation for $d\alpha_3/dr$ can be obtained by combining Eqs. (B5) – (B8). From Eq. (3.21), the spin parameter β is given in terms of these variables by

$$\beta = \frac{113}{12}(s_1\alpha_1 + s_2\alpha_2) + \frac{25}{4M_1M_2} (M_2^2s_1\alpha_1 + M_1^2s_2\alpha_2). \quad (\text{B9})$$

We have numerically integrated Eqs. (B6)–(B8) for various initial spin and angular momentum directions, for the cases of NS-NS, NS-BH, and BH-BH binaries. We assumed all neutron stars have masses of $1.4M_\odot$, and black holes have masses $10M_\odot$. We integrated inward, starting at that value of r at which the emitted waves enter the LIGO-VIRGO waveband at 10 Hz, and ending at $r = 6M$ near the last stable circular orbit [30]. In the special case that one of the spins vanishes, it can be seen from Eqs. (3.21) and (3.22) that β will be conserved [43]. Hence we took both spins to be nonvanishing. We also assumed that their magnitudes are maximal, so that $s_j = M_j^2$ for $j = 1, 2$ [cf. Sec. III B], as these are the values which can be expected to give the largest changes in β .

Typical results are shown in Figs. 18–20. The factor $\chi = 4\pi - \beta$ undergoes small oscillations with an amplitude of order 0.1 which is small compared to the mean value of χ . This mean value depends on the mass ratio and on the initial spin directions, but always lies between $4\pi - \beta_{\max} \approx 3$ and $4\pi + \beta_{\max} \approx 22$, where β_{\max} is as given in Sec. III B. The angles between the vectors given by $\alpha_1, \dots, \alpha_4$ also oscillate, all with the same frequency. [This frequency is *not* the frequency with which the total spin $\vec{S} = \vec{S}_1 + \vec{S}_2$ precesses around \vec{L} [43], as that pre-

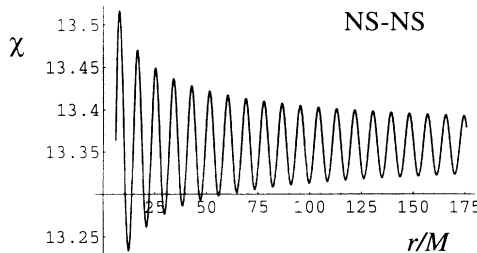


FIG. 18. During the last few minutes of inspiral, the angles between the bodies' spins \vec{S}_1 , \vec{S}_2 and the orbital angular momentum \vec{L} all oscillate, in addition to and separately from the precession of the total spin $\vec{S} = \vec{S}_1 + \vec{S}_2$ around \vec{L} . This oscillation gives rise to an oscillation of the parameter $\chi = 4\pi - \beta$ which governs the contribution of the spins to the accumulated phase of the emitted gravitational waves [cf. Eq. (3.20)]. Here we show a typical plot of χ as a function of the orbital separation r , for a NS-NS binary. The spin and orbital angular momentum directions were taken to be $\vec{S}_1 \propto \vec{i} + \vec{k}$, $\vec{S}_2 \propto -\vec{j}$, and $\vec{L} \propto \vec{i} + \vec{j}$ at the initial gravitational wave frequency of 10 Hz. The spin of each neutron star was assumed to have the maximal magnitude of $(1.4M_\odot)^2$, corresponding to a rotation period of a few milliseconds. It can be seen that in each case the amplitude of oscillation of χ is very small compared to its mean value, so that to a good approximation we can take $\chi = \text{const.}$

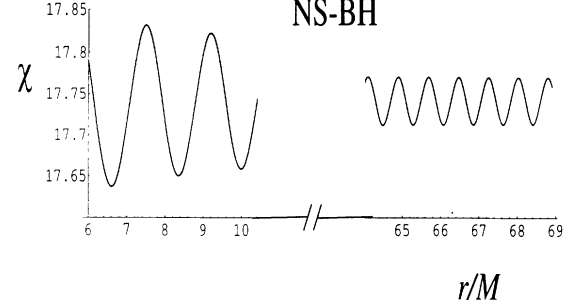


FIG. 19. The evolution of χ for a NS-BH binary; see caption of Fig. 18. The black hole was assumed to be maximally rotating.

cession does not change the angles between the vectors, and thus is not described by Eqs. (B6) – (B8).]

Some insight into the behavior of the general solutions to Eqs. (B6) – (B8) can be gained by considering the special case when the magnitude of one of the spins (say \vec{S}_1) is small, so that $s_1 \equiv |\vec{S}_1|/M^2 \ll 1$. This condition will sometimes be satisfied by NS-NS and BH-BH binaries, but will always be satisfied by NS-BH binaries since all compact bodies satisfy $|\vec{S}_j| \lesssim M_j^2$. Below we find analytic solutions to first order in s_1 . As we now describe, in the approximation $s_1 \ll 1$ the amplitude of the oscillations of β (and hence also of χ) is always smaller than $\sim 1/4$, for all initial spin directions and for all mass ratios. Although rapidly spinning NS-NS and BH-BH binaries will not satisfy $s_1 \ll 1$, nevertheless we find that amplitudes of the oscillations of β in the numerical solutions agree roughly with those predicted by the small spin approximation. (For some special initial spin directions, such as $\alpha_1 = \alpha_3 = 0$, the analytic solutions are poor approximations to the numerical solutions, but in all such cases that we have checked, the amplitudes of the β oscillations are still $\lesssim 0.2$.)

The solutions to first order in s_1 can be written as

$$\alpha_j(r) = \alpha_j^{(0)}(r) + \alpha_j^{(1)}(r) s_1 + O(s_1^2), \quad (\text{B10})$$

for $1 \leq j \leq 4$. Now as we have already mentioned, it can be seen from Eqs. (3.21) and (3.22) that when $s_1 = 0$, the angle between \vec{S}_2 and \vec{L} is conserved, so that β is constant. However, in this case the angles between the small spin \vec{S}_1 and the other two vectors will not be

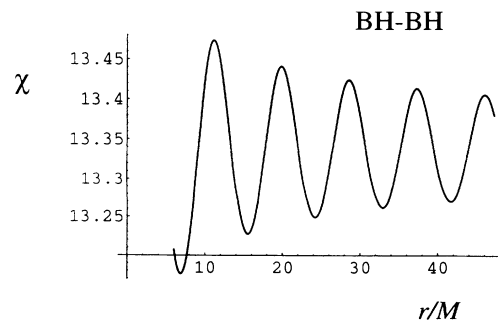


FIG. 20. The evolution of χ for a BH-BH binary; see caption of Fig. 18. Both black holes were assumed to be maximally rotating.

conserved. Thus, the zeroth-order solutions $\alpha_j^{(0)}$ will be nonconstant. We start by deriving these solutions.

Substituting $s_1 = 0$ into Eqs. (B6) – (B8) we find that $\alpha_2^{(0)}$ is constant, i.e., $\alpha_2^{(0)} = \alpha_{2,i} \equiv \alpha_2(r_i)$, where r_i is the initial orbital separation, and that

$$\frac{d\alpha_1^{(0)}}{dr} = -h_1 \alpha_3^{(0)}, \quad (\text{B11})$$

$$\frac{d\alpha_4^{(0)}}{dr} = -h_4 \alpha_3^{(0)}. \quad (\text{B12})$$

Here

$$h_1 = -\frac{15s_2}{128\mu M_2}, \quad (\text{B13})$$

$$h_4 = \frac{15}{128\mu} (s_2 \alpha_{2,i} + L \delta), \quad (\text{B14})$$

and $\delta \equiv (M_1^2 - M_2^2)/(M_1 M_2)$. The coefficient h_4 is non-constant as $L = \mu\sqrt{r}$ depends on r . However, since it will typically vary slowly compared to the oscillations in the angles, we can approximate it to be constant. (The evolution of h_4 gives rise to a slow evolution in the amplitude and frequency of the oscillations of the $\alpha_j^{(0)}$'s.) Defining

$$\alpha_{\pm} \equiv h_4 \alpha_1^{(0)} \pm h_1 \alpha_4^{(0)} \quad (\text{B15})$$

we find that $\alpha_{-}(r)$ is constant, $\alpha_{-}(r) = \alpha_{-,i} \equiv \alpha_{-}(r_i)$, and

$$\frac{d\alpha_{+}}{dr} = -2h_1 h_4 \alpha_3^{(0)}. \quad (\text{B16})$$

This equation can be solved by combining it with the constraint (B5). To zeroth order in s_1 , the constraint can be expressed using Eq. (B15) in the form

$$\alpha_3^{(0)}(r)^2 + \nu^2 [\alpha_{+}(r) - \hat{\alpha}_{+}]^2 = \kappa^2, \quad (\text{B17})$$

where

$$\nu = \frac{\nu_0}{2h_1 h_4}, \quad (\text{B18})$$

$$\nu_0^2 = h_1^2 + h_4^2 - 2h_1 h_4 \alpha_{2,i}, \quad (\text{B19})$$

$$\kappa^2 = 1 - \alpha_{2,i}^2 - (1 + \alpha_{2,i}^2) \frac{\alpha_{-i}^2}{\nu_0^2}, \quad (\text{B20})$$

$$\hat{\alpha}_{+} = -(h_1^2 - h_4^2) \frac{\alpha_{-i}}{\nu_0^2}. \quad (\text{B21})$$

Combining Eqs. (B16) and (B17) yields the solutions

$$\alpha_3^{(0)}(r) = \alpha_{3,i} \cos \Phi + \nu(\alpha_{+,i} - \hat{\alpha}_{+}) \sin \Phi, \quad (\text{B22})$$

$$\alpha_{+}(r) = \hat{\alpha}_{+} - \frac{\alpha_{3,i}}{\nu} \sin \Phi + (\alpha_{+,i} - \hat{\alpha}_{+}) \cos \Phi, \quad (\text{B23})$$

where $\alpha_{+,i} = \alpha_{+}(r_i)$, $\alpha_{3,i} = \alpha_3(r_i)$, and

$$\Phi = \nu_0(r - r_i). \quad (\text{B24})$$

Note that ν_0 is the frequency of oscillation of the $\alpha_j^{(0)}$'s — frequency with respect to changing orbital radius r , not changing time t .

Analytic expressions for the functions $\alpha_1^{(0)}, \dots, \alpha_4^{(0)}$

can now be obtained by combining Eqs. (B13) – (B15) and (B18) – (B23). These expressions depend in a complex way on all of the initial spin direction parameters $\alpha_{1,i}$, $\alpha_{2,i}$, and $\alpha_{4,i}$, and also on s_2 , on the mass ratio M_1/M_2 , and on the initial orbital separation r_i/M . For the equal mass case $M_1 = M_2$, the “frequency” ν_0 is given by

$$\nu_0^2 = \frac{s_2^2}{M_2^2} \left[\frac{255}{4096} + \frac{1125}{16384} \alpha_{2,i}^2 \right]. \quad (\text{B25})$$

Values of ν_0 for $M_1 \neq M_2$ are typically much larger than this.

The first-order corrections $\alpha_j^{(1)}(r)$ can be obtained using the zeroth-order solutions and Eqs. (B6) – (B8). However, we are only interested in determining the leading-order behavior of β , and for this purpose we need only evaluate $\alpha_2^{(1)}$. From Eqs. (B7) and (B22) this is given by

$$\begin{aligned} \alpha_2^{(1)}(r) = & \frac{15}{128\mu\nu_0} \left[\frac{1}{M_1} - \frac{s_2 \alpha_{2,i}}{L} \right] \\ & \times [\alpha_{3,i} \sin \Phi - \nu(\alpha_{+,i} - \hat{\alpha}_{+})(\cos \Phi - 1)]. \end{aligned} \quad (\text{B26})$$

Substituting Eqs. (B26) and (B18) – (B23) into (B9) gives a result of the form

$$\beta(r) = A + B \cos \Phi + C \sin \Phi, \quad (\text{B27})$$

where the constants B and C are first order in s_1 . The resulting expression for the total amplitude of oscillation $\mathcal{A} = \sqrt{B^2 + C^2}$ in terms of the variables $\alpha_{1,i}, \dots, \alpha_{4,i}$, M_1/M_2 and r is complicated and not very illuminating, so we do not reproduce it here. Instead we show in Figs. 21 and 22 the quantity $\mathcal{A}_{\max} = \mathcal{A}_{\max}[\alpha_{2,i}, \alpha_{4,i}]$

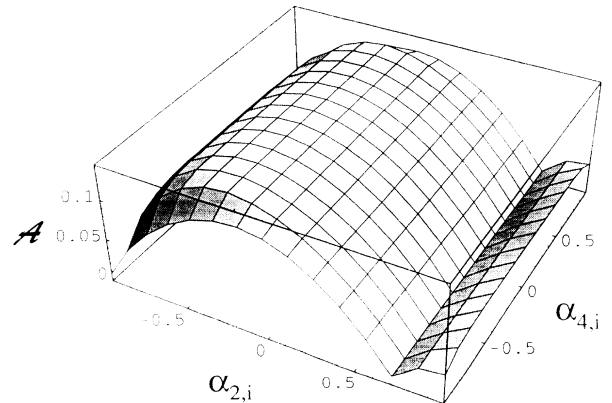


FIG. 21. When one of the spins is small, the evolution of the parameter $\chi = 4\pi - \beta$ is approximately given by

$$\chi = \chi_0 + \mathcal{A} \cos [\nu_0 r + \text{const}],$$

where the “frequency” ν_0 and amplitude \mathcal{A} are slowly varying functions of r . Here we show the amplitude \mathcal{A} for an equal-mass binary, at an orbital separation of $r = 6M$, as a function of $\alpha_{2,i} \equiv \hat{S}_2 \cdot \hat{L}$ and $\alpha_{4,i} \equiv \hat{S}_1 \cdot \hat{S}_2$, where the maximum is taken over the remaining angles. \hat{S}_1 , \hat{S}_2 , and \hat{L} are unit vectors in the directions of the initial spins and the initial orbital angular momentum.

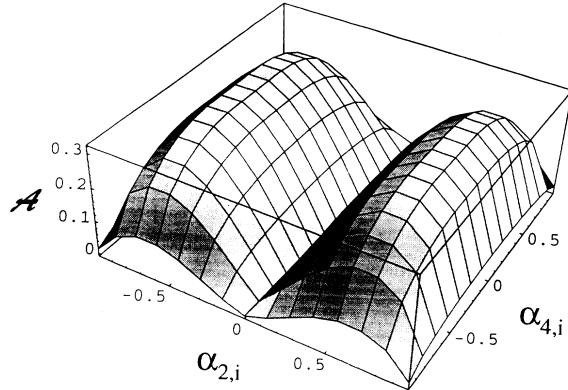


FIG. 22. As in Fig. 21, but for a NS-BH binary with $M_1/M_2 = 1.4/10$.

obtained in the following way: (i) Use Eq. (B5) to eliminate $\alpha_{3,i}$ in terms of $\alpha_{1,i}$, $\alpha_{2,i}$, and $\alpha_{4,i}$; (ii) numerically maximize over values of $\alpha_{1,i}$ that lie in the range between the values $\alpha_{2,i} \alpha_{4,i} \pm \sqrt{(1 - \alpha_{2,i}^2)(1 - \alpha_{4,i}^2)}$ allowed by Eq. (B5); (iii) choose the maximal spin magnitudes $s_1 = M_1^2$, $s_2 = M_2^2$; (iv) choose the final orbital separation $r = 6M$, the value for which the amplitude A will most likely be largest. It can be seen from these plots that for all choices of initial angles, $A \leq 0.25$.

In the special case that $M_1 = M_2$, the formulas simplify and we find that $A \propto 1/\sqrt{r}$ (this is not true in general). Specifically we find in this case that

$$\begin{aligned} B = \frac{376}{384\sqrt{r}} & \left[\alpha_{1,i} \alpha_{2,i} - 2\alpha_{4,i} \right. \\ & \left. + \frac{15}{128} (4 - \alpha_{2,i}^2) (\alpha_{1,i} \alpha_{2,i} + 2\alpha_{4,i}) \nu_0^{-2} \right] \end{aligned} \quad (B28)$$

and

$$C = -\frac{235}{512} \frac{\alpha_{2,i} \alpha_{3,i}}{\sqrt{r} \nu_0}, \quad (B29)$$

where ν_0 is given by Eq. (B25).

To summarize, we have determined the evolution of the quantity $\chi = 4\pi - \beta$ both numerically, for a wide range of

initial conditions, and analytically, in the regime where $|\vec{S}_1| \ll M^2$. In all cases we find that the amplitude of the oscillations of χ is ≤ 0.25 .

APPENDIX C: THE DECOUPLING OF PHASE AND AMPLITUDE PARAMETERS IN THE FISHER INFORMATION MATRIX

The phase $\Psi(f)$ of the Fourier transform of the waveform can be written in the form

$$\Psi(f) = \sum_{n=1,2,\dots} c_n (f/f_0)^{\alpha_n}, \quad (C1)$$

where $(\alpha_1, \alpha_2, \alpha_3, \dots) = (0, 1, -5/3, -1, -2/3, \dots)$, and the parameters c_1, c_2, c_3, c_4 , etc., are simply related to the parameters $\phi_c, t_c, \mathcal{M}, \mu, \beta$, etc., via Eq. (3.24). The number of variables c_n will depend on the post-Newtonian order to which $\Psi(f)$ is calculated; the following analysis holds for any number of these variables. We can make a linear transformation to new variables

$$d_m = U_m^n c_n \quad (C2)$$

in such a way that

$$\frac{\partial \mathbf{h}}{\partial d_1} = \frac{\partial \mathbf{h}}{\partial c_1} = i\mathbf{h}, \quad (C3)$$

and that for $m \geq 2$ [49],

$$\begin{aligned} \left(i\mathbf{h} \left| \frac{\partial \mathbf{h}}{\partial d_m} \right. \right) & \propto \sum_n (\mathbf{U}^{-1})^n_m \int_0^\infty df \frac{|\tilde{h}_0|^2}{S_n(f)} (f/f_0)^{\alpha_n} \\ & = 0. \end{aligned} \quad (C4)$$

The key point now is that the inner product

$$\Gamma_{am} = \left(\frac{\partial \mathbf{h}}{\partial \mu^a} \left| \frac{\partial \mathbf{h}}{\partial d_m} \right. \right),$$

where μ^a is any of the “amplitude” parameters D, ψ, v , and d_1 , will also be proportional to the right-hand side of Eq. (C4) for $m \geq 2$, and so will vanish. This can be seen from the structure of Eq. (4.11). Consequently, in the new variables D, v, ψ , and $d_m, m = 1, 2, \dots$, the Fisher matrix (A30) will be block diagonal, which establishes the result stated in Sec. IV C.

-
- [1] R. Narayan, T. Piran, and A. Shemi, *Astrophys. J.* **379**, L17 (1991).
 - [2] E. S. Phinney, *Astrophys. J.* **380**, L17 (1991).
 - [3] A. Abramovici, W. E. Althouse, R. W. P. Drever, Y. Gürsel, S. Kawamura, F. J. Raab, D. Shoemaker, L. Sievers, R. E. Spero, K. S. Thorne, R. E. Vogt, R. Weiss, S. E. Whitcomb, and M. E. Zucker, *Science* **256**, 325 (1992).
 - [4] C. Bradaschia *et al.*, *Nucl. Instrum. Methods* **A289**, 518 (1990); also in *Gravitation 1990*, Proceedings of the Banff Summer Institute, Banff, Alberta, edited by R. Mann and P. Wesson (World Scientific, Singapore, 1991).
 - [5] A. V. Tutukov and L. R. Yungelson, *Mon. Not. R. Astron. Soc.* **260**, 675 (1993).
 - [6] B. F. Schutz, *Nature (London)* **323**, 310 (1986); *Class. Quantum Grav.* **6**, 1761 (1989).
 - [7] Y. Gürsel and M. Tinto, *Phys. Rev. D* **40**, 3884 (1990).
 - [8] C. Cutler, T. A. Apostolatos, L. Bildsten, L. S. Finn, É. E. Flanagan, D. Kennefick, D. M. Marković, A. Ori, E. Poisson, G. J. Sussman, and K. S. Thorne, *Phys. Rev. Lett.* **70**, 2984 (1993).
 - [9] D. Marković, *Phys. Rev. D* **48**, 4738 (1993).
 - [10] B. F. Schutz, in *Gravitational Collapse and Relativity*, Proceedings of the 14th Yamada Conference, Kyoto, Japan, 1986, edited by H. Sato and T. Nakamura (World Scientific, Singapore, 1986), pp. 350–368.
 - [11] D. F. Chernoff and L. S. Finn, *Astrophys. J.* **411**, 5 (1993).
 - [12] K.S. Thorne, in *300 Years of Gravitation*, edited by S.

- W. Hawking and W. Israel (Cambridge University Press, Cambridge, England, 1987), pp. 330–458.
- [13] C. Cutler, L. S. Finn, E. Poisson, and G. J. Sussman, Phys. Rev. D **47**, 1151 (1993).
- [14] L. S. Finn and D. F. Chernoff, Phys. Rev. D **47**, 2198 (1993).
- [15] P. Jaranowski and Andrzej Krolak, Phys. Rev. D **49**, 1723 (1994).
- [16] P. C. Peters, Phys. Rev. **136**, B1224 (1964).
- [17] However eccentricities may not be negligible for binaries formed in dense star clusters in galactic nuclei; see G.D. Quinlan and S.L. Shapiro, Astrophys. J. **321**, 199 (1987).
- [18] L. Bildsten and C. Cutler, Astrophys. J. **400**, 175 (1992).
- [19] C. Kochanek, Astrophys. J. **398**, 234 (1992).
- [20] A rapidly rotating neutron star will be somewhat oblate, and, therefore, compared to a point mass, its potential energy will be modified by a term proportional to its quadrupole moment times the second derivative of the gravitational potential at its center of mass [18]. However this correction to the orbital energy is of second post-Newtonian order, and thus is of higher order than the other post-Newtonian effects considered in this paper.
- [21] L. A. Wainstein and V. D. Zubakov, *Extraction of Signals from Noise* (Dover, New York, 1962).
- [22] E. Flanagan and K. S. Thorne (unpublished).
- [23] K. S. Thorne (private communication).
- [24] The noise spectrum to which Eq. (2.2) is an approximate analytic fit is given by the sum of the following terms from Ref. [14]: Eq. (4.1), with parameters $\eta I_0 = 60 \text{ W}$, $L = 4 \text{ km}$, $f_c = 130 \text{ Hz}$, $\lambda = 5.1 \times 10^{-7} \text{ m}$, and $A^2 = 5 \times 10^{-5}$; Eq. (4.3) with the modifications to Eq. (4.2) of $f_0 \rightarrow f^2/f_0$ in the numerator and $ff_0/Q_0 \rightarrow f_0^2/Q_0$ in the denominator, and with parameters $Q_0 = 10^9$, $T = 300 \text{ K}$, $f_0 = 1 \text{ Hz}$; and Eq. (4.4), similarly modified, with parameters $f_{\text{int}} = 14 \text{ kHz}$ and $Q_{\text{int}} = 10^6$. Equations (4.2) and (4.4) are modified in order to describe structural damping [25] which is now thought to be the likely dominant damping mechanism in the thermal modes [23].
- [25] P. R. Saulson, Phys. Rev. D **42**, 2437 (1990).
- [26] L. S. Finn, Phys. Rev. D **46**, 5236 (1992).
- [27] S. V. Dhurandhar, A. Krolak, B. F. Schutz, and W. J. Watkins (unpublished).
- [28] Note that this definition differs by a factor of 2 from that found in Ref. [26]. Our definition is chosen to correspond to the quadratic form “ $x_i(\Sigma^{-1})_{ij}x_j$ ” which appears in finite-dimensional Gaussian PDFs, cf. Eq. (A6) above.
- [29] L. S. Finn, A. Ori, and K. S. Thorne (unpublished).
- [30] The last stable circular orbit is not exactly at $r = 6M$ because of the fact that r is the orbital separation in de Donder gauge and not the Schwarzschild radius, and also because of the finite mass ratio. However, this orbit will be close to $r = 6M$; see L. E. Kidder, C. M. Will, and A. G. Wiseman, Class. Quantum Grav. **9**, L125 (1992).
- [31] The calculation is simplified if one first defines the moments
- $$\bar{f}^k \equiv \frac{(f^k h | h)}{(h | h)},$$
- where the inner product $(|)$ is given by Eq. (2.3). As pointed out by Finn and Chernoff [14], all the elements of Γ_{ij} can be expressed in terms of the orbital parameters and a few of the moments \bar{f}^k . This continues to hold true when post-Newtonian corrections are added to the signal. A useful identity is $(f^j h | i f^k h) = 0$ for all real j and k , which follows from Eq. (2.3).
- [32] R. V. Wagoner and C. M. Will, Astrophys. J. **210**, 764 (1976); **215**, 984 (1977).
- [33] A. G. Wiseman, Phys. Rev. D **46**, 1517 (1992).
- [34] E. Poisson, Phys. Rev. D **47**, 1497 (1993).
- [35] A. Krolak, in *Gravitational Wave Data Analysis*, edited by B. F. Schutz (Kluwer Academic, Boston, 1989), p. 59.
- [36] R. Epstein and R. V. Wagoner, Astrophys. J. **197**, 717 (1975); **215**, 984 (1977).
- [37] In fact, because of the spin-induced precession of the orbital plane described in Sec. III B, in general k will be a slowly varying function of time instead of a constant. We neglect this small effect.
- [38] L. Blanchet and T. Damour, Phys. Rev. D **46**, 4304 (1992).
- [39] Somewhat inconsistently, we neglect the δ -function contribution to the derivatives $\partial \bar{h}(f)/\partial \mathcal{M}$ and $\partial \bar{h}(f)/\partial \mu$ that comes from varying the cutoff frequency. While a sharp cutoff gives an acceptable approximation to $h(f)$ (and is easy to work with analytically), it gives a terrible approximation for the derivatives of $h(f)$. Our somewhat careless attitude toward the high-frequency end of the waveform is justified by the fact that the detector noise $S_n(f)$ rises steeply at high frequency, so very little signal to noise is accumulated there.
- [40] The pattern of how the predicted rms errors change, when one includes extra variables in the calculation of the Fisher matrix (2.7) which are strongly correlated with the original variables, can be simply understood by considering the approximation in which all but two of the variables are fixed. The predicted measurement accuracy for a variable x , when its correlations with other variables are neglected, is $\delta x = (h_{,x}|h_{,x})^{-1/2}$. When we include the effects of correlations with another variable y , described by the correlation coefficient
- $$c_{xy} = \frac{\Sigma^{xy}}{\sqrt{\Sigma^{xx}\Sigma^{yy}}} = -\frac{(h_{,x}|h_{,y})}{\sqrt{(h_{,x}|h_{,x})(h_{,y}|h_{,y})}},$$
- then from Eqs. (2.7) and (2.8) we find that (i) the rms error in x is now $\Delta x = \delta x / \sqrt{1 - c_{xy}^2}$, and thus is increased by a large factor if $|c_{xy}|$ is close to one and (ii) if $1 - c_{xy}^2 \ll 1$, the eigenvalues of the variance-covariance matrix (A34) are approximately $(\delta x^{-2} + \delta y^{-2})^{-1}$ and $(\delta x^2 + \delta y^2)/(1 - c_{xy}^2)$, where $\delta y = (h_{,y}|h_{,y})^{-1/2}$. Thus, if δx and δy are comparable, one linear combination of x and y will be measurable with an accuracy comparable to δx , i.e., that accuracy predicted when correlations are neglected; and the orthogonal linear combination will have an rms error that is larger than this by a factor $\sim 1/\sqrt{1 - c_{xy}^2}$.
- [41] L. E. Kidder, C. M. Will, and A. G. Wiseman, Phys. Rev. D **47**, R4183 (1993).
- [42] B. M. Barker and R. F. O’Connell, Gen. Relativ. Gravit. **11**, 149 (1979).
- [43] T. A. Apostolatos, C. Cutler, G. J. Sussman, and K. S. Thorne (unpublished).
- [44] A. Krolak, J. A. Lobo, and B. J. Meers, Phys. Rev. D **43**, 2470 (1991).
- [45] R. L. Forward, Phys. Rev. D **17**, 379 (1978).
- [46] In this section we interpret the parameter t_c to be the time at which the coalescence would be observed by a

hypothetical detector at the origin of spatial coordinates \mathbf{x} .

- [47] Other detector network parameters, such as the distances between the detectors, affect strongly the angular resolution $\Delta\mathbf{n}$ of measurements of sky location, but affect only weakly the distance measurement accuracies. This is due to the decoupling discussed in Sec. IV C and Appendix C.
- [48] We have here ignored the fact that a factor of $\mathcal{M}^{5/6}$ appears in the signal amplitudes; this is unimportant because \mathcal{M} will be measured to much higher relative accuracy ($\sim 10^{-3}$) than the amplitudes ($\sim 10^{-1}$). In other words we in fact calculate $\Delta D_1/D_1$, where $D_1 \equiv D\mathcal{M}^{-5/6}$; for all practical purposes this is the same as $\Delta D/D$.
- [49] In fact we have compared the values of ΔD given by the approximation used in Ref. [9] to those given by Eq. (4.41), and found that they never differ by more than 10% for any values of σ_D , ε_D , v , and ψ .
- [50] Another way to think about this is to associate a signal-to-noise ratio with each polarization component [with respect to fiducial axes determined by the detector network, cf. Eq. (4.25) above] of the incident waves; the distance measurement accuracy will essentially be determined by the smaller of the two signal-to-noise ratios.
- [51] It is simplest to calculate this prefactor using the variables α and β defined by Eq. (4.36) instead of D and v . In fact it diverges at $v = 1$, because of the fact that $\partial\mathbf{h}/\partial\psi \propto \partial\mathbf{h}/\partial\phi_c$ in this limit. This divergence would seem to contradict our claim that the prefactor does not depend strongly on v and D . In the special case where $\varepsilon_D = 0$, a more careful calculation of the integral over ψ and ϕ_c (without first expanding to quadratic order in $\psi - \psi_0$ and $\phi_c - \phi_{c0}$) shows that the effective prefactor remains finite at $v = 1$; we expect similar behavior for $\varepsilon_D \neq 0$. In the case $\varepsilon_D = 0$ we obtain

$$p(v, D) \propto p^{(0)}(v, D) F(\omega\hat{\omega}) F(\zeta\hat{\zeta}) e^{-(\Delta\omega^2 + \Delta\zeta^2)/2},$$

where $\omega = (\alpha + \beta)/\sqrt{2\sigma_D r_0}$, $\zeta = -(\alpha - \beta)/\sqrt{2\sigma_D r_0}$, and $\hat{\omega}$, $\Delta\omega$, etc., are similarly defined in terms of $\hat{\alpha}$, $\hat{\beta}$

[cf. Eqs. (4.54) and (4.55) above] and $\Delta\alpha \equiv \alpha - \hat{\alpha}$, $\Delta\beta \equiv \beta - \hat{\beta}$. The prefactor function F is

$$F(x) \equiv \frac{1}{2\pi} \int_0^{2\pi} e^{-x(1-\cos\theta)} d\theta \approx \begin{cases} \frac{1}{\sqrt{2\pi x}}, & x \gg 1, \\ 1-x, & x \ll 1. \end{cases}$$

Thus the prefactor is regular and slowly varying despite the apparent divergence $\propto 1/\sqrt{\zeta} \propto 1/(1-v)$ that would be obtained by doing a Gaussian integration over the angles ψ and ϕ_c .

- [52] T. Loredo, in *Statistical Challenges in Modern Astronomy*, edited by E. D. Feigelson and G. J. Babu (Springer-Verlag, New York, 1992).
- [53] M. H. A. Davis, in *Gravitational Wave Data Analysis* [35].
- [54] B. S. Sathyaprakash and S. V. Dhurandhar, Phys. Rev. D **44**, 3819 (1991).
- [55] C. W. Helstrom, *Statistical Theory of Signal Detection*, 2nd ed. (Pergamon, New York, 1968).
- [56] B. F. Schutz, *The Detection of Gravitational Radiation* (Cambridge University Press, Cambridge, England, 1989).
- [57] F. Echeverria, Phys. Rev. D **40**, 3914 (1989).
- [58] F. Echeverria, Ph.D. thesis, California Institute of Technology, 1993, addendum to Chap. 2.
- [59] In fact this method can determine all the parameters $\theta = (\theta^1, \dots, \theta^k)$, except for the overall amplitude of the signal which drops out of Eq. (A24). To obtain the overall amplitude one must use Eq. (A28); see Ref. [58] for more details.
- [60] Throughout this paper we use the term *Fisher matrix* to refer to the matrix (A30); strictly speaking, this term as defined in, e.g., Ref. [55] refers to a quantity which coincides with the matrix (A30) only when the noise is Gaussian. The Cramer-Rao inequality is usually stated in terms of this more general Fisher matrix.
- [61] For an example of such a Monte Carlo simulation, see K. Kokkotas, A. Krolak, and G. Tsegas (unpublished).

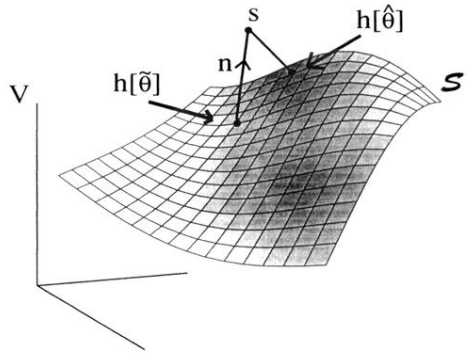


FIG. 1. Gravitational waveforms from coalescing compact binaries are completely specified by a finite number of parameters $\theta = (\theta^1, \dots, \theta^k)$, and so form a surface S in the vector space V of all possible measured detector outputs $s = s(t)$. The statistical properties of the detector noise endow V with the structure of an infinite-dimensional Euclidean space. This figure illustrates the relationships between the true gravitational wave signal $h(\tilde{\theta})$, the measured signal s , and the “best-fit” signal $h(\hat{\theta})$. Given a measured detector output $s = h(\tilde{\theta}) + n$, where $n = n(t)$ is the detector noise, the most likely values $\hat{\theta}$ of the binaries parameters are just those that correspond to the point $h(\hat{\theta})$ on the surface S which is closest [in the Euclidean distance $(s - h | s - h)$] to y .

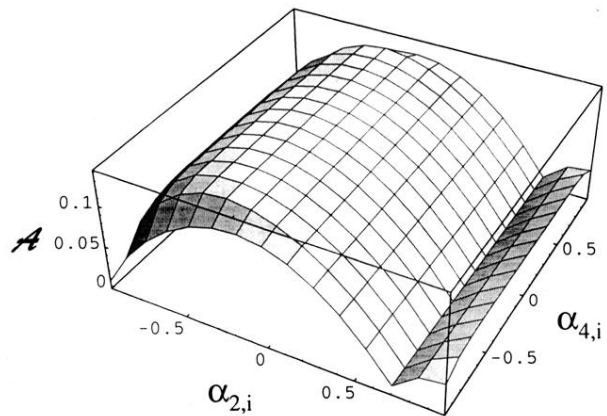


FIG. 21. When one of the spins is small, the evolution of the parameter $\chi = 4\pi - \beta$ is approximately given by

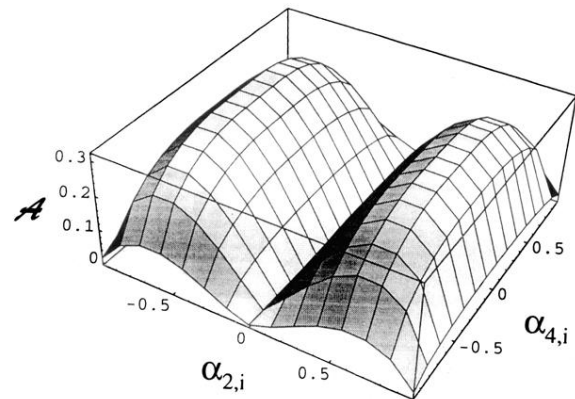


FIG. 22. As in Fig. 21, but for a NS-BH binary with $M_1/M_2 = 1.4/10$.

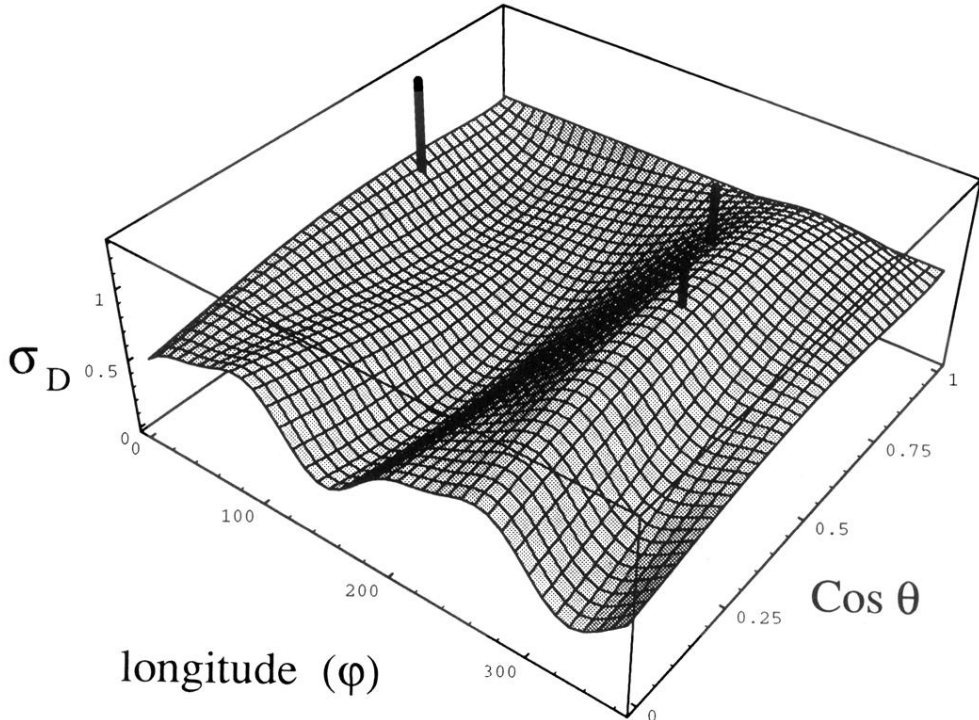


FIG. 5. The amplitude sensitivity function $\sigma_D(\mathbf{n})$, as a function of position on the sky parametrized by the Earth-fixed coordinates θ and φ , for the detector network consisting of the two LIGO detectors in Hanford, Washington and Livingston, Louisiana, and the VIRGO detector in Pisa, Italy. The axis $\theta = 0$ is the Earth's axis of rotation, and $\varphi = 0^\circ$ longitude. Only sky positions over the northern hemisphere are shown, because σ_D takes the same values at antipodal points. The function $\sigma_D(\mathbf{n})$ has the following meaning: for a source of waves in the direction \mathbf{n} , the combined signal-to-noise ratio of the whole network, averaged over all polarization angles ψ of the source (equivalently, averaged over rotations of the source in the plane perpendicular to the line of sight), will be proportional to $\sigma_D(\mathbf{n})$. The thick black lines indicate the positions of the three detectors. This plot can be generated by combining Eqs. (4.31) and (4.35) of the text with the network parameters given after Eq. (4.35).

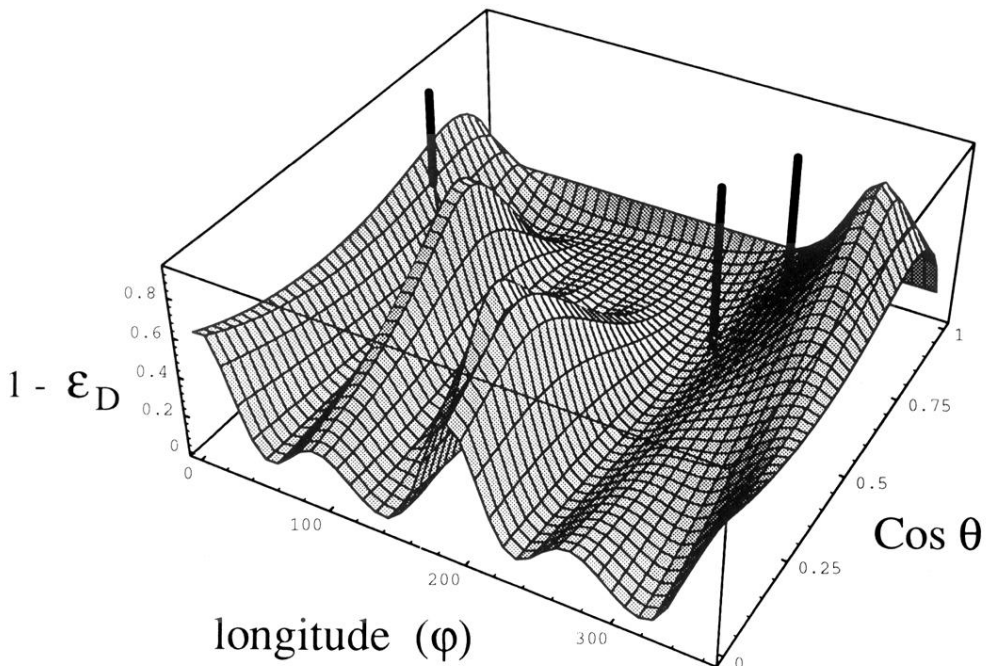


FIG. 6. The polarization sensitivity function $1 - \epsilon_D(\mathbf{n})$, for the LIGO-VIRGO detector network; see caption of Fig. 5. This plot can be generated by combining Eqs. (4.30), (4.32), (4.34), and (4.35) of the text. The quantity $\epsilon_D(\mathbf{n})$ essentially measures the “skewness” or asymmetry in the sensitivities of the network to the two independent polarization components of waves propagating in the direction \mathbf{n} . When $\epsilon_D \approx 0$, the network has roughly equal sensitivity to both polarization components. When $\epsilon_D \approx 1$, on the other hand, one polarization component can be measured far more accurately than its orthogonal counterpart. In this case the signal-to-noise ratio for incident, strongly linearly polarized bursts of waves (e.g., those from edge-on coalescing binaries) will depend sensitively on the polarization axis, i.e., it would vary by large factors if the source were rotated in the plane perpendicular to the line of sight. Note that the polarization sensitivity is poor ($\lesssim 0.2$) for directions directly overhead the two LIGO detectors (because the two detectors are nearly parallel), and is typically $\lesssim 0.3$ over most of the sky. Good sensitivity is achieved in isolated regions.

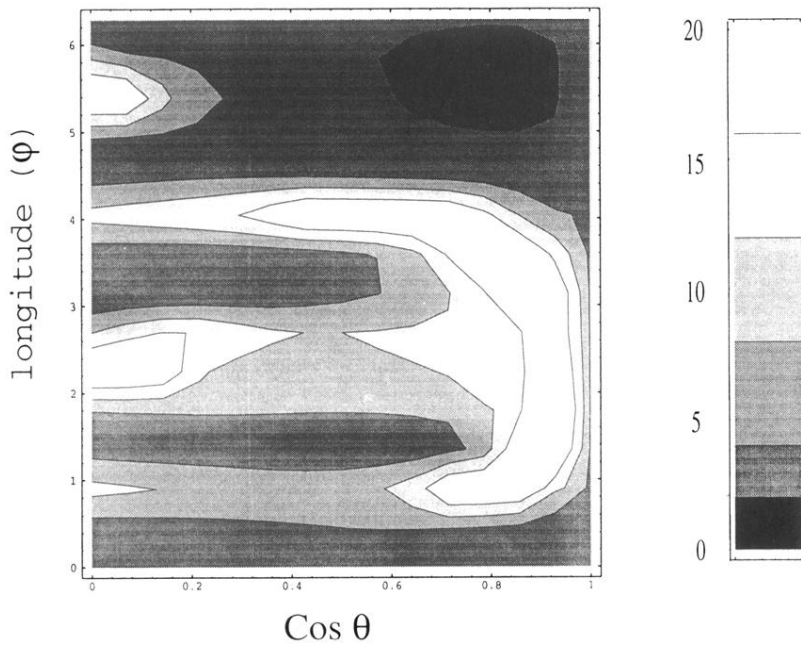


FIG. 7. The dependence of the distance measurement accuracy $\Delta D/D$ on the sky location \mathbf{n} , the polarization angle ψ , and the cosine v of the angle of inclination of the orbit to the line of sight is approximately given by $\Delta D/D \propto \Upsilon(\mathbf{n}, v, \psi)$, where the dimensionless function Υ is defined in Eq. (4.42). Here we plot for the LIGO-VIRGO detector network the quantity Υ_{\max} obtained by maximizing Υ over all polarization angles ψ , at $v^2 = 1/2$, as a function of θ and φ . Higher values of Υ indicated by regions of lighter shading correspond to poorer measurement accuracy.

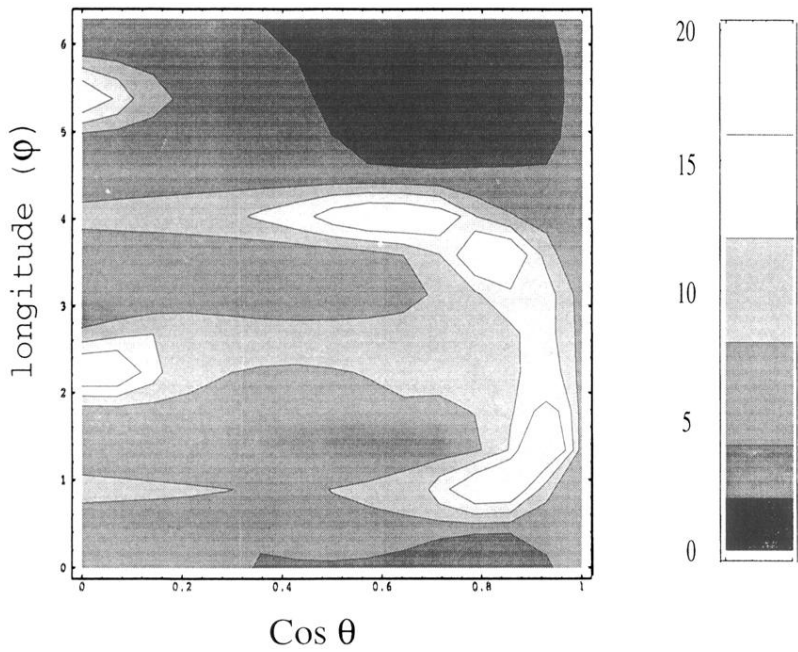


FIG. 8. The quantity Υ_{\min} which is obtained by minimizing $\Upsilon(\mathbf{n}, v, \psi)$ over ψ , at $v^2 = 1/2$; see caption of Fig. 7.